Capacity Assessment of Titanium Pipes Subjected to Bending and External Pressure

by

Arve Bjørset

Department of Structural Engineering
Faculty of Civil and Environmental Engineering
The Norwegian University of Science and Technology
N-7491 Trondheim, Norway.

Dedicated to
Mariann
for her patience and understanding
and to
Mats and ***Simon***
for their invaluable contribution to my work
though they were not aware of it.
Obviously, there have been moments of play,
when I have been physically present,
but mentally absent.
Irrespective of this,
as they both frequently say:
Hakuna Matata ...

"And all those days that came and went,
I did not know that this way life."
Stig Johansson

ABSTRACT

Exploration for oil and gas is moving towards deeper waters. Steel has been the most common riser material. Related to deep water concepts titanium has become an alternative to steel for these applications.

Several codes exist today for predicting collapse loads for marine pipes. However, the capacity formulas are developed for steel. If the formulas are applied directly to titanium several parameter uncertainties will be unknown. Ideally, extensive model testing of titanium pipes is required. This thesis discusses and investigates utilisation of experimental material test data and a supplementary numerical approach based on finite element analysis. The relationship between material model parameters as input to the analysis and the collapse capacity is investigated by performing a series of nonlinear FEM analyses.

Statistical models for the input material model parameters are established based on tests on small specimens cut from titanium pipes. These models are subsequently combined with results from the FEM analyses by application of response surface methods. As output from the analysis, the probability distributions of the pipe capacity with respect to local buckling/collapse are obtained.

Finally, the data from the nonlinear finite element analyses are compared to a relevant design code. Suggestions for a possible basis for design formulas to check for the local collapse capacity of deep water titanium risers are provided.

AKNOWLEDGEMENTS

This study has been carried out under the supervision of Professor Svein Remseth, at the Division of Structural Engineering, the Norwegian University of Science and Technology. His advice, guidance, motivation and fruitful discussions throughout the whole study are hereby gratefully acknowledged.

Professor Bernt J. Leira and Professor Carl M. Larsen, at the Division of Marine Structures, NTNU, have been co-supervisors. Professor Bernt J. Leira is acknowledged for his interest and cooperation throughout the whole study, for suggestions and for valuable comments and discussions to Chapters 3, 5 and 6, in particular. I appreciate the contribution from Professor Carl M. Larsen for his discussions to Chapters 4 and 6.

Norsk Hydro provided the titanium pipe sections from which the material test specimens were prepared. This important support of the present study is gratefully acknowledged.

The material tests were conducted as part of the research program 'Material modelling for structural analysis' supported by the Research Council of Norway, NFR.

I would also like to extend thanks to some of the colleagues at the Division of Structural Engineering, in particular, Dr. ing. Arne Aalberg and doctoral student Ivar Tiller for valuable help with ABAQUS- and FEM-related problems. Credits are also to be given to Mr. Eirik Fyhn, at the Faculty of Civil and Environmental Engineering, NTNU, who prepared several of the figures.

I am also thankful to Professor Ragnar Sigbjörnsson, Dr. ing. Magne K. Nygård, and Professor Jørgen Amdahl for their participation as members of the thesis committee.

This study was made possible by a 4 year scholarship from the Norwegian University of Science and Technology, Faculty of Civil and Environmental Engineering. The flexible attitude to MARINTEK Division of Structural Engineering, represented by Division Manager Oddvar Inge Eide, especially in the last part of the study, is also very much appreciated.

March 2000

Arve Bjørset

TABLE OF CONTENTS

NOTATIONS

Abbreviations:

API	: American Petroleum Institute.
C.o.V.	: coefficient of variation (=standard deviation divided by mean value).
D/t	: Mean diameter over nominal wall thickness-ratio.
DnV	: Det norske Veritas.
FE	: Finite element.
FEM	: Finite element method.
FORM	: First-order reliability method.
IRR	: Implied reserve ratio.
L/D	: Length over diameter-ratio.
NPD	: Norwegian Petroleum Directorate.
TLP	: Tension Leg Platform.
RIFLEX	: Flexible Riser System Analysis Program.
SG	: Specific gravity.
SLS	: Serviceability Limit State
SORM	: Second-order reliability method.
SMYS	: Specified Minimum Yield Strength.
ULS	: Ultimate Limit State.
VIV	: Vortex Induced Vibrations.
X65	: Material Grade of Steel, yield strength=655 ksi=448 MPa.

Roman letters:

A	: Cross-sectional area ($\pi^* (R_{outer}^2-R_{inner}^2)$).
A_i	: Internal cross-sectional area ($\pi^*R_{inner}^2$).
A_e	: External cross-sectional area ($\pi^*R_{outer}^2$).
$\mathbf{C}$	: Damping matrix or Green's deformation tensor.
C	: Predefined level for the maximum bending moment capacity.
C_1, C_2	: Material parameters in Voce material model.
D	: Nominal outside diameter or mean diameter.
D_e	: External diameter.
D_i	: Internal diameter.
D_iM	: Measured internal diameter.
DM	: Measured external diameter.
D_{min}	: Minimum diameter.

D_{max} : Maximum diameter.
e : Piercer eccentricity.
e_k : Unity vector in direction k, k ∈ [1,3].
E : Green's strain tensor.
E : Young's modulus.
f : Volume force per unit volume.
f : Yield surface.
f_0 : Initial imperfection/ovalization.
$f_{\mathbf{X}}( )$: Probability density function.
F : Deformation gradient.
g : Plastic potential.
g( ) : Failure function in probability analyses.
h(**X**) : Maximum bending moment capacity based on all response surfaces.
i : Counting parameter.
I : Moment of inertia.
j : Counting parameter.
k_i : Constants, k ∈ [1,12].
k_T : Temperature derating factor.
k_P, k_M : Constants when calculating the critical external pressure and critical bending moment.
K : Inner position of the test specimen through the thickness or parameter in Ramberg-Osgood material model.
K : Stiffness matrix.
L : Outer position of the test specimen through the thickness.
M : Mean position of the test specimen through the thickness or parameter in Ramberg-Osgood material model. Denotes also bending moment.
M_c : Characteristic limit bending moment or critical bending moment.
$M_{E,c}$: Characteristic environmental bending moment.
$M_{F,c}$: Characteristic functional bending moment.
M_{max} : Maximum bending moment capacity.
M_{ref} : Reference bending moment.
N_{eff} : Effective axial force.
$N_{E,c}$: Characteristic environmental axial pipe wall force.
$N_{F,c}$: Characteristic functional axial pipe wall force.
n : Outward unit vector of a surface.
n : Parameter in Tvergaard and Needleman material model.
o : Cross-sectional orientation.
O : Orientation of the test specimen.
p : Applied external pressure.
p_c : Critical external pressure.
p_e : External pressure.

p_{el} : Elastic Euler buckling pressure.
p_f : Probability of failure.
p_i : Internal pressure.
r : Residual force or radius to a specific point in the pipe wall.
R : Anisotropy response parameter or applied load in probability analyses.
R_1, R_2 : Material parameters in Voce material model.
S : Different locations for the test specimens in the longitudinal direction or limit load in probability analyses.
S_f : Safety factor.
t : Nominal wall thickness or time parameter.
t : Surface force per unit surface.
T_E : Effective tension.
T_{TW} : True wall tension.
t_0 : Initial thickness of the test specimen in the gauge area.
t_f : Thickness of the test specimen in the gauge area after rupture.
t_m : Measured wall thickness.
u_i : Displacement in direction i, where $i \in [1,6]$.
U_i : Normalized variable in probability analyses, where $i \in [1,n]$.
V_0, V_t : Prescribed and arbitrary material volume.
w_o : Initial width of the test specimen in the gauge area.
w_f : Width of the test specimen in the gauge area after rupture.
X_i : General variable in probability analyses, where $i \in [1,n]$.
X : General vector of the parameters X_i.

Greek letters:

α_{gw} : Girth weld reduction factor.
α : Crystalline phase of titanium or proportionality factor. Also used as normalized stress and scaling parameter.
β : Reliability index or one particular crystalline phase of titanium. Also used as normalised stress.
γ : Utilisation ratio.
γ_C : Condition load factor.
γ_E : Environmental load factor.
γ_F : Functional load factor.
γ_R : Strength resistance load factor.
γ_ε : Strain capacity resistance factor.
δ_0 : Initial imperfection according to DnV (1996).

δ_{kl} : Kronecker-delta.
ε : Applied strain.
ε_c : Critical strain.
ε_f : Fracture strain.
$\varepsilon_{E,c}$: Characteristic environmental longitudinal strain.
$\varepsilon_{F,c}$: Characteristic functional longitudinal strain.
$\varepsilon_{M,c}$: Characteristic buckling strain capacity.
ε_p : True plastic strain.
ε_u : Ultimate strain.
κ : Curvature or hardening parameter.
λ : Load level or stretch-ratio of a material.
π : 3.1415927.
ν : Poisson's ratio.
ρ_{eq} : Equivalent metal density.
$\rho_{titanium}$: Equivalent titanium density.
η : Usage factor.
$\boldsymbol{\sigma}$: Cauchy's stress tensor.
σ : Stress.
σ_i : Stress in direction i, where $i \in [1,3]$.
σ_a : True axial wall stress (zero if compressive).
σ_E : Critical stress of completely elastic material.
σ_{EL} : Elastic limit stress.
σ_H : Hoop stress or average strain hardening in the strain range from 0.5% up to 5%.
σ_L : Longitudinal stress.
σ_M : Average strength hardening in the strain range from 0.5% up to 5%.
σ_U : Ultimate stress.
σ_{VM} : Von-Mises stress.
σ_0 : Parameter in the Ramberg-Osgood material model.
$\sigma_{0.01}$: Stress at 0.01% true, plastic strain.
$\sigma_{0.05}$: Stress at 0.05% true, plastic strain.
$\sigma_{0.2}$: Stress at 0.2% true, plastic strain.
σ_Y : Yield strength.
σ_Y^* : Reduced yield strength.
$\boldsymbol{\tau}$: Kirchhoff's stress tensor.
Ω : Domain requiring that the failure function is less than zero.

C h a p t e r 1

INTRODUCTION

"This is not technology,
it is theology."
In broader terms of P. Gordon.

1.1 BACKGROUND

When exploring for oil and gas in deep water, risers constitute the transportation system to bring the hydrocarbons to the surface. The riser configurations are also critical and sometimes non-redundant element in offshore activities. The whole concept fails if the risers fail.

There are several commonly employed riser configurations for the production / export-phase. The risers can be vertical or catenary (free hanging). Other configurations are so-called lazy / steep wave and lazy / steep S. These risers can either be pure metallic or consist of both metallic and thermoplastic layers (flexible risers). A pure metallic export catenary riser in deep water is considered herein, see Figure 1.1.

Steel has been the most common riser material. Steel catenary risers have been used for example in the Gulf of Mexico, Sertã et al. (1996) and as a flexible catenary riser at the Snorre field, Mollan (1992). However, titanium may offer several benefits compared with steel. This is due to a unique and attractive combination of physical, mechanical and corrosion properties relevant for most of the riser configurations. Potential concepts that has almost been impossible to develop due to limitations when employing steel as riser material, may become possible due to potential use of titanium.

Titanium has approximately twice the specified minimum yield strength compared to steel. The modulus of elasticity and the metal density are typically half of that for steel, Berge et al. (1995). These combinations lead to higher flexibility, improved capacity and lower top tensions, which may imply simpler and cheaper topside equipment such as tensioner device. Titanium has been used in offshore applications, e.g. Heidrun Tension Leg Platform's drilling riser, Thornton (1994) and Sauer et al. (1996), and as a stress joint in the Gulf of Mexico.

1.2 OBJECTIVES AND SCOPE OF WORK

The objective for the present study is to investigate the maximum bending moment capacity for a catenary titanium riser. The catenary riser is connected to a Tension Leg Platform (TLP) in deep water, as shown in Figure 1.1. The riser is chosen to be exporting oil. The internal diameter and internal pressure are set equal to 20 in and 30 bar, respectively. This is representative for an oil export riser, Karunakaran et al. (1996).

This particular type of riser is subjected to largest external load effects either at the top or in the sag-bend region (see the 'X' in Figure 1.1). The top of the riser is subjected to large dynamic motions, due to waves, which cause high bending moments in addition to high tension levels. However, in the sag-bend region, high external pressure acts simultaneously with large bending moments. Implicitly, local buckling / collapse may occur for a catenary riser configuration in the sag-bend region. The maximum bending moment capacity is investigated in this particular area. The capacity to withstand the combination of external pressure and bending moment depends on material properties and cross-sectional geometry, and these are the major capacity parameters investigated in detail in this study. Furthermore, the uncertainty of the major parameters in relation to the uncertainty in the estimated capacity is also investigated extensively.

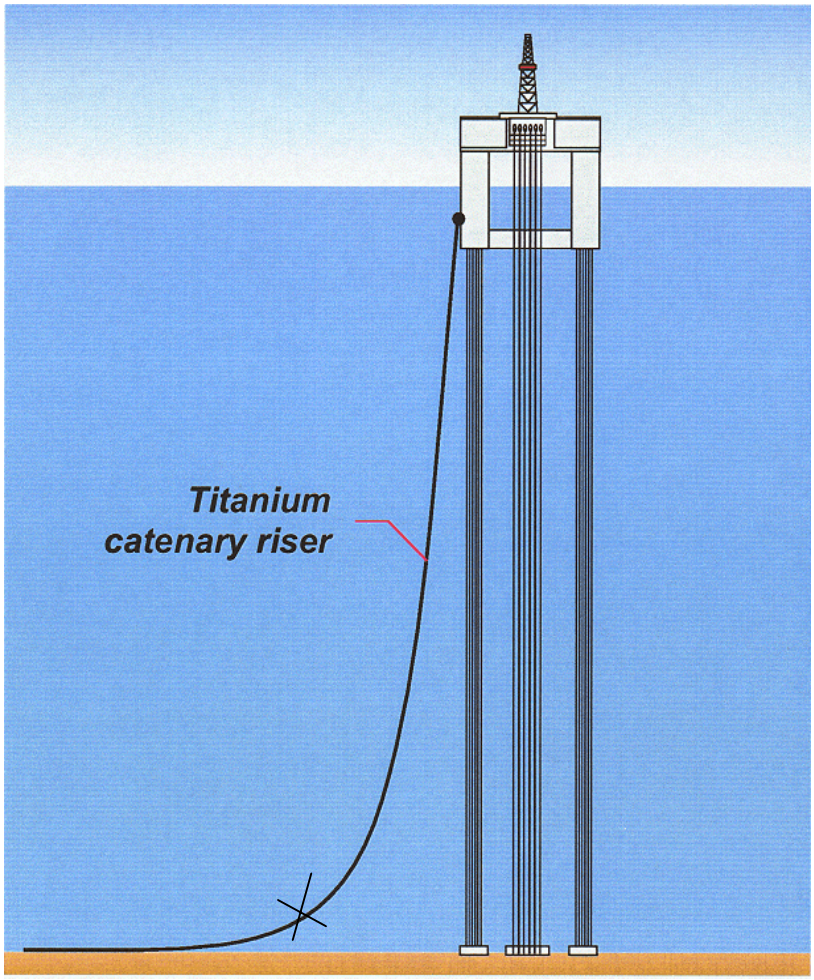

Figure 1.1 Titanium catenary riser connected to a TLP at deep water ('X' is to be interpreted as the sag-bend region). The figure is not drawn to scale in vertical and horizontal direction.

1.3 PREVIOUS WORK RELATED TO LOCAL BUCKLING AND COLLAPSE ANALYSIS OF PIPES

Brazier (1927) dealt analytically with the problem of pure bending of pipes that caused ovalization of the cross-section. He included second order effects and derived moment-curvature relationship based on elastic material behaviour. He also concluded that elastic pipes were characterised by a limit load type of instability when subjected to pure bending. Similar aspects were also discussed in Reissner & Weinitschke (1963). However, by the presence of external pressure, the non-linear behaviour becomes softer, and, hence, the limit moments and bifurcation loads become lower, Fabian

(1977) and Emmerling (1982). Ades (1957) extended Brazier's work by taking inelastic material behaviour into account. He employed theory of plasticity and assumed an elliptical ovalization shape for the cross-section. For relatively thin pipes, local shell buckling (bifurcation buckling) occurs, Timoshenko and Gere (1961). Reissner (1959) analysed elastic tubes under bending and pressure, using an analytical formulation based on approximate solutions in the form of a series expansion. Stephens et al. (1975) performed analytical work based on finite difference technique for thin, elastic pipes. Holand and Remseth (1975) and Remseth et al. (1977) performed pipeline buckling analysis with the use of finite elements taking both material non-linearities and large displacements into account. They developed the computer program (TUBBUC) based on finite elements and capable of performing inelastic buckling analysis of pipelines.

Some experimental research was done in order to obtain adequate knowledge of behaviour of deep-water pipelines. Early laboratory research was mainly performed on tubular members, e.g. Schilling (1976), Sherman (1976), Korol (1979) and Reddy (1979). Murphey & Langner (1985) and Johns & McConnel (1983) presented some results on pipelines. Sherman (1976) and Reddy (1979) also performed experiments for several D/t-ratios. Further experimental data was provided by Kyriakides & Shaw (1982), Yeh & Kyriakides (1986a, 1986b) and Kyriakides & Ju (1992).

Gellin (1980), who investigated ovalization instability using Galerkin formulation with trigonometric functions for in-plane section deformation performed additional analytical solutions. Shaw & Kyriakides (1985) extended Gellin's solution procedure. Furthermore, Bushnell (1981) and Calladine (1983) contributed to solve this problem. Fabian (1977, 1981) dealt with relatively thick pipes and developed a more complete analysis of the problem involving inelastic effects with isotropic hardening. Additionally, a two-dimensional finite element formulation on thick-walled pipelines using large displacements, non-linear shell theory was adopted by Row et. al (1987). However, the results were limited to the case of bending under constant pressure.

For pure theoretical investigation related to this problem, Croll & Ellinas (1984), Makowski & Stumpf (1990), van den Berg (1995) and Willson & Myers (1990) are some relevant references.

Winter et al. (1985) emphasised that the estimated buckling load level was sensitive to the loading history. Important, extensive experimental research as well as analytical results were published by Corona & Kyriakides (1988a, 1988b) and Kyriakides & Shaw (1982). These laboratory tests were mainly stainless-steel tubes with D/t-ratios varying from 18 up to 35. Analytical and experimental results were in good agreement and concluded that collapse prediction under combined pressure and bending is sensitive to the loading path. Fowler (1990) verified from large-scale tests. Karamanos & Tassoulas (1991) performed analyses for different loading paths. Furthermore, Walker (1994) investigated pipelines subjected to high levels of strain, instead of stress, which some of today's codes are based on. Additionally, Torselletti & Curti

(1995), Mørk et al. (1996) and Jiao et al. (1995, 1997) performed research on buckling and collapse of steel pipelines/risers based on probabilistic modelling.

1.4 ORGANISATION OF THE REPORT

The finite element method is used to investigate the maximum bending moment capacity. The analyses combine a global beam model with a local finite element shell model. The theory, material model and solution algorithm as basis for the nonlinear shell analysis, is outlined in Chapter 2. Furthermore, in the same chapter the choice of the computer code ABAQUS is explained, since it offers necessary options for the modelling and the solution of the problem.

Chapter 3 covers the material properties used in the numerical FE-studies. They are based on laboratory testing of test specimens cut from two titanium pipes. The objective of this chapter is to identify the variability in material parameters as the yield strength, Young's modulus, possible anisotropy and strain hardening properties.

The numerical models for the response analyses are established and assessed in Chapter 4. The beam model provides stress resultants to be applied to the local shell model, and the local finite element shell model. The shell model is evaluated with respect to type of elements, element mesh, size of model etc. The response estimates from the model are compared with analytical and experimental results.

Chapter 5 presents an extensive study of the maximum bending moment capacity. The influence on the maximum bending moment capacity from variations in the material parameters and cross-sectional geometry based on laboratory tests is identified. Statistical modelling of the uncertain parameters is done, and probability analyses are performed to identify the type of distribution of the maximum bending moment capacity. Further reliability analyses are performed to identify the most important parameters affecting the maximum bending moment capacity.

Chapter 6 contains a visualisation of mechanical limit states based on steel formula when parameter values for both steel and titanium are used. A comparison of computed capacity and design code limit values for steel and titanium is presented. A basis for possible alternative formulas for the critical external pressure and the critical bending moment for titanium are provided. Furthermore, an alternative shape of the interaction formula between bending and external pressure compared to the ones in commonly employed design codes is suggested for titanium.

C h a p t e r 2

BASIS FOR THE PRESENT NONLINEAR SHELL ANALYSIS IN ABAQUS

"Euclid taught me that without assumptions, there is no proof. Therefore, in any argument, examine the assumptions."
Eric T. Bell (1883-1960)

This chapter gives a brief overview of the computational basis for the nonlinear finite element shell analyses that have been run with the computer code ABAQUS (1996) for the present study. The basis is included as a background for the assessment of computed results. Details in the derivation of the various quantities are incorporated to a very limited extent.

In addition to the theory and user's manuals of ABAQUS, the present outline has been based on Malvern (1969), Crisfield (1991) and NAFEMS (1992).

2.1 DESCRIPTION OF MOTION

A prescribed and arbitrary material volume, V_0, is introduced in a Cartesian coordinate system with ortonormal base vectors $\mathbf{e}_k$ (k=1,2,3), see Figure 2.1.

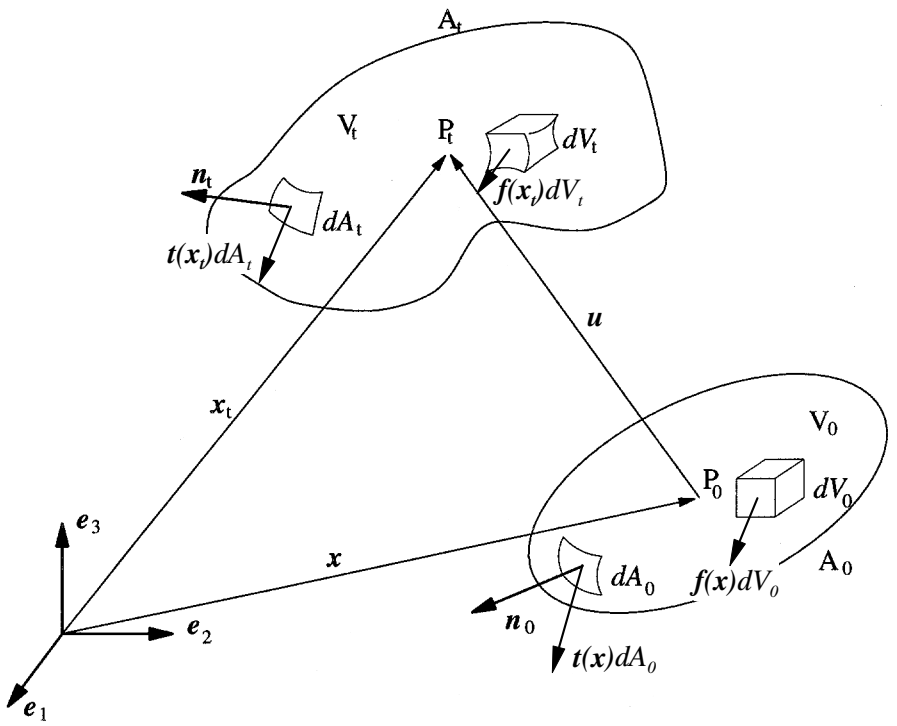

Figure 2.1 The volume V_0 in the reference configuration (t=0) and at time t=t.

A time parameter, t, is measured from a reference point (t=0) representing e.g. the loading parameter in an incremental nonlinear static analysis. $\mathbf{x}$ is the vector from the origin in the Cartesian coordinate system to a material particle in V_0, i.e. $\mathbf{x} = x_k \, \mathbf{e}_k$.

At a time, t, the initial volume, V_0, has deformed into a volume V_t. The new position of a material particle is defined by

$$\mathbf{x}_t = \mathbf{x}_t(\mathbf{x},t) = x_{t,k} \, (\mathbf{x},t) \, \mathbf{e}_k \tag{2.1}$$

where $\mathbf{x}$ are the material coordinates and $\mathbf{x}_t$ are the spatial coordinates.

The motion of a material particle from the reference position, $\mathbf{x}$, to the position at time t, $\mathbf{x}_t$, is defined by

$$\mathbf{u} = \mathbf{x}_t - \mathbf{x} = \mathbf{u}(\mathbf{x},t) \tag{2.2}$$

2.2 DEFORMATIONS AND STRAIN

The deformation gradient is a 2nd order tensor, defined by $\boldsymbol{x}_t$ in the following expression that gives the relation between an infinitesimal vector in the deformed and the reference configuration

$$\mathbf{F} = \text{grad}\, \boldsymbol{x}_t = (\partial x_{t,i} / \partial x_j)\, \mathbf{e}_i \mathbf{e}_j \tag{2.3}$$

implying that

$$d\mathbf{x}_t = \mathbf{F}(\mathbf{x})\, d\mathbf{x} \tag{2.4}$$

$\boldsymbol{e}_i$ and $\boldsymbol{e}_j$ are identified by the following general expression

$$\mathbf{e}_k = \partial \mathbf{x} / \partial x_k \tag{2.5}$$

The deformation gradient, **F**, may also be written as follows (more convenient for computations):

$$\mathbf{F} = \mathbf{I} + \text{grad}\, \mathbf{u} = (\delta_{ij} + \partial u_i / \partial x_j)\, \mathbf{e}_i \mathbf{e}_j. \tag{2.6}$$

where $\mathbf{I} = \delta_{kl}\, \mathbf{e}_k \mathbf{e}_l$.

The structural behaviour depends on the straining of the material. By considering infinitesimal lengths d**x** (at the reference configuration) and $d\mathbf{x}_t$ (at the deformed configuration) of the material, the reference (dL_0) and deformed lengths (dL_t) can be measured as

$$dL_0^2 = d\mathbf{x}^T \cdot d\mathbf{x} \quad and \quad dL_t^2 = d\mathbf{x}_t^T \cdot d\mathbf{x}_t \tag{2.7}$$

The deformation measure, called 'stretch ratio' and its relationship with the deformation gradient is defined by

$$\lambda = \frac{dL_t}{dL_0} = \sqrt{\frac{d\mathbf{x}_t^T \cdot d\mathbf{x}_t}{d\mathbf{x}^T \cdot d\mathbf{x}}} = \sqrt{\frac{d\mathbf{x}^T \cdot \mathbf{F}^T \cdot \mathbf{F} \cdot d\mathbf{x}}{d\mathbf{x}^T \cdot d\mathbf{x}}} \tag{2.8}$$

A more convenient deformation measure for the present computational purpose is provided by the Green strain tensor (**E**) defined by

$$dL_t^2 - dL_0^2 = d\mathbf{x}^T \cdot \mathbf{F}^T \cdot \mathbf{F} \cdot d\mathbf{x} - d\mathbf{x}^T \cdot d\mathbf{x} = 2 d\mathbf{x}^T \cdot \mathbf{E} \cdot d\mathbf{x} \tag{2.9}$$

giving

$$\mathbf{E} = ½ (\mathbf{F}^T \mathbf{F} - \mathbf{I}) \tag{2.10}$$

On component form the Green strain tensor is given as:

$$E_{kl} = ½ (F_{mk} F_{ml} - \delta_{kl}) = E_{lk} \tag{2.11}$$

showing that this 2nd order tensor is symmetric.

By substituting equation (2.6) into the expression for the Green strain tensor, the general strain component E_{kl} can be expressed in terms of displacements in material coordinates as

$$E_{kl} = \frac{1}{2}\left(\frac{\partial u_k}{\partial x_l} + \frac{\partial u_l}{\partial x_k} + \frac{\partial u_m}{\partial x_k}\frac{\partial u_m}{\partial x_l} \right) \tag{2.12}$$

For the case of small strains but finite rotations as assumed for the present study, the Green strain tensor will be appropriate as a link between the kinematics and a constitutive model with assumptions of small strain, as it is invariant to rigid body rotations. The Green strain tensor is also computationally convenient, as the strains are readily available from the displacements that are the basic variables of the finite element displacement method.

2.3 STRESS AND EQUILIBRIUM

The surface traction, $\mathbf{t}$, at a point is defined as the ratio between an infinitesimal force and the infinitesimal area on which this force is acting. The Cauchy stress tensor, $\boldsymbol{\sigma}$, is defined by relating it to the surface traction by

$$\mathbf{t}(\mathbf{x}_t) = \mathbf{n}_t \cdot \boldsymbol{\sigma} \tag{2.13}$$

where $\mathbf{n}_t$ is the unit outward normal on the infinitesimal area dA_t. The Cauchy stress components, σ_{ij}, are identified as acting in the direction of the second index on a plane with outward normal in the direction of the first index. Cauchy stresses represent the physical stresses in the instantaneous position of the material point.

Physical stress components in the current configuration of a structure is a natural choice for stress output from a general nonlinear computer code as ABAQUS (1996) with respect to requirements from user interpretation of computed stress results.

Force equilibrium for an arbitrary material volume, V, acted upon by tractions **t** (force per unit area) on the surface S and body forces per unit volume **f**, is written:

$$\int_S \mathbf{t}\, dS - \int_V \mathbf{f}\, dV = 0 \tag{2.14}$$

By introducing Equation (2.13) and applying the Gauss theorem, the pointwise force equilibrium in the material volume is defined by

$$\left(\frac{\partial}{\partial \mathbf{x}_t}\right) \cdot \boldsymbol{\sigma} + \mathbf{f} = \mathbf{0} \tag{2.15}$$

The corresponding moment equilibrium of the material volume defines the symmetry of the Cauchy stress tensor.

The weak form of equilibrium in a finite element virtual work context can then be established. Several of the nonlinear constitutive models in ABAQUS are defined in terms of strain rate, and thus the rate of virtual work over the volume V is established from Equation (2.15) as:

$$\int_V \left[\left(\frac{\partial}{\partial \mathbf{x}_t}\right) \cdot \boldsymbol{\sigma} + \mathbf{f}\right] \cdot \delta \mathbf{v}_t\, dV = 0 \tag{2.16}$$

where $\delta \mathbf{v}_t = \delta \dot{\mathbf{x}}_t$ is the virtual velocity field. By using the Gauss theorem and the definition of Cauchy stress this equation can be written as

$$\int_V \boldsymbol{\sigma} : \left(\delta \frac{\partial \mathbf{v}_t}{\partial \mathbf{x}_t}\right) dV = \int_S t \cdot \delta \mathbf{v}_t\, dS + \int_V f \cdot \delta \mathbf{v}_t\, dV \tag{2.17}$$

The virtual velocity gradient can now be decomposed into a symmetric and an anti-symmetric part as follows:

$$\delta \frac{\partial \mathbf{v}_t}{\partial \mathbf{x}_t} = \frac{1}{2}\left(\delta \frac{\partial \mathbf{v}_t}{\partial \mathbf{x}_t} + \delta\left[\frac{\partial \mathbf{v}_t}{\partial \mathbf{x}_t}\right]^T\right) + \frac{1}{2}\left(\delta \frac{\partial \mathbf{v}_t}{\partial \mathbf{x}_t} - \delta\left[\frac{\partial \mathbf{v}_t}{\partial \mathbf{x}_t}\right]^T\right) = \delta\mathbf{D} + \delta\boldsymbol{\Omega} \tag{2.18}$$

where $\delta\mathbf{D}$ is the virtual strain rate and $\delta\boldsymbol{\Omega}$ the virtual rate of spin. Since $\boldsymbol{\sigma}$ is symmetric, $\boldsymbol{\sigma} : \delta\boldsymbol{\Omega} = 0$ and the rate of virtual work equation appears in the classical form as

$$\int_V \boldsymbol{\sigma} : \delta\mathbf{D}\, dV = \int_S \mathbf{t} \cdot \delta\mathbf{v}\, dS + \int_V \mathbf{f} \cdot \delta\mathbf{v}\, dV \tag{2.19}$$

Equation (2.19) identifies Cauchy stress and the strain measure with rate equal to **D** as work conjugate quantities as their product defines work rate per current volume. With the initial volume, V_0, as reference for a Lagrangian description of motion, the work conjugate stress measure to the strain with rate **D** is $J\boldsymbol{\sigma}$ according to:

$$\int_V \boldsymbol{\sigma} : \mathbf{D}\, dV = \int_{V_0} J\boldsymbol{\sigma} : \mathbf{D}\, dV_0 \tag{2.20}$$

where $J = dV / dV_0$ is the Jacobian of the elastic deformation between the initial natural reference volume and the current volume. The stress measure, $J\boldsymbol{\sigma}$, referred to the initial reference volume is called Kirchhoff stress and this tensor is often denoted $\boldsymbol{\tau}$.

In the previous section Green strains were selected as a convenient and appropriate strain tensor for the present study. The corresponding work conjugate stress measure is the second Piola-Kirchhoff stress tensor. The rate of Green strains can be related to the strain measure whose rate is the rate of deformation:

$$\begin{aligned} \dot{\mathbf{E}} = \frac{1}{2}\left(\dot{\mathbf{F}}^T \cdot \mathbf{F} + \mathbf{F}^T \cdot \dot{\mathbf{F}}\right) = \frac{1}{2}\left(\left(\frac{\partial \mathbf{v}_t}{\partial \mathbf{x}_t} \cdot \mathbf{F}\right)^T \cdot \mathbf{F} + \mathbf{F}^T \cdot \left(\frac{\partial \mathbf{v}_t}{\partial \mathbf{x}_t} \cdot \mathbf{F}\right)\right) = \\ \frac{1}{2}\mathbf{F}^T \cdot \left(\frac{\partial \mathbf{v}_t}{\partial \mathbf{x}_t} + \left(\frac{\partial \mathbf{v}_t}{\partial \mathbf{x}_t}\right)^T\right) \cdot \mathbf{F} = \mathbf{F}^T \cdot \mathbf{D} \cdot \mathbf{F} \end{aligned} \tag{2.21}$$

The right hand side of Equation (2.20) thus gives

$$\int_{V_0} J\boldsymbol{\sigma} : \mathbf{D}\, dV_0 = \int_{V_0} J\boldsymbol{\sigma} : \left(\mathbf{F}^{-T} \cdot \dot{\mathbf{E}} \cdot \mathbf{F}^{-1}\right) dV_0 = \int_{V_0} J\left(\mathbf{F}^{-T} \cdot \boldsymbol{\sigma} \cdot \mathbf{F}^{-1}\right) : \dot{\mathbf{E}}\, dV_0 \tag{2.22}$$

which defines the second Piola-Kirchhoff stress tensor

$$\mathbf{S} = J\mathbf{F}^{-1} \cdot \boldsymbol{\sigma} \cdot \mathbf{F}^{-T} \tag{2.23}$$

as being work conjugate to Green strains.

For a case with small strains but arbitrarily large rotations the components of **S** can be interpreted as the rotated axis components of $\boldsymbol{\sigma}$. The components of **S** are thus the stress components associated with directions in the reference configuration.

The constitutive relationships for path dependent materials in general are formulated on rate form in ABAQUS. This formulation is also adopted for metals with

elastoplastic behaviour. A natural state of reference for the elastic response is the unstressed initial state. With Cauchy stress as the desired output stress measure, Equations (2.20) and (2.22) point out the Kirchhoff stress, $\boldsymbol{\tau} = J\,\boldsymbol{\sigma}$ as being conjugate to the strain measure with rate equal to the rate of deformation and referred to the initial configuration. Equation (2.21) gives the relationship between the rate of the Green strain tensor, and the rate of deformation.

2.4 ELASTO-PLASTIC MATERIAL BEHAVIOUR

The isotropic metal plasticity model in ABAQUS (1996) is applied. It is based on the von-Mises yield criterion with associated plastic flow according to coinciding yield function and plastic potential function. Isotropic strain hardening behaviour of the specific titanium alloy selected for this study is confirmed by the material tests reported in Chapter 3.

A fundamental assumption of the applied plasticity theory, is the additivity of elastic and plastic strains. This is assured for the co-rotational incremental solution procedure, cf. Section 2.5.1.

The integration of the plasticity model is based on the backward Euler method with Newton iterations to satisfy the consistency conditions which ensure that the stress state remains on the yield surface at the end of each load increment.

Details of the theory and the algorithms are given in ABAQUS (1996).

2.5 SOLUTION PROCEDURE

2.5.1 Basic Equations

The incremental solution of the history dependent equilibrium equations implied by the rate of virtual work of Equation (2.19) is in ABAQUS based on the Newton algorithm.

Following the discussion in Section 2.3, the left hand side of Equation (2.19) can be replaced by the integral over the reference volume of the virtual work rate per unit volume defined by any conjugate pair of material stress and rate of strain. With the second Piola–Kirchhoff stress tensor and the rate of Green strain, the rate of virtual work equation becomes:

$$\int_{V_0} \mathbf{S} : \delta\dot{\mathbf{E}}\, dV_0 = \int_S \mathbf{t}^T \cdot \delta\mathbf{v}\, dS + \int_V \mathbf{f}^T \cdot \delta\mathbf{v}\, dV \tag{2.24}$$

Incremental stiffness for the Newton algorithm is established from the variation of Equation (2.24). By introducing the velocity field in the virtual work equations in terms of interpolation functions between finite element nodal displacement variables, the linear variation with respect to these variables is denoted d( ). Equation (2.24) thus gives:

$$\int_{V_0}\left(d\mathbf{S}:\delta\dot{\mathbf{E}}+\mathbf{S}:d\delta\dot{\mathbf{E}}\right)dV_0 = \int_S\left(d\mathbf{t}^T\cdot\delta\mathbf{v}+t^T\cdot\delta\mathbf{v}\,dA_r\,\frac{1}{A_r}\right)dS+\int_V\left(d\mathbf{f}^T\cdot\delta\mathbf{v}+\mathbf{f}^T\cdot\delta\mathbf{v}dJ\,\frac{1}{J}\right)dV \tag{2.25}$$

where A_r is the surface area ratio between the current and the reference configuration and thus defined by $A_r = |dS/dS_0|$.

The first term on the left hand side of Equation (2.25) will give rise to the incremental material stiffness, while the second term gives rise to the 'initial stress' or geometric incremental stiffness. With pressure loading acting normal to the instantaneous position of the element surface, the variation of the surface integral term of Equation (2.24) introduces incremental rate of virtual work by displacement dependent loading. The first term of the surface integral on the right hand side of Equation (2.25) is then related to the change in the load magnitude and the normal direction of the surface, while the second term is related to change or deformation of the surface area. In the finite element model the displacement dependent force increments implied by the surface integral can be expressed as the product of an incremental 'surface load stiffness' and the increment in nodal displacement variables.

ABAQUS applies a co-rotational Lagrangian incremental description of motion. Rigid body rotations or the local spin between successive configurations can thus be subtracted prior to establishing the state of strain from displacements. Similarly, the physical stress increments can be subdivided into one part associated with the local spin of the stress tensor and one part related to the strain through the constitutive relationship.

2.5.2 Equilibrium Iterations

At the end of each load increment there may result a force unbalance between the external load level represented by the vector, $\mathbf{R}^E$, and the nodal forces corresponding to the state of stress in the elements. These latter forces are assembled in the vector $\mathbf{R}^I(\mathbf{r})$ at system level. The deformation dependency of $\mathbf{R}^I$ of the state of deformation is indicated by the argument $\mathbf{r}$, the system vector of nodal displacements.

Equilibrium is obtained if the force unbalance is zero according to

$$\mathbf{R}(\mathbf{r}) = \mathbf{R}^E - \mathbf{R}^I(\mathbf{r}) = 0 \tag{2.26}$$

The Newton incremental method with iterations is used to establish the vector **r** that satisfies Equation (2.26) to a specified level of accuracy.

After iteration *i*, an approximation of $\mathbf{r}_i$ is obtained. Let $\mathbf{\Delta}_i$ be the difference between $\mathbf{r}_i$ and the solution satisfying Equation (2.26). Thus

$$\mathbf{R}(\mathbf{r}_i + \mathbf{\Delta}_i) = 0 \tag{2.27}$$

Expanding the left hand side in a Taylor series about the approximate solution $\mathbf{r}_i$, the following relation appears:

$$\mathbf{R}(\mathbf{r}_i) + \frac{\partial \mathbf{R}(\mathbf{r}_i)}{\partial \mathbf{r}} \cdot \mathbf{\Delta}_{i+1} + \frac{\partial^2 \mathbf{R}(\mathbf{r}_i)}{\partial \mathbf{r}^2} \cdot \mathbf{\Delta}_{i+1}^2 + \cdots = 0 \tag{2.28}$$

The magnitude of the displacement difference, $\mathbf{\Delta}_{i+1}$, will be small if $\mathbf{r}_i$ is a close approximation to the solution. Hence, all but the first two terms in Equation (2.28) can be neglected. This implies:

$$\frac{\partial \mathbf{R}(\mathbf{r}_i)}{\partial \mathbf{r}} \cdot \mathbf{\Delta}_{i+1} = \mathbf{K}_{ti} \cdot \mathbf{\Delta}_{i+1} = -\mathbf{R}(\mathbf{r}_i) \tag{2.29}$$

where $\mathbf{K}_{ti}$ is the tangential stiffness matrix for iteration step no. *i*. The solution for $\mathbf{\Delta}_{i+1}$ is now found from:

$$\mathbf{\Delta}_{i+1} = \mathbf{K}_{ti}^{-1} \cdot (-\mathbf{R}(\mathbf{r}_i)) \tag{2.30}$$

The updated displacement vector after iteration *i* is now

$$\mathbf{r}_{i+1} = \mathbf{r}_i + \mathbf{\Delta}_{i+1} \tag{2.31}$$

As convergence criterion, ABAQUS uses the following inequality:

$$r_{\max} \le R_n \cdot \widetilde{q} \tag{2.32}$$

where r_{max} is the largest residual and $\widetilde{q}$ is an averaged value of $\overline{q}$ over all previous increments. $\overline{q}$ is the instantaneous magnitude averaged over the entire model. R_n is the specified accuracy of the convergence criterion, which is set equal to 0.5 % in ABAQUS. If the inequality in Equation (2.32) is satisfied, convergence is accepted.

2.5.3 The RIKS-method in ABAQUS

The equilibrium path for collapse behaviour of structures is usually a non-linear surface representing the load-deformation history in a multi-dimensional space defined by the nodal variables and the loading. The maximum bending moment capacity for the present FE-analyses is represented by a limit point on the load-displacement curve for the actual problem. To pass this limit point in the nonlinear shell analyses, a so-called 'arc-length' method is used. The method, also known as constraining surface approach, is called RIKS-method, Riks (1979).

The basic idea of this method is, however, modifying the load level at each iteration rather than holding the applied load level constant during a load increment. Essentially, all constraint methods involve the addition of an auxiliary equation that constrains the iterative displacements to follow a specified path towards a converged solution. For an 'arc length' method this constraint equation can be expressed as

$$c = \sqrt{\Delta \mathbf{r}^T \cdot \Delta \mathbf{r} + \Delta\lambda^2 \psi^2 \Delta \mathbf{R}^T \cdot \Delta \mathbf{R}} - \Delta l = 0 \tag{2.33}$$

where

$\Delta \mathbf{r}$	incremental displacement vector
$\Delta\lambda$	incremental load factor
ψ	scaling factor between load and displacement
$\Delta \mathbf{R}$	incremental load vector
Δl	specified 'radius' (length) of the arc which is normal to the tangent of the equilibrium surface, see Figure 2.3.

Equation (2.33) is visualised in Figure 2.3.

The material has path dependent response and it is thus essential to limit the size of the increment Δl (distances from A_0 to A_1 in Figure 2.3). In ABAQUS this is done by moving a specified distance along the tangent line from the current solution point (A_0 to A_1), and then searching for equilibrium in the plane normal to the tangent direction of the load step. The projection of the residual forces (ρ_1) is accounted for so that the point of equilibrium calculation is moved from A_1 to A_2. This procedure is repeated until satisfactory convergence is reached.

The procedure implemented in ABAQUS is modified from the original RIKS method as the tangential direction is updated prior to each iteration. This implies that the equilibrium search shall be orthogonal to the last tangent, rather than the tangent at the beginning of the load increment. One of the main reasons for this modification is related to the solution procedures for the plasticity problems, where the first iteration of each increment applies the elastic material stiffness to establish the direction of straining.

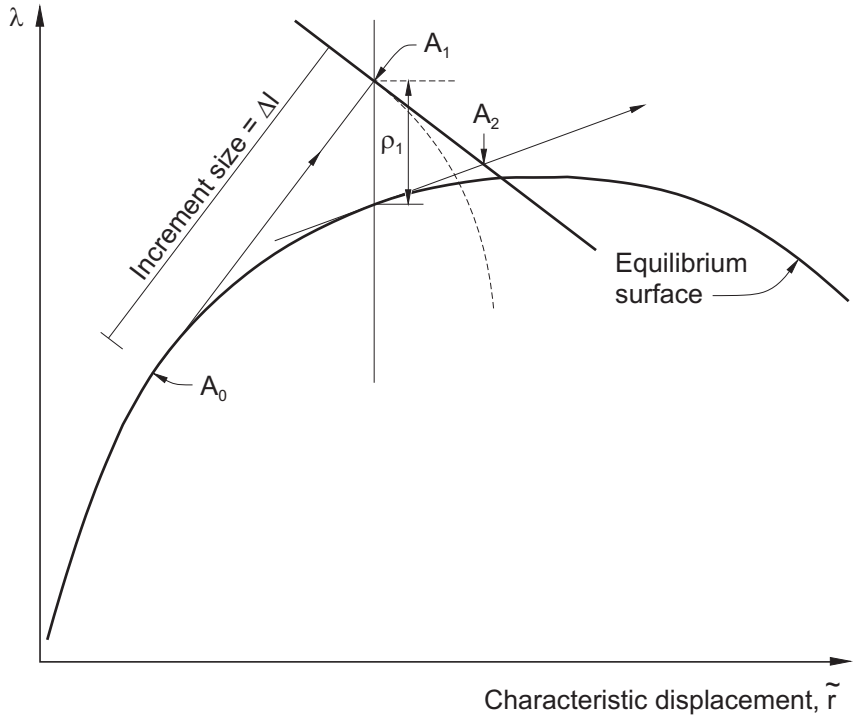

Figure 2.3 Schematic view of the modified RIKS-method.

C h a p t e r 3

MATERIAL AND GEOMETRY DATA

"The Young's modulus does not describe a material completely."
Lecture notes for architect students, Faculty of Architecture,
Norwegian University of Science and Technology, 1998/99.

3.1 INTRODUCTION

The material properties are important input parameters when numerical simulations are used to study the behaviour and strength of titanium pipes in failure modes that imply elasto-plastic material behaviour.

The material properties of two titanium pipes are studied from tensile test specimens. To establish the variation of the material properties in terms of the relevant parameters as Young's modulus, yield stress, strain hardening parameters, ultimate stress and possible anisotropy.

The uniaxial tensile test specimens are selected out to acquire the variation of the material properties over the pipe cross-section and along the pipe. The anisotrophy is investigated from test specimens in three different directions: 0°, i.e. along the pipe, 45° and 90°.

3.2 TITANIUM RISER MATERIAL

3.2.1 Titanium Alloys for Riser Application

Relevant background information for titanium alloys is provided in this section, and is, if not otherwise specified, based on Lunde et al. (1995), Gorynin et al. (1995), Tetyunkhin et al. (1996), Tetyunkhin & Smirnov (1996), Baxter & Schults (1996) and Salama et al. (1998).

The titanium alloys are divided into separate grades, depending on the alloying elements. One of the 'base alloys', is Ti-6Al-4V, denoted Grade 5, Boyer et al. 1994. This specific grade consists of about 6 % aluminium, 4 % vanadium and normal interstitial content of oxygen and hydrogen. Another commercially available alloy is Ti-6Al-4V ELI (Grade 23), which is quite similar to Grade 5, but with extra low interstitial content of oxygen and hydrogen. Adding ruthenium (Ru) or palladium (Pd) (Grade 29 and 24, respectively), improves the corrosion resistance significantly while the mechanical properties are maintained as for grade 23. Table 3.1 gives the chemical composition of Grades 5 and 23 (24, 29).

Table 3.1. Chemical composition of grades 5 and 23 (24, 29). The numbers in the table corresponds to % of weight.

Grade	Aluminium (Al)	Carbon (C)	Iron (Fe)	Hydrogen (H)	Nitrogen (N)	Oxygen (O)	Vanadium (V)
5	5.5-6.75	.1	.4	.0125-.015	.05	.2	3.5-4.5
23	5.5-6.75	.1	.25	.0125-.015	.05	.13	3.5-4.5

When it comes to the microstructure of titanium alloys, the solid phase consists of two main crystallisation types, called α and β. The former is a close packed hexagonal structure, while the latter is a body centred cubic structure. By introducing different elements in the alloy, a stabilising effect of either α- or β-phases is possible. Aluminium and vanadium stabilise the α- and the β-crystals, respectively. A microstructure combining both phases may result in high strength. The α-β-phase is stable from room temperature up to 1025 °C. The β-phase alone is stable above 1025°C, while α alone is unstable.

Seamless titanium pipes for marine applications are being manufactured by a forging process, i.e. hot extrusion and hot rolling (rotary piercing or press piercing). This may be done for diameters up to 30 inches, Berge (1998). Additionally, thermal treatment is applied to create different combinations of the α- and β-crystals. To prevent

absorption of unfavourable elements (N_2, O_2, H_2), the heating must be performed in either vacuum or in an inert gas atmosphere (e.g. argon, helium). Two different types of heat treatment is commonly used, Donachie (1988):

- Annealing: This method is used to obtain an increased toughness and ductility. The material is either in the $\alpha+\beta$-phase or in the 'pure' β-phase.

- Solution treatment, quenching and ageing (in subsequent order): This method is frequently used to obtain high tensile strength. The material is heated above the β-transus and cooled quickly in either water or oil (quenched). The alloy is then aged and air-cooled.

The alloy is also machined. This treatment is intended to remove some of the outer part of the material surface. Due to the cooling process, nitrogen (N_2), oxygen (O_2) and hydrogen (H_2), may penetrate into the material. This is unfavourable from a mechanical point of view since it may introduce dislocations in the material, which again reduces the strength and the fatigue properties. The material can also become more brittle if dislocations are present.

Furthermore, alloys may be pickled, implying that moisture oxides and grease are removed from the surface. This is normally performed just prior to welding of the pipe segments. If these organic materials are not removed before welding takes place, porosities (e.g. water particles) may be introduced. Such small defects can initiate cracks, which obviously are unfavourable from a fatigue point of view. Regarding fatigue, this phenomenon is dependent on defects from e.g. machining, surface condition, microstructure, and environment. It is also important to emphasise, contrary to steel, that microstructure, temperature, and interstitial content significantly influence the crack growth rate in titanium.

3.2.2 Titanium Material for the Present Study

The titanium alloy in the pipes provided for testing in this study is Ti-6Al-4V ELI/Pd (Grade 24), manufactured by Deutsche Titan GMBH. The pipe sections had a mean diameter equal to 170 mm (6.7 in) and nominal wall thickness of 16 mm, see Section 3.3.

The pipe tested in the laboratory is extruded, heat treated, machined and pickled Furthermore, the pipe is hot rolled at high temperatures, and seamless. It is heated above β-transus, i.e. the temperature above which the β-crystallisation phase is stable. By heating the material above the α-region (i.e. temperatures above 1025 °C), the growth of β-crystals is favoured.

Furthermore, the material is cooled slowly, not quenched, implying that some β crystals are converted to the α-phase. Hence, the alloy has both α and β crystalline structure, which is favourable from a tensile strength's point of view.

3.3 UNIAXIAL TENSION TESTS

3.3.1 Test Specimens and Test Setup

The properties of the employed titanium material are obtained from experiments in the laboratory performed on samples cut from the pipes identified in the previous section, Tryland et al. (1997). Forty uni-axial tension tests along four different directions are investigated. The geometry of each test specimen is shown in Figure 3.1.

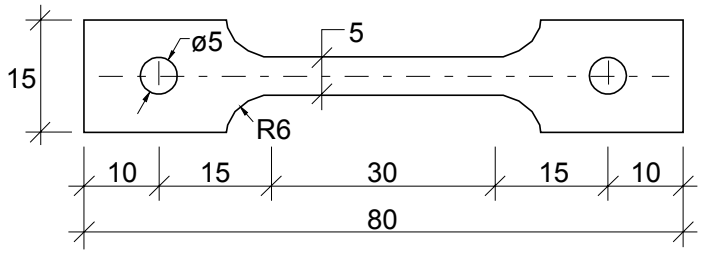

Figure 3.1 The geometry of the test specimens. The nominal thickness is 3 mm.

The load during the tests is measured by a 100 kN load cell. The strain in the longitudinal direction is measured by an extensometer with a gauge length of 12.5 mm. The tests are performed by applying a strain rate of about 5.0 E-4 s^{-1}. The width and thickness of the specimen's gauge area are measured before testing and after tensile rupture.

To identify possible anisotropy, the tensile specimens are taken along four different directions in the pipe-wall, see Figure 3.2. The specimens in the longitudinal directions are cut from the different cross-sectional locations in K (inner position), L (outer position) and M (mean position) and longitudinal locations SI, SII. W is to be interpreted as the position around the pipe in hoop direction, i.e. has values of either 1 or 2 representing two separate halves of the pipe.

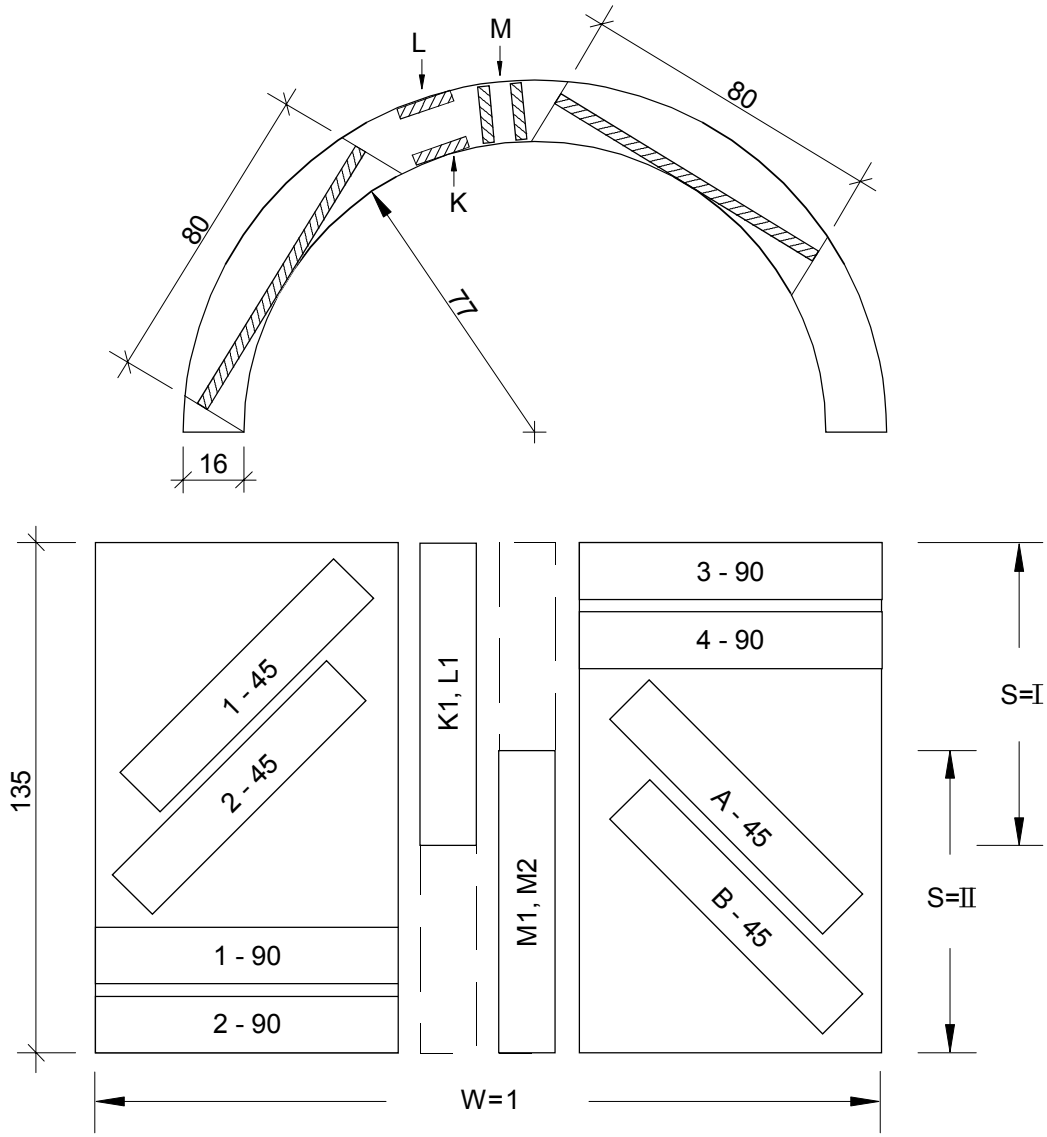

Figure 3.2 Location and orientation of test specimens.

The factors that may influence the values of the relevant parameters from the laboratory tests are identified as given in the list below. Three different levels for each of the factors are selected, i.e. high, medium and low level.

1. The orientation of the specimen relative to the pipe axis, O, gives the angle between the tensile axis and the axial direction of the pipe: O = 0°, 45° and 90° (where the axial direction corresponds to O = 0°).

2. The cross-section part, W, defines the different parts of the pipe cross-section: W =1, 2.

3. The positions, P, corresponding to three separate locations through the thickness, i.e. inner (K), outer (L) and middle (M). Hence, P = K, L, M.

4. The section, S, which defines two different locations along the test pipe (S = I, II).

5. The two possible 45° orientations, are herein denoted 1-45, 2-45, ... and A-45, B-45, ..., respectively. See Figure 3.2.

If the test program and experiments are conducted for all possible combinations of the different variables defined above, the total number of tests is (3 x 2 x 3 x 2 x 2) 72. A factorial design method is employed in order to obtain the characteristic data from a reduced number of tests, Box et al. (1978).

A $4x2^{2-1}$ experimental design method is chosen to identify the relevant material parameters. Two replicates are used implying that 16 tests are required. The investigated factors are as follows: section (S), cross-section part (W) and orientation/position (O/P). Four levels of the factor O/P are defined as follows: O/P=0°/M, 45°/K, 90°/K, 0°/(K or L). See Figure 3.2 for further details.

3.3.2 Test Results

The material characteristics, Young's modulus (E), ultimate strength (σ_u), stress levels at 0.01 % ($\sigma_{0.01}$), 0.02 % ($\sigma_{0.02}$) and 0.05 % ($\sigma_{0.05}$) of plastic strain are identified from the laboratory tests. The ultimate plastic strain, ε_u, is identified and defined on the basis of the initial and final geometry of the specimen in the fracture zone. This is done because of the high stress level combined with a low Young's modulus implying that the elastic energy (W_e = 1/2 σ^2/E) is large. The extensometer is removed to avoid damage of this instrument at a strain level of 5 % (i.e. before rupture). The ultimate plastic strain may thus be defined as follows:

$$\varepsilon_u = \ln\left|\frac{A_o}{A_f}\right| = \ln\left|\frac{t_o w_0}{t_f w_f}\right|$$

where A_0, t_0, w_0 and A_f, t_f, w_f refer to initial and final geometry, respectively. w_0 and t_0 are initial width and thickness of the specimen in the gauge area, while w_f and t_f are the same measures after rupture.

Furthermore, in order to determine possible anisotropy, the response parameter (the so-called R-value), $R = \ln(w_f / w_0) / \ln(t_f / t_0)$, is computed, Hosford & Caddell (1993).

Table 3.2 presents the mean values and the corresponding standard deviations of the material characteristics. The standard deviations are given in brackets. The results are given for both the 16 tests in Series I and the 24 tests in Series II. Both possible 45° orientations are investigated in Series II. Stress-strain relationships for the mean and 5 % upper and lower curves are given in Figure 3.3.

From Table 3.2 is noted: The parameters σ_M and σ_H are the average strength and standard deviation of σ_M in the strain range from 0.5 % up to 5 %, respectively. This means, that σ_M is calculated based on the average of the stresses for 26 different values of the strain for both the total strain ranges between 0.5 % and 1.0 % and from 1 % up to 5 %. This particular subdivision of the strain range is made to obtain a good representation of the stress-strain relationship for the part of the curve with the largest gradients of the stress-strain curve in the plastic range. This is for small strains due to the low strain hardening of this specific titanium alloy. A high and a low value of σ_H represents a high and low strain hardening. ε_f represents fracture strain, which corresponds to σ_f, see the end points of the three curves in Figure 3.3. ε_u is the strain at which the corresponding stress, σ_u, has its maximum.

Based on the laboratory results, the following conclusions and observations are made:

- The material behaviour for the present titanium pipe can be modelled as isotropic. Anisotropic effects are very small for the present test data.

- Large variations in the fracture strain are observed. The lowest and the largest values observed are 3 % and 12 %, respectively.

- The strain hardening is low. The stress at ultimate strain is about 10 % above the yield stress.

Reasons for the relatively large variations in the test results for the fracture strain and the ultimate strain may partly be found in the properties of the small test specimens. Eccentricities and surface roughness may cause inaccuracies. However, the present test specimens were carefully examined, and there is no reason to believe that such effects have significantly influenced the material characteristics of the present laboratory tests.

Table 3.2. Mean values and standard deviations (in parenthesis) from 40 titanium tests.

	Series I									Series II			
S.o.v.	E (MPa)	$\sigma_{0.01}$ (MPa)	$\sigma_{0.05}$ (MPa)	$\sigma_{0.2}$ (MPa)	σ_M (MPa)	σ_H (MPa)	σ_u (MPa)	ε_u (%)	R	σ_u (MPa)	ε_u (%)	ε_f (%)	R
All	119176	685.1	763.7	827.8	890.2	18.07	911.8	5.92	1.05	900.7	5.22	8.35	1.13
	(5685)	(11.9)	(11.3)	(12.9)	(10.5)	(1.04)	(11.0)	(1.75)	(0.15)	(12.5)	(1.52)	(2.79)	(0.16)
O=0°	119530	681.6	759.6	821.4	884.9	17.89	905.9	4.98	1.04	888.3	5.19	8.20	1.23
	(4197)	(11.8)	(10.3)	(9.1)	(9.2)	(0.55)	(9.9)	(1.02)	(0.18)	(8.8)	(1.44)	(2.10)	(0.20)
O=45°	121065	693.6	772.4	841.2	899.1	17.48	920.9	7.60	1.00	901.8	4.80	6.93	1.03
	(10214)	(8.3)	(6.3)	(12.5)	(7.3)	(1.53)	(6.5)	(1.37)	(0.05)	(8.5)	(2.08)	(3.59)	(0.13)
O=90°	116577	683.4	763.2	827.2	892.1	19.03	914.7	6.14	1.12	912.0	5.66	9.94	1.14
	(1432)	(13.5)	(14.3)	(11.8)	(10.4)	(0.76)	(11.0)	(2.18)	(0.12)	(6.2)	(0.87)	(1.74)	(0.07)
W=1	118872	686.6	765.4	828.2	892.6	18.65	914.9	6.11	1.00	901.8	5.32	8.73	1.11
	(4156)	(15.3)	(12.4)	(11.5)	(9.7)	(0.65)	(10.8)	(2.23)	(0.11)	(13.4)	(1.64)	(2.71)	(0.12)
W=2	119479	683.5	762.1	827.4	887.9	17.50	908.7	5.75	1.10	899.5	5.12	7.98	1.15
	(7195)	(8.0)	(10.7)	(15.0)	(11.3)	(1.07)	(11.0)	(1.22)	(0.16)	(12.0)	(1.46)	(2.93)	(0.19)
S=1	118389	684.9	762.2	824.6	887.2	18.07	909.4	6.42	1.05	903.3	5.07	8.33	1.10
	(4574)	(12.6)	(11.9)	(12.0)	(10.7)	(0.54)	(11.7)	(1.57)	(0.20)	(9.4)	(1.72)	(2.53)	(0.16)
S=2	119962	685.2	765.3	831.0	893.3	18.07	914.3	5.42	1.05	898.1	5.37	8.38	1.17
	(6849)	(12.1)	(11.3)	(13.8)	(9.9)	(1.43)	(10.4)	(1.87)	(0.08)	(14.9)	(1.35)	(3.14)	(0.16)
0°/M	119067	681.8	756.1	818.1	882.7	17.95	903.8	5.09	1.11	886.0	5.94	9.65	1.29
	(3139)	(16.7)	(12.6)	(10.7)	(12.8)	(0.78)	(14.2)	(1.20)	(0.19)	(8.2)	(0.87)	(1.39)	(0.10)
0°/K	119993	681.4	763.2	824.7	887.0	17.83	908.0	4.86	0.97	890.5	4.44	6.75	1.16
or L	(5539)	(7.0)	(7.4)	(7.1)	(4.6)	(0.32)	(3.4)	(0.98)	(0.17)	(10.0)	(1.62)	(1.64)	(0.27)
45°/	-	-	-	-	-	-	-	-	-	904.5	4.50	7.23	0.95
1,2,...										(11.0)	(2.23)	(2.93)	(0.13)
45°/	-	-	-	-	-	-	-	-	-	899.0	5.10	6.63	1.11
A,B,...										(5.1)	(2.21)	(4.60)	(0.08)

S.o.v: Source of variation.

Figure 3.3 represents the mean and the 5 % upper and lower stress-strain curves from the tests. It clearly shows the large variation in fracture strain for the titanium alloy. The largest fracture strain is 12 %, while the lowest value is only 3 %. Furthermore, it can also be concluded from Figure 3.3 that the ratio between the ultimate stress and the yield stress is relatively low (equal to 1.1 for this specific titanium grade).

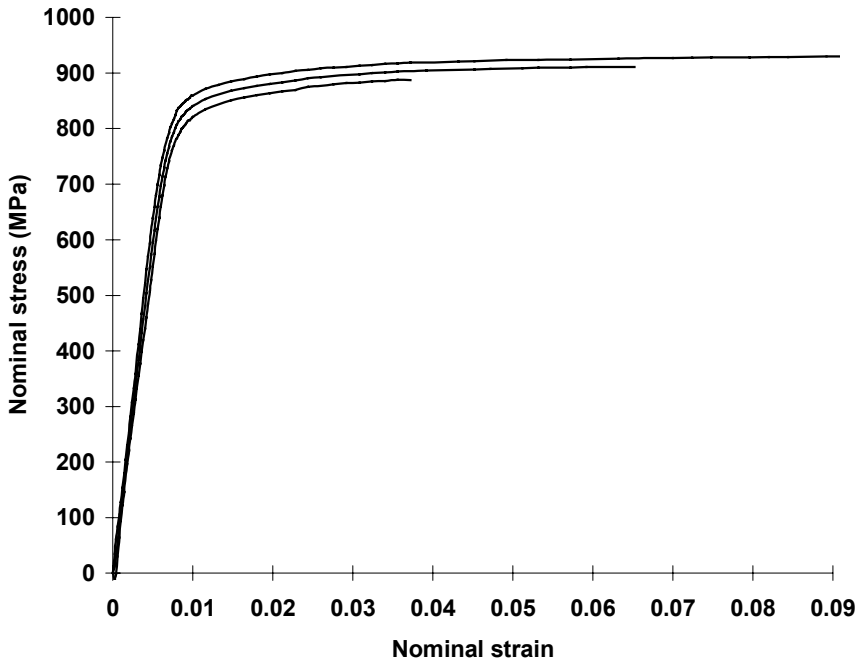

Figure 3.3 σ-ε-curves for mean and 5 % upper and lower curves.

3.4 WALL THICKNESS VARIATION

The wall thickness variation is also identified for the pipe tested in the laboratory. This is done by measuring the wall thickness at 32 points at both ends by means of a digital micrometer. The variation is shown in Figure 3.4, where the values for both ends relative to the nominal value are given.

The wall thickness varies from –5.4 % to +21.8 % relative to the nominal value. The reason for this variation is most likely the manufacturing process (hot rolled and extruded). When extruding a pipe, the locations of the centre of the rotating piercer and the centre of the pipe are of major interest. If they match perfectly, the pipe will (theoretically) have a constant wall thickness in the circumferential direction. However, this optimal production process is very difficult to achieve in practice, due to production methods, fabrication tolerances etc. Accordingly, a certain variation of the wall thickness in the circumferential direction is expected. Furthermore, this variation will have a shape like a harmonic mathematical function (sine or cosine) due to the rotating piercer when the pipe is being extruded. In Figure 3.4, a sine-function is fitted to the curve with the greatest range of variation. It is seen that some deviations are present. However, both low and high values are represented by the harmonic function.

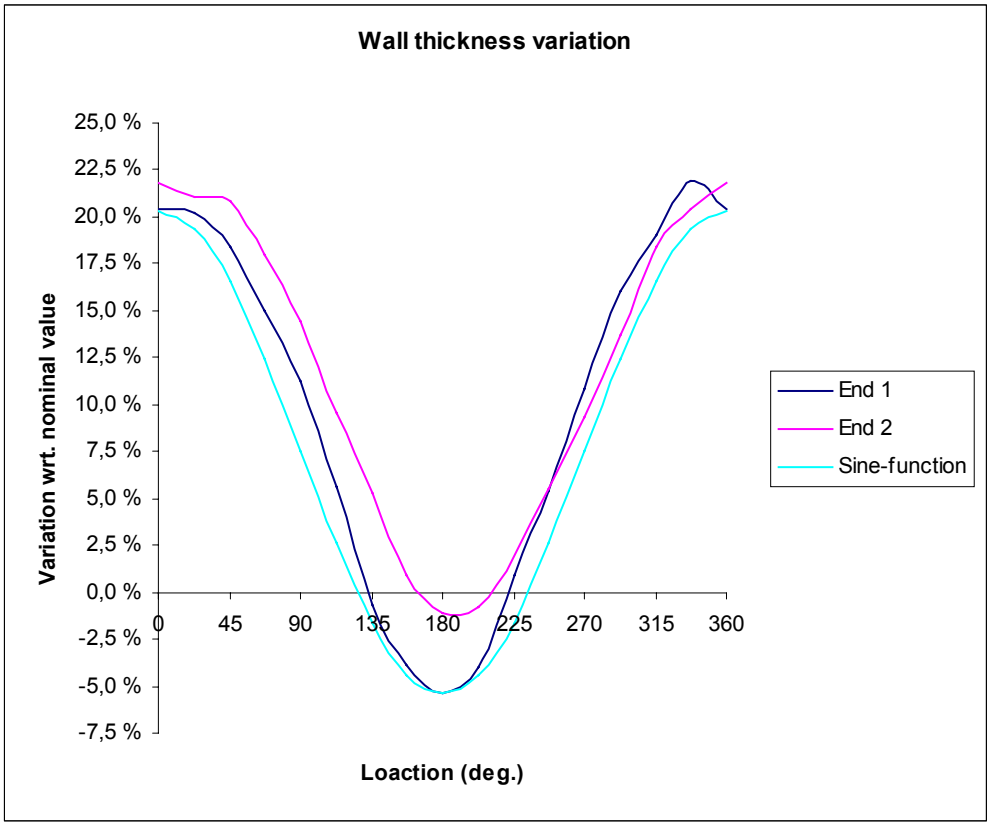

Figure 3.4 Wall thickness variation in circular directions normalised with respect to the nominal value.

C h a p t e r 4

GLOBAL AND LOCAL RISER MODELING

"A theory has only the alternative of being right or wrong.
A model has a third possibility; it may be right, but irrelevant."
Manfred Eigen (1927-)

4.1 INTRODUCTION

The main objective of this chapter is to outline the analyses of estimates of the maximum bending moment capacity in the sag-bend for a specified deep water titanium riser. The analyses combine a global beam model and a local finite element shell model. The beam model is integrated in a floater motion analysis and provides stress resultants to the shell modelling of the risers in the sag-bend area.

4.2 GLOBAL ANALYSIS

4.2.1 Global Modelling of the Riser and the Sea Bed

The global model represents a catenary riser as shown in Figure 1.1. Static and dynamic response analyses are performed with the computer program RIFLEX (1995).

The riser is modelled with constant axial, bending and torsion stiffness throughout the length. A ball joint connector is located at the top of the riser at the surface vessel, which is a tension leg platform (TLP).

The transfer functions for the TLP motions used in the RIFLEX analyses are representative for a deep-water configuration. The heave motions are, very small compared to the surge motions.

The static mean configuration of the riser during the analyses corresponds to the near position of the vessel, see Figure 4.1. This specific location of the vessel is associated with an offset equal to 10 % of the water depth relative to the mean position. Static offset is defined as positive in the direction from the mean position towards the near position. A static offset equal to -10 % of the water depth is referred to as the far position in Figure 4.1.

Damping is assumed to be proportional to the stiffness, which means increased damping with frequency. It is common practice to let stiffness-proportional damping correspond to 1-2 % of the critical value for the first mode, RIFLEX (1995), and 1.5 % of the critical damping of the 1st mode is chosen for the present analyses.

Wave loading is applied to the floater and the riser, and is represented by regular waves that are propagating in the same direction as the static offset. A load-duration of five wave periods is employed in the regular wave analysis to achieve stationary response. Regular waves are considered to be better suited for parameter studies of isolated response parameters, avoiding variability in excitation from irregular wave trains. Furthermore, the purpose of the global riser analyses is to obtain a reasonable relationship between the axial and shear force and bending moment in the sag-bend region. The maximum bending moment in the sag-bend and corresponding axial and shear forces are the response parameters of major interest from the global motion analysis of the riser. The maximum response parameters are calculated for the combinations of the 100 year wave height with the 10 year current velocity and also for the 10 year wave height with the 100 year current velocity, DnV (1988). The condition implying the largest bending moment in the sag-bend is used as the basis for further calculations with the local riser model in Chapter 5. The internal pressure of the riser is set equal to zero to obtain maximum pressure difference. This may correspond to possible conditions in the installation phase and during production shut-down.

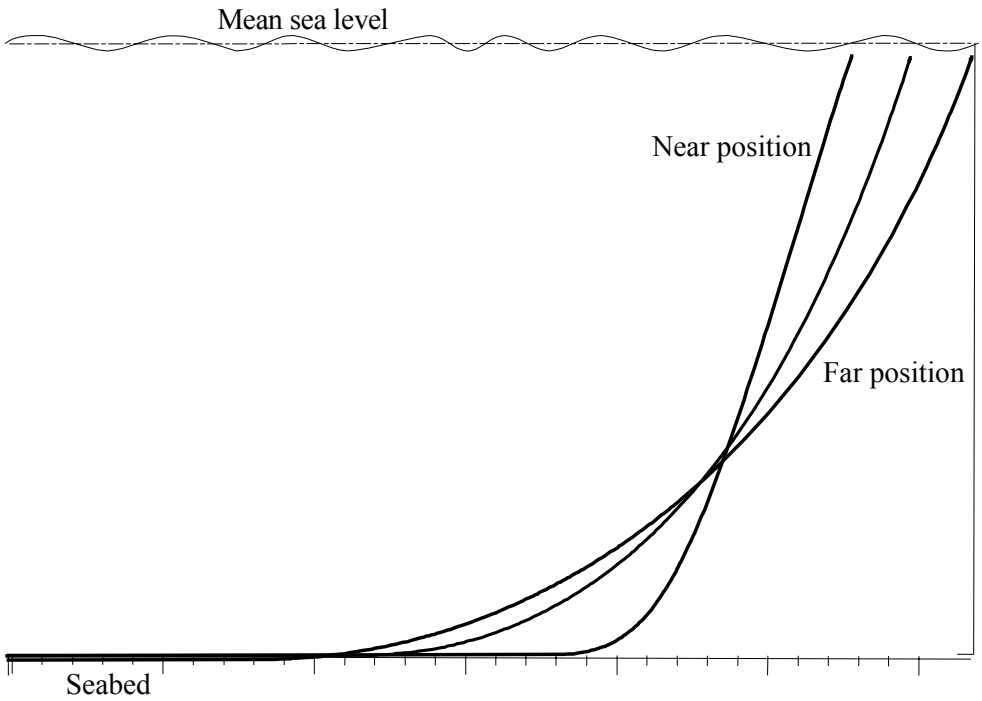

Figure 4.1 An illustration of the riser when the vessel is located in the near, mean and far positions.

The riser may buckle as a beam-column if the effective axial forces become compressive over an extended length of the riser, see e.g. Larsen (1995), DnV (1996) and API (1998). Furthermore, the riser is more sensitive to dynamic loading if its submerged weight is low. This implies larger dynamic motions. Since the density of titanium is relatively low, it may thus be required to add weight to a titanium riser to satisfy mechanical limit state criteria.

Distributed additional weight in the present study is included through an equivalent metal density of about twice that of most titanium alloys ($\rho_{titanium} \sim 4500$ kg/m^3). Wall thickness sizing is based on strength requirements, and does not include weight considerations. Since titanium is a relatively expensive material, increased weight may be obtained by the use of other materials. In the present study, additional weight is considered not to contribute to the strength or capacity of the riser cross sections.

The computational model is thus established with an equivalent material density equal to 10430 kg/m^3. This corresponds to a specific gravity ratio of 1.45 (this ratio is given as the submerged weight including content plus buoyancy (positive value) divided by the buoyancy, DnV (1988)). This is observed to be applicable for a stable catenary riser configuration at similar water depths connected to this type of floater, Bjørset & Leira (1996). The top tension is increased by the increased weight. This leads to lower

probability of negative effective axial forces in the sag-bend region when the vessel is located in the near position, as demonstrated for the case studies below.

Figure 4.2 verifies that increased weight leads to more positive effective axial forces in the sag-bend region. Figure 4.2a is an effective axial force diagram for a riser with a specific gravity of 1.2. The dotted line represents the static values, which for this particular position are negative for the touch-down point and the rest of the riser resting at the sea bed. The continuous lines represent the sum of static and dynamic values of the effective axial force. Figure 4.2b shows the effective axial force diagram for a specific gravity equal to 2.0. Obviously, the minimum values have increased significantly from –40 kN to 80 kN.

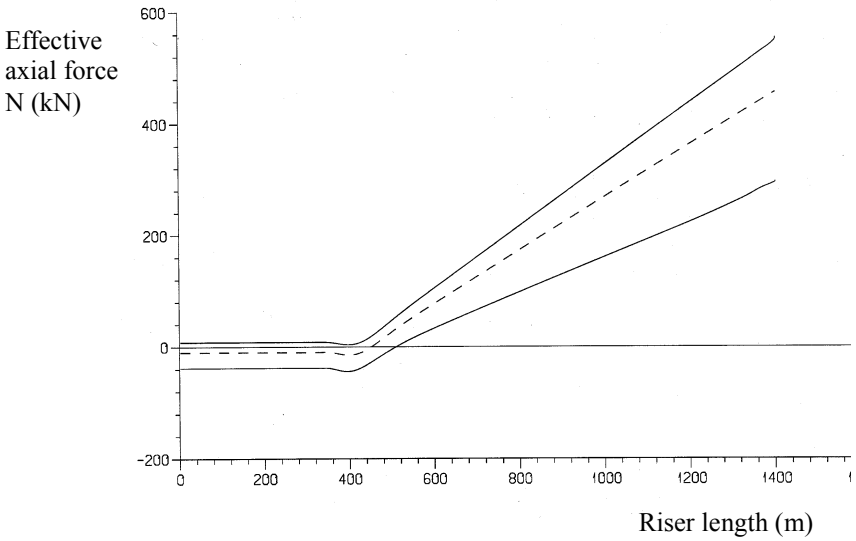

Figure 4.2a The effective axial force diagram for a riser with a specific gravity equal to specific gravity = 1.2.

The riser length in Figure 4.2 and the following figures (Figures 4.3-4.6) is measured along the riser from the interface coupling with a pipeline section.

As mentioned, a titanium riser with a specific gravity equal to 1.45 is defined as the base case for the present studies. Input data for this riser is specified in Table 4.1.

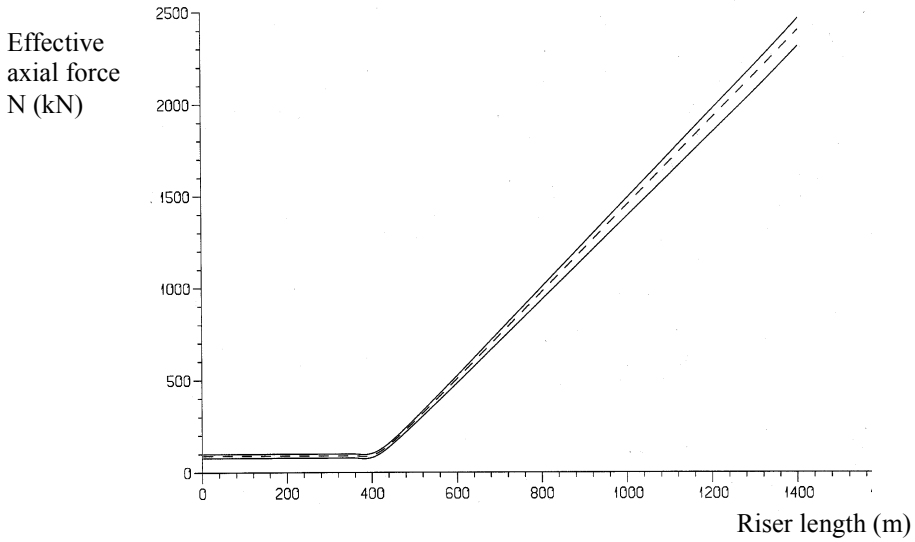

Figure 4.2b The effective axial force diagram for a riser with a specific gravity equal to specific gravity = 2.0.

Table 4.1. Key parameters for the base case.

D/t	External diameter	Internal diameter	Wall thick. t	Area, A	Moment of inertia, I	Water depth	Equiv. density, ρ_{eq}	Intern. content
	mm	mm	mm	mm^2	10^9 mm^4	m	kg/m^3	
26	548.6	508	20.3	33692	1.1772	1000	10430	empty

The D/t ratio represents the mean diameter over nominal wall thickness.

The diagrams for the effective axial force and bending moment along the whole riser for the base case are given in Figures 4.3 and 4.4, respectively. The environmental loading is 100 year current and 10 year wave height.

All values for the effective axial force along the riser are positive in Figure 4.3, except for the minimum values of zero in the touch-down area (distance around 400 m from bottom connection). The effective axial force at the top increases from 1058 kN (static value) to 1133 kN (+7%) due to dynamic motions. At the bottom the static and the maximum values are 23.1 kN and 36.6 kN (+58 %), respectively. The dynamic contribution to the axial force is greater at the top (75 kN) compared to the touch-down region (13.5 kN).

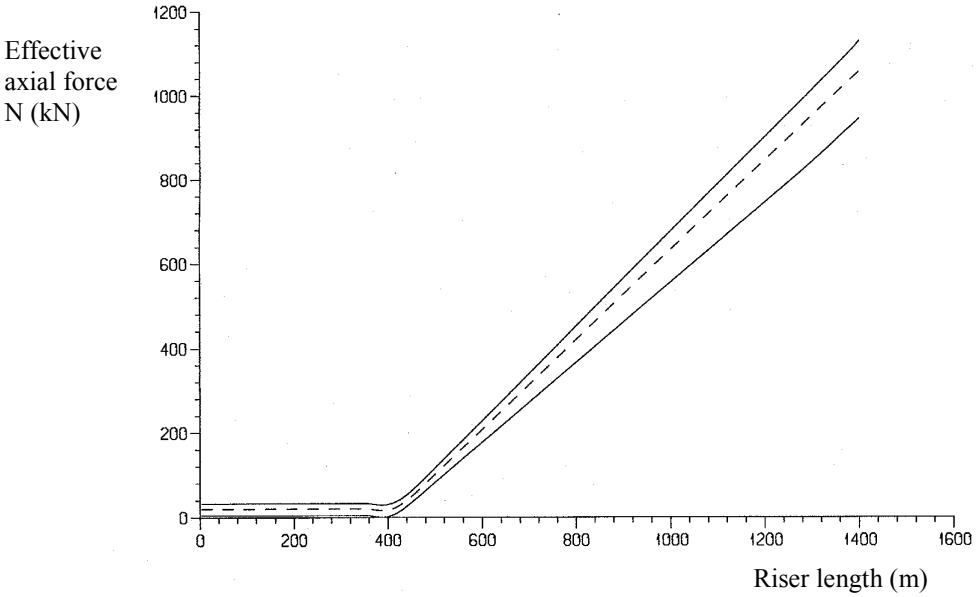

Figure 4.3 Effective axial force diagram for the whole riser. The continuous lines represents static + dynamic contributions, while the static values are given by the dotted line.

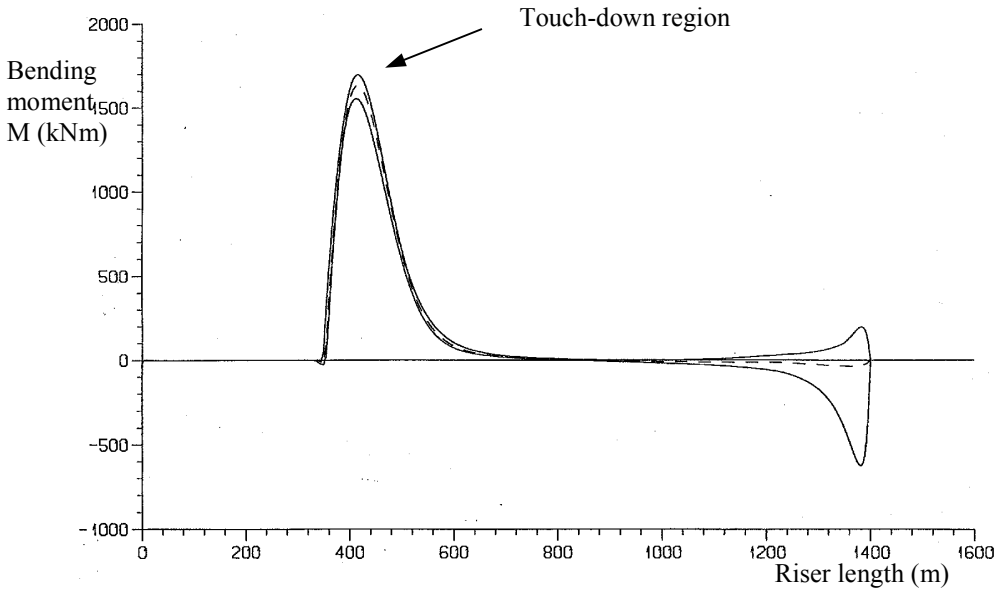

Figure 4.4 Bending moment diagram for the whole riser. The continuous lines represent the sum of static and dynamic response, while the static values are given by the dotted line.

Two different peaks appear for the bending moment along the riser. They represent the touch-down region and the connection to the floater. The bending moment caused by dynamic loading has a significant impact on the total bending moment in the wave zone. The bending moment is increased from 38 kNm (static value) to 593.5 kNm when taking the dynamic contributions into account for the upper part of the riser. The bending moment reaches its maximum at a distance about 420 m from the bottom connection. The maximum value is 1696 kNm. The local variation of the bending moment in the touch-down area is shown in Figure 4.5.

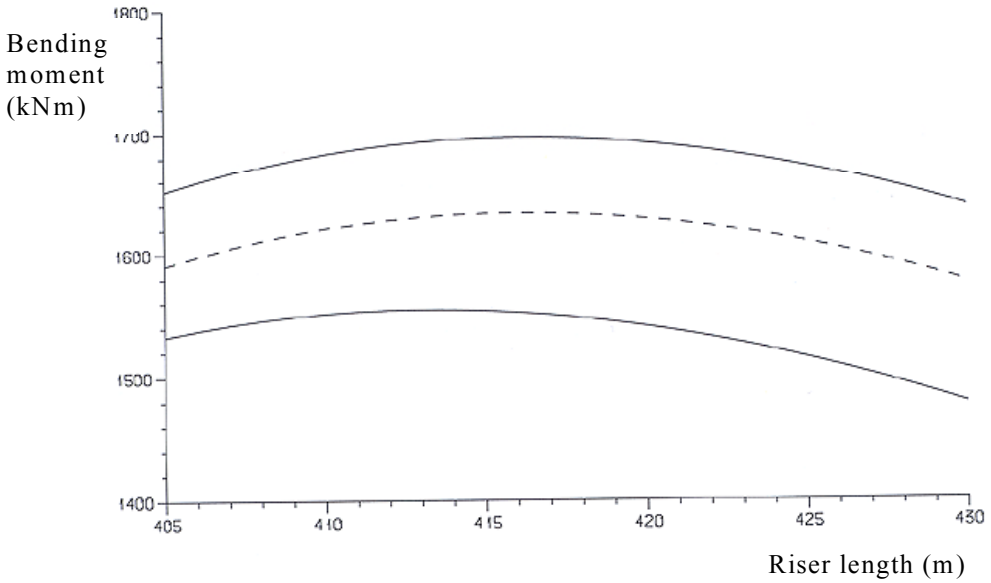

Figure 4.5 Local variation of the bending moment for the touch-down area. The continuous lines represent the sum of static and dynamic response, while the static values are given by the dotted line.

The dynamic contribution to the bending moment in Figure 4.5 is about + 4 %, i.e. from 1633 kNm (static value) to 1696 kNm.

Sea bottom modelling

The sea bottom modelling may or may not allow penetration of the riser into the soil. Comparing response values for maximum bending moment and corresponding true axial force in the sag-bend examines the adequacy of neglecting soil penetration. Table 4.2 gives the computed results. Hard and soft sea bed in the table are to be interpreted as very dense sand and very soft clay (for the latter option, the base case will penetrate about 0.5 diameter).

Table 4.2. Differences in relevant parameters for hard and soft soil modelling.

Load	Axial force, N_{true} (kN)	Bending moment, M (kNm)
Hard seabed	-2340.6	1633
Soft seabed	-2340.5	1632
Difference	- 0.004 %	- 0.06 %

These results indicate that the sea bed modelling is of no importance for the major response quantities of this study. The bottom stiffness used in the RIFLEX calculations for the present study is selected at an intermediate value to represent an intermediate properties of clay bottom material.

4.2.2 Load and Excitation Effects

In order to identify which parameters that will significantly influence the sag-bend response, an assessment of the contribution to the computed response from relevant input parameters is performed. Thermal expansion is neglected since the considered case is an export riser with relatively low temperature of the content. Furthermore, vortex induced vibrations are neglected.

Current induced load effects

Current is considered as a static loading. The effect of this loading is accounted for by introducing a distributed load along the riser according to a specified current profile with depth. Also the location of the maximum radius of curvature will differ compared to an analysis without current loading. Current profiles representing both a 10 year and a 100 year condition are given in Table 4.3.

Table 4.3. Current profile representing 10 year and 100 year condition.

Depth (m)	0	75	100	200	300	800	1000
10 year (m/s)	1.32	1.11	1.06	0.81	0.72	0.40	0.30
100 year (m/s)	1.45	1.27	1.20	0.89	0.85	0.45	0.35

Table 4.4. Comparison between relevant parameters with and without current loading for the sag-bend area.

Condition	Axial force, N_{true} (kN)	Bending moment, M (kNm)
Zero current velocity	-2304.4	1307
10 year current	-2332.2	1547
Difference	+1.2 %	+18.4 %
100 year current	-2340.6	1633
Difference	+1.6 %	+24.9 %

Inclusion of current loading increases the bending moment in the range between 18% and 25%. This is mostly caused by the decrease of the radius of curvature when the current forces are acting on the riser. However, it is also observed that the true axial force is decreased (i.e. higher compressive value), implying an increase in the effective axial force (tension is defined as positive). This aspect is explained by current acting on the riser in this direction that tends to move the riser in the same direction (similar to an increased static vessel offset position).

Wave load and wave/current effects

Waves may introduce relatively large heave motions of the floater. This can influence the true axial force and bending moment in the sag bend of the riser. The analyses are performed for a regular wave with wave height equal to 30.0 m and a corresponding period of 16.1 s. This represents a typical 100 year condition. The regular waves are combined with a 10 year current velocity (condition: 10 c & 100 w in Table 4.5). A condition with a 10 year wave height and a 100 year current velocity is called '100 c & 10 w' in the same table. The 10 year wave condition is specified by H = 26.6 m and T = 15.4 s.

Table 4.5. Effects of waves on the true axial force (N) and bending moment (M) for the sag-bend area.

Condition	Load	Axial force, N_{true} (kN)	Bending moment, M (kNm)
10 c & 100 w	Excl. waves	-2332.2	1547
	Incl. waves	-2319.6	1599
	Difference	-0.5 %	+3.4 %
100 c & 10 w	Excl. waves	-2340.6	1633
	Incl. waves	-2327.2	1696
	Difference	-0.6 %	+3.9 %

The maximum bending moment is increased by approximately 4 % when waves are present, and will be included in the further studies.

The effect of slow drift response of the vessel was examined for possible inclusion in the study. If the slow drift periods of the floater are relatively close to some of the eigen-periods of the riser, significant stresses may be introduced in the riser. The lowest eigen-period for the base case is 147 s, which is much lower than any representative slow drift periods of the TLP. Slow drift response is hence disregarded for the present study.

4.3 STUDY OF THE SAGBEND BENDING MOMENT CAPACITY BY COMBINING A GLOBAL AND A LOCAL NUMERICAL MODEL

The global riser analyses are based on beam elements and is thus not suitable for ultimate capacity calculations for pipe cross-sections. The computer program for the global analysis does not account for any non-linear behaviour of the material nor cross-sectional properties as initial imperfections, wall thickness variations or ovalization. A local finite element model using shell elements is employed as a numerical model to estimate the maximum bending capacity of the riser under combined loading in the sag bend area.

The local shell model replaces the global model in the area of the largest sag bend bending moments. Figure 4.5 showed a bending moment diagram over a length of 25 metres of the sag-bend region. Figure 4.6 shows the same diagram, but also the length for which the local model shall represent the global model. The maximum bending moment is very close to being symmetric for the indicated length of the local model. Hence, the point at which the maximum bending moment occurs is taken as a symmetry cross-section for the shell model. It is then possible to establish a local model as indicated in Figure 4.7.

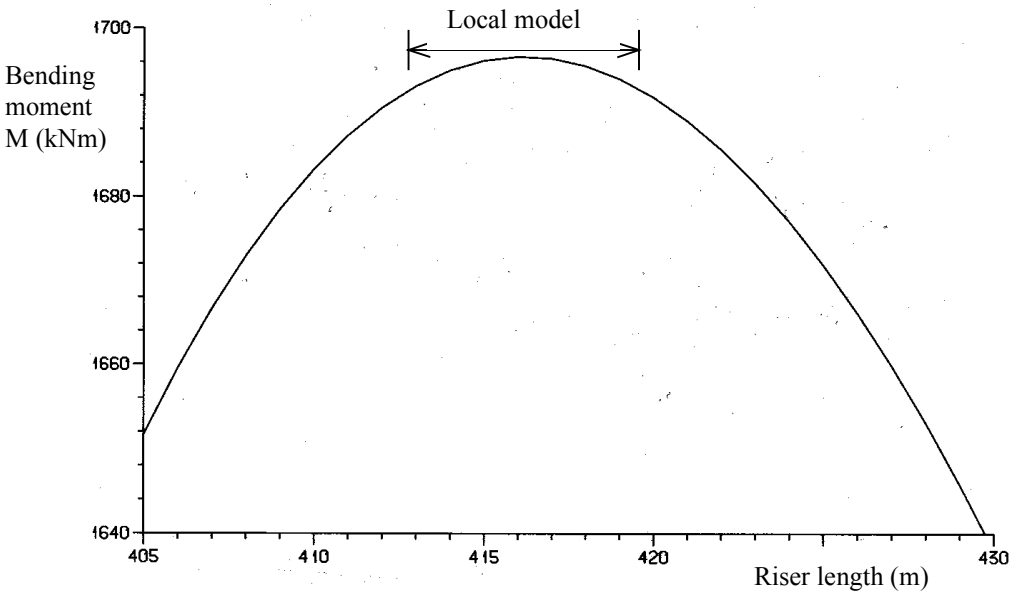

Figure 4.6 Bending moment diagram from the global analysis indicating the extension of the local model around the maximum value of the bending moment.

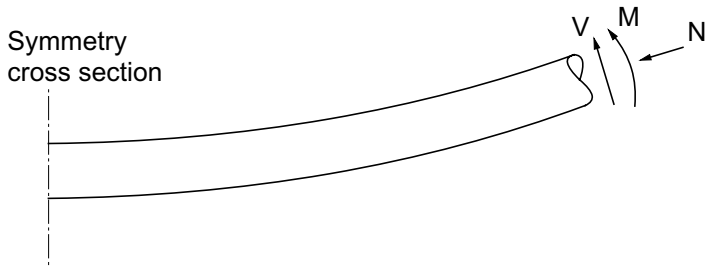

Figure 4.7 A principal view of the local model with the stress resultants from the global model applied at the end opposite to the symmetry cross section.

The stress resultants are applied at the end opposite to the symmetry cross-section of the model. The global analysis computer program gives the effective axial tension as output. Since the shell analyses replaces a part of the riser, the actual stresses and strains in the pipe wall of the global model are to be transferred to the local model. The effective axial force is thus transferred to true wall tension by the use of Equation (4.1), Sparks (1980).

$$T_E = T_{TW} - p_i \cdot A_i + p_e \cdot A_e \tag{4.1}$$

where

T_E : Effective tension.
T_{TW} : True wall tension.
p_i / p_e : Internal and external fluid pressure, respectively.
A_i / A_e : Internal and external cross-sectional area, respectively.

The loading path for the local shell model should be consistent with the global behaviour of the riser. Results obtained by analyses with combination of bending moment and external pressure are sensitive to the loading path, Karamanos and Tassoulas (1991). In the present study the riser is installed and subjected to external pressure, axial force, shear force and bending moment and assumed to be in the near position, see Figure 4.1. When the static vessel offset is increased, the bending moment will increase accordingly until its maximum capacity is reached. The external pressure remains constant, while the bending moment, the true axial force and the shear force will change. Furthermore, the position of the cross-section exposed to the largest bending moments will change locally as the magnitude of the curvature along the riser changes in the sag-bend area due the change in vessel position. The true axial force and the shear force will also change with the change in curvature. The local modelling accounts for these effects by identifying the current location of maximum bending moment and the corresponding values of the axial force and the shear force. This means that the symmetric cross-section in the local model (see Figure 4.7) represents the cross-section with maximum curvatures for current offset positions. Figure 4.8 shows the stress resultants as a function of the static vessel offset. The values in this figure are normalised with the corresponding values for the vessel in the near position.

As can be seen from Figure 4.8, the increase in the normalised quantities are linear for the present range of static vessel offset for all parameters (the range is from mean (0 %) to near (10 %) position). The shear force (V) and the bending moment (M) increase to 1.96 and 1.47 times the values for zero offset, respectively. The true axial force (N) is almost constant. It increases only 1.023 times the value for the vessel in the near position.

When applying the stress resultants from the global model to the local model, the axial force is kept constant. This is chosen due to the fact that maximum bending moment is not influenced by the small increase in the true axial force of + 2 % compared to the first order increase in bending moment (increased by + 47 %).

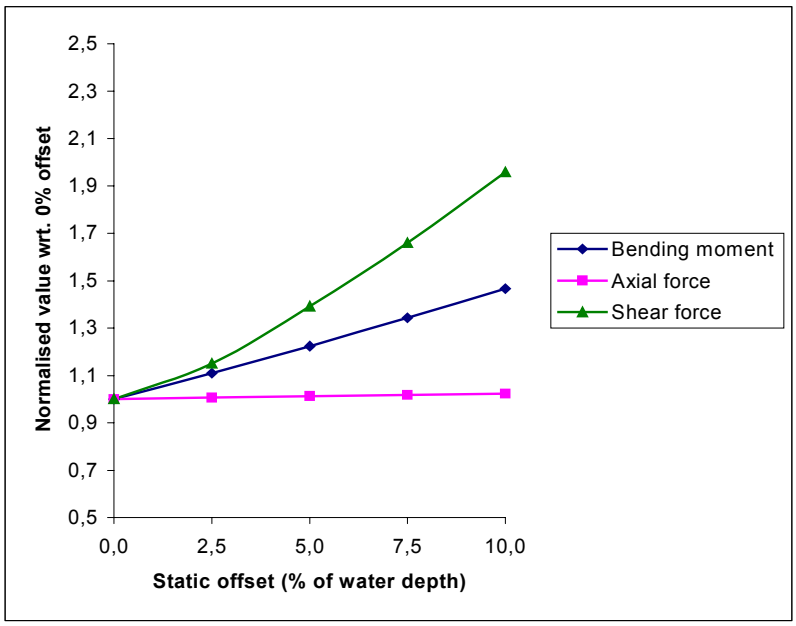

Figure 4.8 Normalised values of axial force, shear force and bending moment as a function of the vessel offset.

The shear force and the bending moment are increased in the same relative magnitude as indicated in Figure 4.8, implying that the actual bending moment gradient from global riser analysis remains and the equilibrium is maintained.

4.4 THE LOCAL ANALYSIS MODEL

The finite element computer program ABAQUS (1996) is used to simulate the nonlinear behaviour of the titanium riser in the area of maximum bending moment in the sag bend region.

The sketch of the local model in Figure 4.9 is used to discuss the applied boundary conditions. Symmetry is assumed with the vertical plane as the principal bending plane (the plane through boundaries C and D in Figure 4.9). This is experimentally verified in, e.g. Mohareb et al. (1993), Reddy (1979), Sherman (1976), Bouwkamp & Stephen (1973) and Jirsa et al. (1972). Furthermore the local deformations are assumed to be symmetric about the cross-section of maximum curvature (boundary A in Figure 4.9).

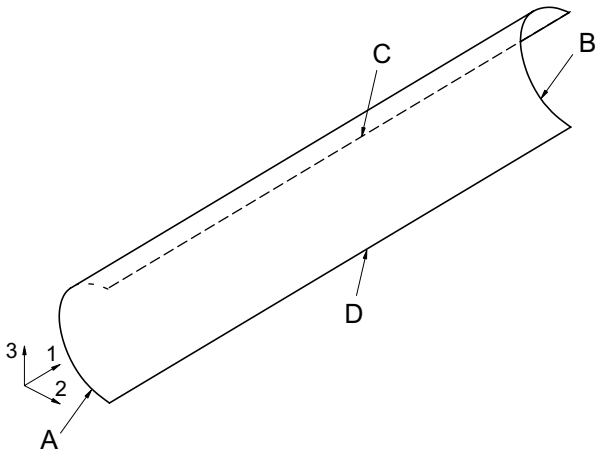

Figure 4.9 A schematic view of the local model used for the numerical simulations.

The boundary conditions for the model in Figure 4.9 are as follows:

The nodes at boundaries C and D can only move in the vertical bending plane and shall have symmetric motion with respect to that plane (normal displacement is fixed and rotations about the longitudinal and the vertical axes are fixed). The nodes at boundary A can not move in longitudinal direction and are allowed to rotate only around the longitudinal axis. Only the node midway between boundaries C and D on boundary A is fixed against vertical motion.

The stress resultants from the global model are applied at cross-section B in Figure 4.9. This cross-section must not deform during the analysis in order to maintain proportionality between bending and corresponding applied normal stresses at the cross-section. The present model obtains this by increasing the thickness adjacent to this cross-section. The stress distribution is in accordance with technical beam theory (Navier-Bernoulli's hypothesis).

The maximum bending moment capacity in the sag bend area as estimated from the local finite element model is illustrated by the load-displacement curve in Figure 4.10. After the maximum point, the cross-sectional capacity decreases due to increased ovalization that is not compensated by material hardening. The nodal displacement as a function of the load in Figure 4.10 is drawn for the uppermost node on the compressive side at cross-section A in Figure 4.9 (i.e. on the intersection between A and C).

The nonlinear analyses that provide the estimates of the maximum bending moment capacity include equilibrium iterations after each load increment. Since a limit point is also involved to define the maximum bending moment capacity, an arc-length method (modified RIKS method) is applied as discussed in Chapter 2.

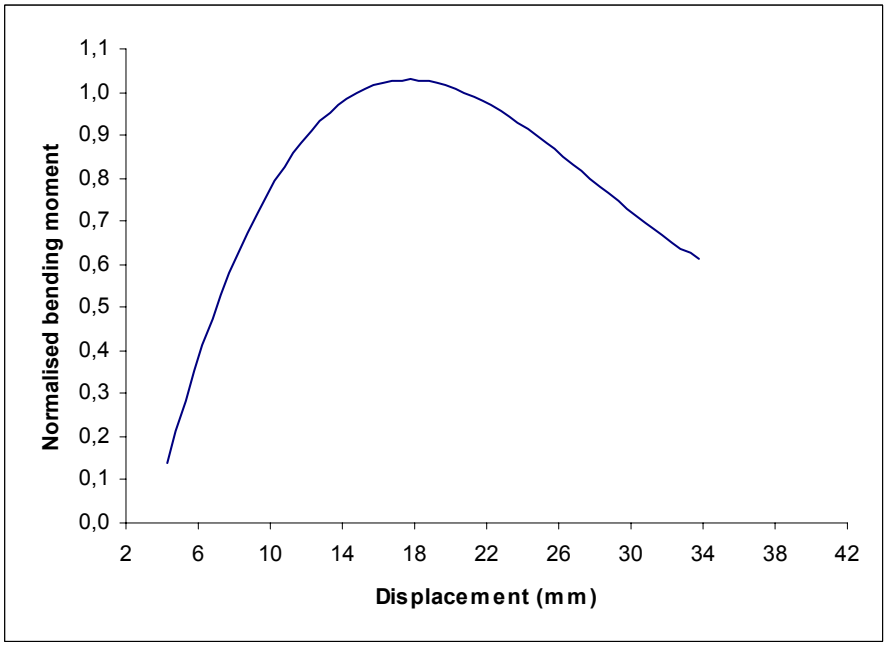

Figure 4.10 Load-displacement curve for a collapse analysis. 'Load' on the vertical axis is to be interpreted as non-dimensional bending moment.

All local analyses are based on a certain initial ovality. The initial ovality is introduced by applying a force at the top and the bottom node in the symmetric cross-section (see cross-section A in Figure 4.9). A new computational step is then restarted, where ABAQUS allows the pipe to be stress-free at the start of further computational steps.

The length of the finite element model must satisfy the requirement that the increased thickness at end B is not transferring boundary disturbance to end A (the symmetry cross-section of maximum bending moment). The development of deformations at the symmetry cross-section shall be as for the continuous riser. The boundary disturbance effects are checked by analyses for four different model lengths corresponding to the length/diameter-ratios as given together with the results in Table 4.6.

Table 4.6. Results for variations in the model length with respect to the diameter.

Length over diameter ratio (L/D)	Total number of elements	Normalised max. von-Mises stress	Normalised max. longitudinal strain	Normalised max. bending moment
3	264	1.02	1.36	1.04
4	348	1.00	1.10	1.01
5	432	1.00	1.00	1.00
6	516	1.00	1.00	1.00

Normalised is to be interpreted as the current value divided by the value for L/D=5.

It is seen that for a model length equal to 5 times the diameter, there are negligible effects on the maximum bending moment capacity. However, it is emphasised that the maximum longitudinal strain is somewhat sensitive to the size of the load step close to reaching the maximum bending moment capacity. This is due to the very low strain hardening that applies for this particular titanium grade. A small change in the applied load may introduce a relatively large change in the strain level. This is illustrated by Figure 4.11, where the load-displacement curves for the four actual L/D-ratios are given. In this figure it is clearly seen that for a given load level, the displacement, and implicitly the strains, may vary significantly. This supports the relatively large difference in longitudinal strain in Table 4.6 between the case with L/D equal to 3 and the others. Additionally, it can also be observed from the curves, that the two longest models have load-displacement curves matching each other also in the post-buckling region. This does not apply for an L/D-ratio equal to 4.

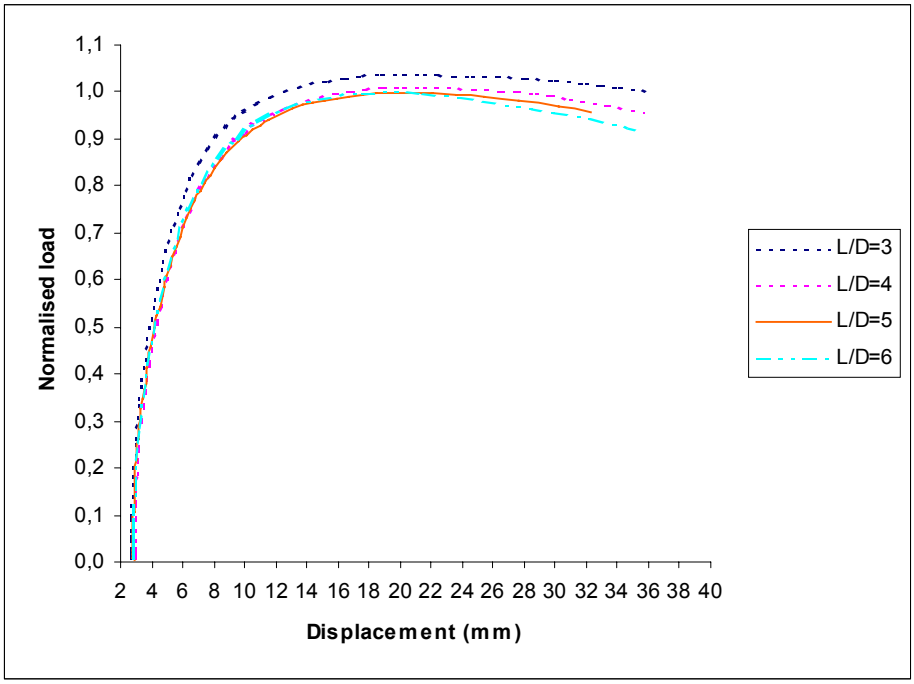

Figure 4.11 Load-displacement curves for various length/diameter-ratios

A general-purpose four-node quadrilateral shell element with bilinear interpolation is used in the finite element model. The element is based on shear flexible (Mindlin, e.g. Cook et al (1989)) shell theory. Fully reduced integration is used to prevent shear locking. Furthermore, Koiter-Sanders shell theory, Budiansky and Sanders (1963), is used to calculate bending strains. Thickness changes as a function of in-plane deformations are allowed in this element's formulation.

Requirement on element size is investigated by analysing the problem with 8, 12 and 16 elements in the hoop direction and by employing square elements for a selected part of the pipe adjacent to the symmetry cross-section. The results are given in Table 4.7.

Table 4.7. Stress and strain results for variations in the element mesh.

No of elements in ring direction	Element size (mm x mm)	Total number of elements	Normalised maximum von-Mises stress	Normalised max. longitudinal strain	Normalised max. bending moment
8	100 x 100	200	1.01	1.08	1.02
12	70 x 70	432	1.00	1.00	1.00
16	50 x 50	800	1.00	1.00	1.00

The maximum bending moment is not considerably influenced by the variation in the element mesh indicated in Table 4.7. However, there are still some deviations by using 8 elements in hoop direction compared to 12 and 16 elements (8 % in the compressive longitudinal strain and 2 % in the maximum bending moment capacity). Hence, by using 12 elements in the hoop direction, sufficient accuracy is achieved. Figure 4.12 shows the nodal displacement for the uppermost node on the compressive side of the symmetry cross-section (i.e. the intersection between A and C in Figure 4.9) as a function of the normalised load level (i.e. normalised bending moment with respect to the value for 12 and 16 elements). The three curves represent a finite element model with 200 elements (8 elements in hoop direction), 432 elements (12 elements in hoop direction) and 800 elements (16 elements in hoop direction), respectively. It is seen that for a given load level, the displacement for the coarse model is smaller than for the finer models. Accordingly, the coarse model estimates higher bending moment capacity (i.e. the top of the corresponding curve in Figure 4.12) and at higher strains. Implicitly, the strains for the fine model are smaller than for the coarse mesh. From Figure 4.12 it is clearly seen that the two curves for 12 and 16 elements in hoop direction converge to the same value for the maximum bending moment. For 12 elements in hoop direction, calculation is also performed for 8-node shell elements. No differences are observed for the maximum bending moment capacity.

The number of integration points over the wall thickness is also investigated. The results are given in Table 4.8.

Table 4.8. Different number of integration points over the wall thickness.

Number of integration points over the thickness	Normalised max. von-Mises stress	Normalised max. longitudinal strain	Normalised max. bending moment
3	0.99	0.86	0.97
5	1.00	1.00	1.00
7	1.00	1.01	1.00

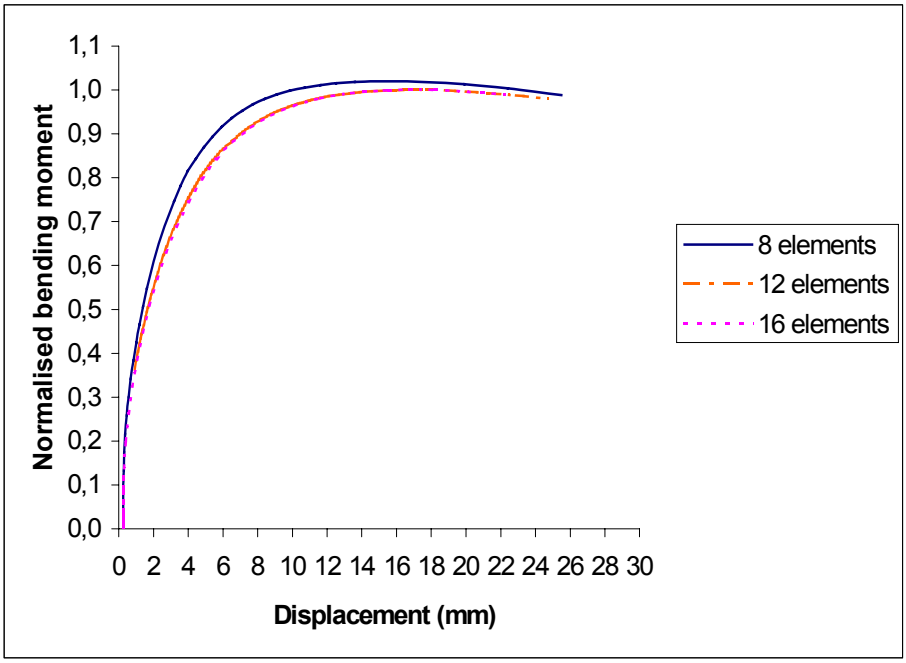

Figure 4.12 Load-displacement curves for various element meshes.

The number of integration points influences the results. A deviation of about 3 % in the maximum bending moment capacity is observed by increasing the number of integration points from 3 to 5 and 7. The difference is less for the maximum von-Mises stress (1 %), but greater for the maximum longitudinal strains (- 14 % & + 1). The load-displacement curves for the three cases in Table 4.8 are given in Figure 4.13. It is clearly seen that by using 3 integration points over the thickness, inaccurate results are obtained for the maximum point of the load-displacement curve. On the other hand, Figure 4.13 indicates also that almost nothing is gained by increasing the number of integration points from 5 to 7. The explanation for the lower maximum bending moment capacity when using 3 integration points is that the model can not describe the strain variation over the wall thickness sufficiently accurate. By having a larger number of integration points over the thickness, the cross-section will reach a plastic strain level successively for various integration points over the thickness as a function of the applied load. This is not the case for the cross-section using the lowest number of integration points. This aspect also explains the relatively rapid drop in the curve for post-collapse behaviour for 3 integration points.

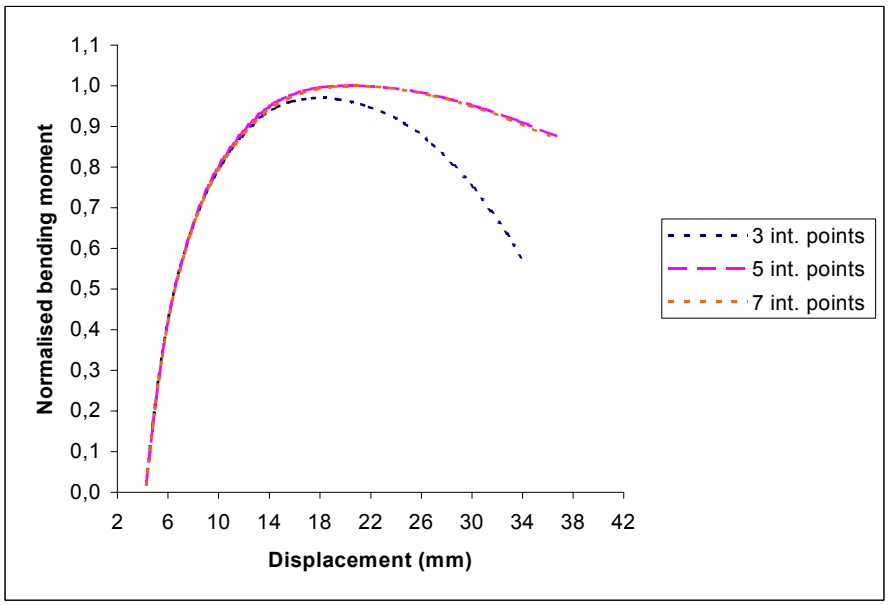

Figure 4.13 Load-displacement curves for different number of integration points over the thickness (analyses are terminated manually).

Furthermore, possible optimisation of the element mesh is sought by varying the number of elements in longitudinal direction. Square elements are used where the largest cross-sectional deformations occur (a length of one diameter from the symmetric cross-section) and linearly increasing element lengths towards the other end of the model. The 'length over width'-ratio for the longest elements (i.e. at the cross-section B in Figure 4.9) is set equal to 3, implying a total number of elements equal to slightly above 250 (this reduces the total number of elements to 58 % compared to a purely square mesh). The results for the alternative and the square model are given in Table 4.9, and indicate that differences between the two meshes are negligible (mesh type 'Bias' represents the most efficient mesh).

Neither the maximum von-Mises stress nor the bending moment capacity is affected by this optimisation of the model. A deviation of about 1 % in the maximum longitudinal strain is observed. However, the updated and more efficient mesh is found to represent the behaviour well enough for the numerical simulations and is used in the present study.

Table 4.9. Analyses for mesh with different 'length over width'- ratio of the elements.

Mesh type	Total number of elements	Normalised maximum stress	Normalised max. longitudinal strain	Normalised max. bending moment
Square	432	1.00	0.99	1.00
Bias	252	1.00	1.00	1.00

The finite element mesh used in the numerical shell analyses is then as shown in Figure 4.14.

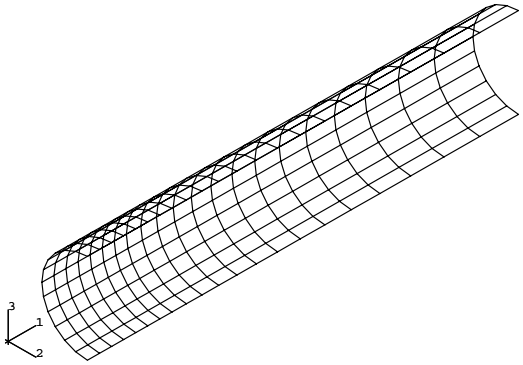

Figure 4.14 Finite element mesh used for numerical simulations.

4.5 MATERIAL MODELING FOR STRUCTURAL ANALYSIS

The requirements of the material model to be applied in the finite element analysis, are the following:

The material model shall give an accurate representation of the stress-strain relationship. The hardening characteristics are obviously of major importance when it comes to localisation of the deformation in connection with buckling and collapse analysis, Zhou and Murray (1993a, 1993b, 1995). An accurate modelling of the real plastic material behaviour is hence important to obtain reliable results when yielding takes place and a possible local buckle is being initiated. The stress-strain relationship in the present analysis, is represented by a material model which is fitted to about 45 measured points for each test. Implementation is discussed later in this section.

The material model shall be able to model isotropic elasto-plastic behaviour included hardening. The Bauschinger effect, Chen and Han (1987), must be modelled if reversed yielding can take place. However, such yielding does not occur when identifying the maximum bending moment capacities in the present study. This is because the most relevant part of the load-displacement curve for the present analyses is up to the maximum bending moment capacity, and not in the post-buckling region (see Figure 4.10).

When trying to identify the material model representing the laboratory data in an optimal way, several material models were tried, i.e. Ramberg-Osgood (1943), Tvergaard & Needleman (1980) and Voce (1948) (the latter is also formulated in alternative ways in e.g. Lemaitre & Chaboche (1990) and Khan & Huang (1995)). The three formulations are given as follows:

Ramberg-Osgood:

$$\sigma = \sigma_0 + K \cdot \varepsilon_P^{1/M} \tag{4.2}$$

where σ_0, K and M are the parameters that may be varied, while ε_P is the true plastic strain (i.e. $\varepsilon_P = \varepsilon_{TOT} - \sigma / E$).

Tvergaard and Needleman:

$$\varepsilon = \frac{\sigma_Y}{E}\left[\frac{1}{n}\left(\frac{\sigma}{\sigma_Y}\right)^n - \frac{1}{n} + 1\right] \tag{4.3}$$

This formula is valid for $\sigma > \sigma_Y$. In principle, both σ_Y and n may be varied.

Voce:

$$\sigma = \sigma_{EL} + R_1 \cdot \left(1 - \exp(-C_1 \cdot \varepsilon_P)\right) + R_2 \cdot \left(1 - \exp(-C_2 \cdot \varepsilon_P)\right) \tag{4.4}$$

where σ_{EL} is the elastic limit stress (i.e. the stress at which plastic strains occur). R_1, R_2, C_1 and C_2 are the material parameters to be determined from material tests.

All three material models are compared to the stress-strain relationship from the laboratory data (see Figures 4.15 and 4.16). Figure 4.16 shows an expanded comparison of the models and data below a plastic strain level of 0.01. Figure 4.15 gives results for strain levels up to 0.05. ‘Mean curve’ is to be interpreted as the average of all stress-strain relationships from the laboratory tests.

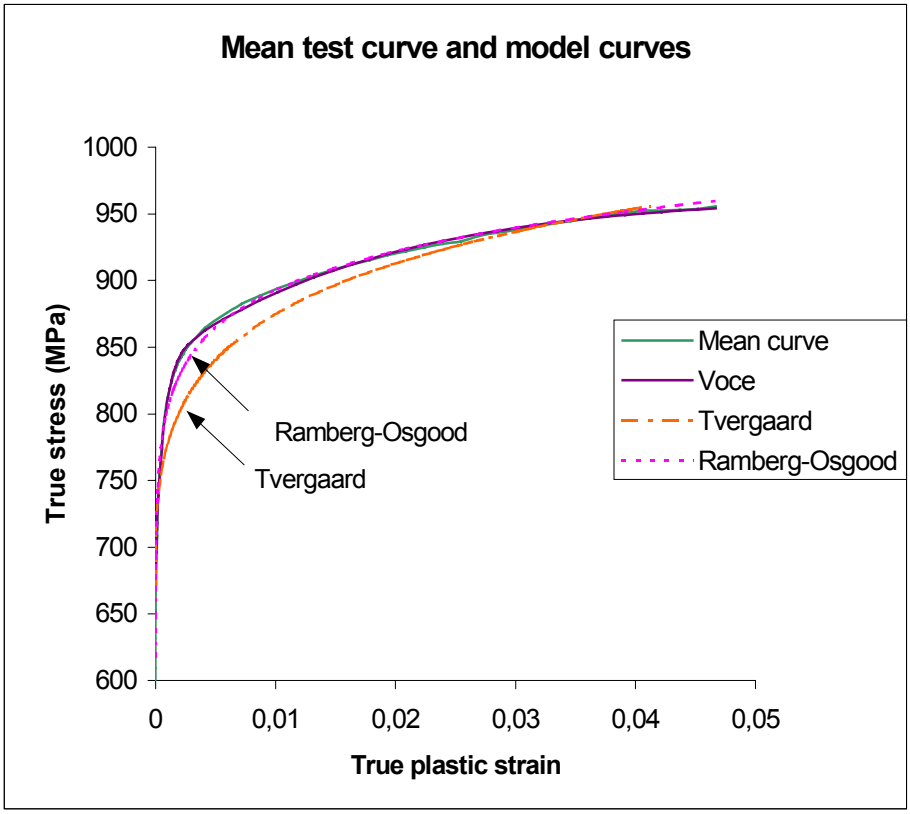

Figure 4.15 Different material models compared to laboratory data.

It is clearly seen that the Tvergaard-Needleman model does not give a close representation of the real material behaviour. Furthermore, it seems like the Ramberg-Osgood model does not match the mean curve as well as the Voce model. This is seen clearly if the curves are plotted for true plastic strain in the range up to 1 % (Figure 4.16).

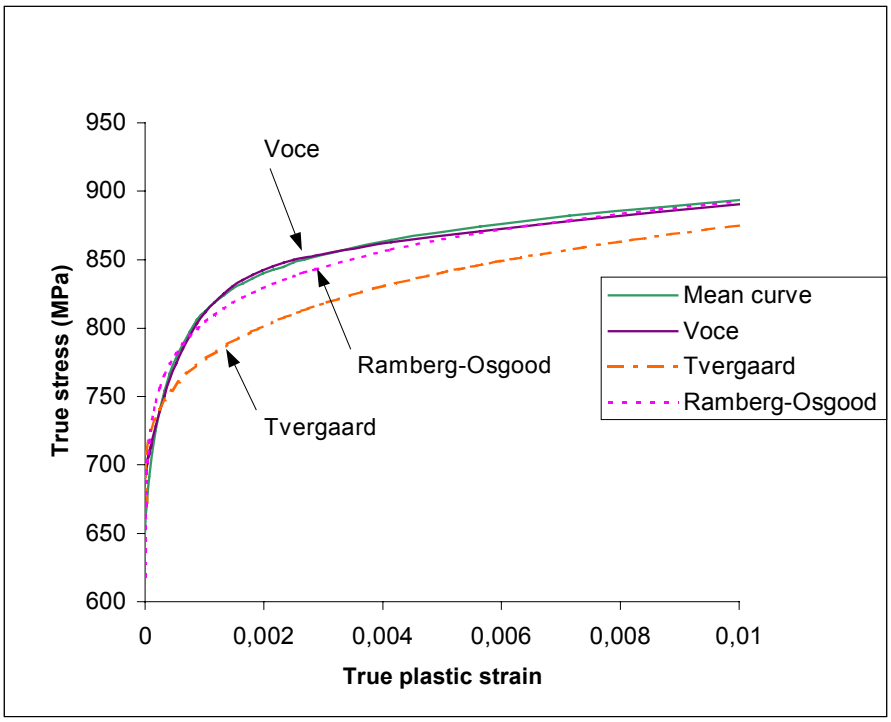

Figure 4.16 Fit of material models in the range of plastic strain up to 1 %.

The material model suggested by Voce is adopted in the material modelling of the actual titanium alloy.

4.6 VERIFICATION OF THE FINITE ELEMENT MODEL

Results from the simulations are checked against analytical solutions and experimental results to verify the finite element model.

For the case of uniformly distributed external pressure, theoretical solutions are available for rings. In the elastic range Timoshencko and Gere (1961) give the following formula:

$$p_{el} = \frac{2 \cdot E}{1 - \upsilon^2} \cdot \left(\frac{t}{D}\right)^3 \tag{4.5}$$

The transition zone between elastic and plastic collapse is found for a D/t-ratio when the hoop stress reaches the yield or proportionality limit:

$$p_Y = 2 \cdot \sigma_Y \cdot \left(\frac{t}{D}\right) \tag{4.6}$$

where E, ν, σ_Y, D and t are Young's modulus, Poisson's ratio, yield stress, mean diameter and the wall thickness.

The transition point is defined when Equations (4.5) and (4.6) are equal. For titanium grade 24 (mean values in Chapter 3), this specific point is calculated to be

$$D/t = \sqrt{\frac{E}{\sigma_Y \cdot (1-\nu^2)}} = 12.4 \tag{4.7}$$

Calculations are performed to verify that the FE-model estimates the limit for application of Equation (4.5). For these calculations a completely uniform element mesh is used (all element rings equal along the tube).

Figure 4.15 gives as a function of D/t-ratios the pressure value from Equation (4.5) with a bold line and the pressure limit for which the hoop stress reaches the proportionality or yield limit. As can be seen from Figure 4.15, the intersection between the two curves is for a D/t-ratio equal to 12.4. The finite element model is obviously able to predict collapse pressures on both sides of the transition point (given by the diamond called P_y).

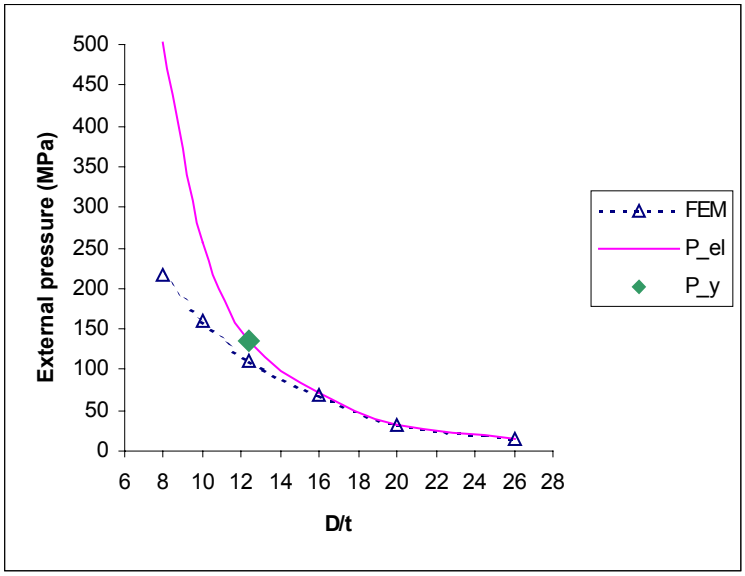

Figure 4.15 Comparison between external collapse pressure based on FEM-results and elastic collapse pressure given in Equation (4.5).

The computed collapse pressure values are represented by the triangles (called FEM) in Figure 4.15. The values from the finite element model calculations are very close to the elastic solution according to Equation (4.5) for D/t-ratios greater than 16. The D/t-ratios of the further calculations in this work vary between 20 and 30. The FE-predicted collapse pressures are represented by a smooth curve, also for D/t-ratios less than the transition point. The reason for the deviation between the 'FEM'-curve and the 'P_el'-curve for D/t-ratios less than 16, is that the formula for 'P_el' identifies the elastic collapse pressure. This specific formula is not valid if plasticity occurs. The elastic collapse pressure formula over-predicts the collapse pressure based on the FE-analysis for D/t-ratios less than 16. This is as expected since the elastic pressure in Equation (4.5) is proportional to the Young's modulus. However, when yielding occurs the stress-strain gradient decrease. This implies larger deviation between the 'P_el'-curve and the 'FEM'-curve for smaller D/t-ratios, as also shown in Figure 4.15.

Comparison with laboratory tests

Comparisons are also made with laboratory tests of titanium grade 29 (Ti-6Al-4V-Ru). Test results for titanium grade 29 (Ti-6Al-4V-Ru) were made available during the final stage of the present research work, Schutz (1999) and Spolton (1999). The tests apply external pressure and then bending moment to reach the maximum bending capacity. These laboratory tests are simulated with the finite element model as given in Figure 4.14. The comparisons between the maximum bending moment capacity from the tests and the estimates by the finite element model are given as the ratio M_{FEM} / M_{LAB} in Table 4.10. It should be noted that $p_{c,DnV96}$ in Table 4.10 is to be interpreted as the critical external pressure given in DnV (1996) by:

$$\left(p_c - p_{el}\right)\left(p_c^2 - p_p^2\right) = p_c\, p_{el}\, p_p\, f_0\, \frac{D}{t}$$

where

$p_{el} = 2\ E\ (t/D)^3 / (1-\nu^2)$

$p_p = 2\ SMYS\ t/D$ (SMYS: Specified Minimum Yield Stress)

$f_0 = (D_{max}-D_{min}) / D > 0.005 = 0.5\ \%$

Results from the finite element analyses are given in Table 4.10. They are based on wall thickness measured in the laboratory. Furthermore, an initial ovality equal to 0.5 % (common minimum requirement based on DnV (1996)) is assumed. This is, however, not explicitly measured, but is reasonable from a certain observed wall thickness variation in hoop direction of all tested pipes.

Table 4.10: Comparisons between finite element analyses and laboratory tests.

Test no	1	2	3	4	5	6
D/t	19.4	19.8	19.9	27.2	27.2	11.4
p_e / $p_{c,DnV96}$	.65	.59	.55	.37	.34	.2
M_{FEM}/M_{LAB}	1.00	0.99	1.02	0.98	1.06	1.00

The finite element results comply generally very well with the laboratory tests. It is to be noted that Tests 2 and 6 did not reach maximum bending moment in the laboratory. However, it is believed that the values are close to the corresponding maximum capacities. In general the numerical simulations over-predict the values from the laboratory tests. This is also as expected, since the numerical model should be on the stiffer side. However, test 4 is reported to have a maximum bending moment capacity greater than obtained from the FE-analysis. When looking at the data for this specific pipe, it is noticed that its maximum wall thickness is 4.5 % above the average wall thickness. The orientation of the pipe is not monitored. Thus, if the pipe is oriented with the thickest part of the wall on the compression side of the bending plane, this may explain the difference. Tests 1 to 3 have a decreasing external ($p_e/p_{c,DnV96}$)-ratio and correspond to the lower part of the D/t-range relevant for the numerical calculations in Chapters 5 and 6. The maximum bending moment is over-predicted up to 2 % by the finite element model compared with the data from Tests 1, 2 and 3. Tests 4 and 5 represent bending dominated conditions, for which the D/t-ratio is very close to the base case for this study. The FE-model over-predicts the maximum bending moment capacity up to 6 % for this specific D/t-ratio. Test 6 is performed for a D/t-ratio somewhat outside the range for the present study, but the finite element model seems to be applicable also for this D/t-value.

C h a p t e r 5

RELIABILITY ANALYSIS OF ESTIMATED MAXIMUM BENDING MOMENT CAPACITY

"As far as the laws of mathematics refer to reality, they are not certain; and as far as they are certain, they do not refer to reality."
Albert Einstein (1879-1955)

5.1 INTRODUCTION

The maximum bending moment capacity of a deep water titanium riser depends on different parameters as identified in the previous chapters. All these parameters are associated with some uncertainty, and introduce an uncertainty in the estimated maximum bending moment capacity. The inherent variations may be divided into geometrical and material variations. The former is due to the manufacturing process of titanium pipes implying variations in the wall thickness and circular shape of the cross-section. The latter is introduced by uncertainties in alloy composition leading to variations in mechanical properties.

Regarding all these uncertainty aspects, it is of interest to identify the parameters whose contribution to the total probability of failure (also referred to as limit state exceedance), are the greatest. The greater the contribution to the limit state exceedance, the greater is the need and interest to reduce the uncertainty in the particular parameter.

By performing reliability analyses of the estimated maximum bending moment capacity, each parameter's contribution is identified. The reliability analyses are based on the methods for prediction of maximum bending moment capacity as described in Chapter 4. Variations of each of the uncertain parameters imply variation of the maximum bending moment capacity. When looking at one parameter at a time, this variation may be represented by an analytical expression as a function of the parameter under consideration. It is possible to establish an analytical function for each of the input parameters. By combining all functions, a response surface for the predicted maximum bending moment capacity is obtained. The reliability analyses employ the response surface when calculating the probability of exceedance of the predicted maximum bending moment capacity.

5.2 BASIC PRINCIPLES OF PROBABILISTIC ANALYSIS

The probability of failure for a specific structure subjected to loads is a key problem in structural reliability analysis. For a particular structure there exists a limit value of the load it can withstand before failure occurs. The probability of failure herein refers to exceedance of a limit state. Mathematically, the probability of failure, p_f, can be written as, Madsen et al. (1996), Melchers (1987):

$$p_f = P (R \leq S) = P (R-S \leq 0) \tag{5.1}$$

The relevant load action is usually denoted by the capital letter S, and the implied response or load effect by a capital R. Furthermore, this function can be expressed as

$$p_f = P [g(R,S) \leq 0] \tag{5.2}$$

where $g(\cdot)$ is to be interpreted as the limit state function or the failure function.

In a general way this specific $g(\cdot)$-function may consist of n-variables (X_1, X_2, …, X_n) and the failure criterion is typically expressed as:

$$g(\mathbf{X}) = g(X_1, X_2, \ldots, X_n) = 0 \tag{5.3a}$$

where the functions R and S can generally be written as

$$R(\mathbf{X}) = R(X_1, X_2, \ldots, X_k) = 0 \tag{5.3b}$$

$$S(\mathbf{X}) = S(X_{k+1}, X_{k+2}, \ldots, X_n) = 0 \tag{5.3c}$$

Failure occurs when $g(\mathbf{X}) < 0$. On the other hand, positive values of this specific g-function indicate the safe domain. The set of X-values giving $g(\mathbf{X})$ a zero value defines the limit surface.

The probability of exceeding the limit can, however, also be expressed by the joint probability density function, $f_{\mathbf{X}}(\mathbf{x})$, for all time-independent variables in **X** over the failure domain:

$$p_f = P[g(\mathbf{X}) \le 0] = \int_{g(\mathbf{X})\le 0} f_{\mathbf{X}}(\mathbf{x}) d\mathbf{x} \tag{5.4}$$

In general this specific integration is of a complex nature, and is normally solved by numerical integration.

Usually, some of the basic random variables in equation (5.3) are non-Gaussian. A favourable property is obtained by transforming the set of input variables, which initially is referred to as the **X**-space, into an uncorrelated and normally distributed **U**-space. This means that the limit surface in the **X**-space is mapped onto a corresponding limit surface in the **U**-space.

The favourable property is that the probability of exceeding the limit can now be approximated by identifying the minimum distance from the origin (where the probability density in the **U**-space is largest) in the **U**-space to the limit surface. This distance is called the reliability index and the corresponding point on the limit surface is referred to as the design point, β (see Figure 5.1).

To establish the probability of failure, two typical types of solution procedures are frequently employed: simulation or analytical algorithms. Monte Carlo-simulation, among others, is a method to determine the probability of failure corresponding to the former type of analysis. The latter type consists typically of FORM and SORM (1st and 2nd order reliability methods, respectively). The approximations to the failure surface are indicated in Figure 5.1.

Monte-Carlo simulations, Rubinstein (1981), generate a relatively high number of independent realisations of the structural response. The probability of failure is estimated as number of simulations that exceed the failure surface divided by the total number of realisations. See figure 5.2.

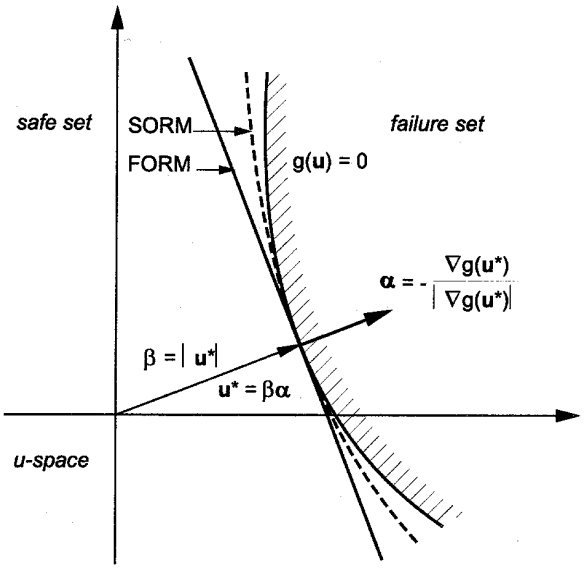

*Figure 5.1 A definition of the reliability index in the **U**-space.*

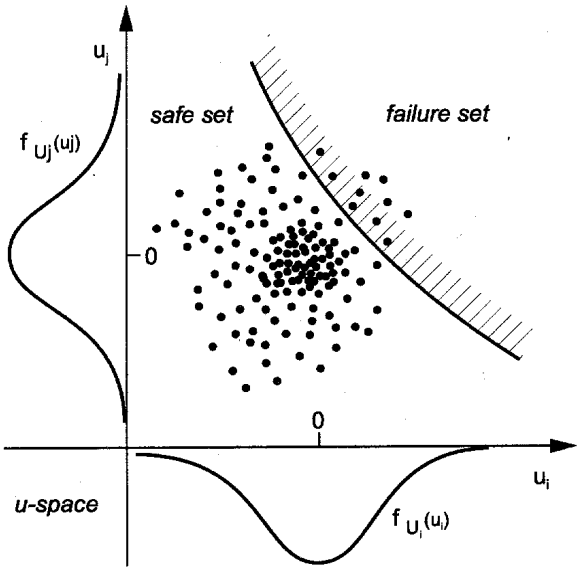

Figure 5.2 Visualisation of results from Monte-Carlo simulations.

The FORM approximation corresponds to a linearization of the failure surface at the design point, Rackwitz & Fiessler (1978). A better approximation can be obtained by using a second-order approximation to the failure surface, which is referred to as SORM, Breitung (1984). Both these methods are frequently employed (see Figure 5.1).

When it comes to probabilistic capacity analysis, a representative failure function needs to be established. This function, g(**X**), may be expressed as:

$$g(\mathbf{X}) = h(\mathbf{X}) - C \tag{5.5}$$

where

- h(**X**) : maximum capacity as a function of the parameters contained in the vector **X**, which is the response surface value.
- C : specified threshold level for which the probability of exceedance is wanted.

The set of input parameters to the response problem is modelled as random variables since they have inherent, significant uncertainties. The statistical representation is based on results from the laboratory tests.

Failure to exceed the threshold C is now defined by $g(\mathbf{X}) < 0$. The probability of exceeding the limit is denoted probability of failure, p_f, indicating failure to meet the requirement implied by the given limit C. This also corresponds to the cumulative probability distribution function ($p_f = P(M_{max} < C) = F_{Mmax}(C)$) for the response at the specified limit.

The probability of failure is expressed by

$$p_f = P[g(\mathbf{X}) \le 0] = \int_{\Omega} f_{\mathbf{X}}(\mathbf{x}) d\mathbf{x} \tag{5.6}$$

The function, $f_{\mathbf{X}}(\mathbf{x})$, is the joint probability density function of the uncertain parameters. The integration is performed over the domain Ω given by requiring $g(\mathbf{X})=0$. Calculations are performed by means of the computer program PROBAN (1996).

The cumulative distribution function of the response quantity (maximum bending moment) can be found by varying the deterministic bending moment capacity C. Furthermore, by numerical differentiation of the distribution function, the corresponding probability density function may be obtained.

5.3 UNCERTAINTY ANALYSIS

When dealing with reliability analyses and statistical modelling, various types of uncertainties of the input parameters are represented as indicated in section 5.1. Relevant uncertainties may in general be divided into three different categories as given below, Melchers (1987). Furthermore, references for identification of uncertainties are e.g. Schneider (1981) and Henley & Kumamoto (1981).

Modelling uncertainty.

In the present study, this type of uncertainty is associated with the difference between the numerical models and the real behaviour of the riser in the sag-bend. The behaviour predicted by the local and the global model does not necessarily match the real behaviour perfectly. Some small deviations between estimated and real behaviour may be introduced when analytical expressions are employed in order to calculate the riser response caused by waves, current etc. This type of uncertainty is not accounted for in the probability analyses because they are not expected to influence the relative contributions to the reliability in the estimation of the chosen parameters.

Physical uncertainty.

Physical uncertainty is relevant for almost all kind of reliability assessment. This type is related to inherent random nature of different quantities, such as yield stress, Young's modulus, and wall thickness. Physical uncertainty may be reduced, but not eliminated, with larger amount of data, Thoft-Christensen and Baker (1982).

Statistical uncertainty.

These are uncertainties in computed statistical quantities (such as mean value, standard deviation calculated from a chosen probability distribution function) determined from a limited set of data for a parameter from the laboratory test. The probability distribution function and corresponding statistical estimators may be different for various samples. This uncertainty is described thoroughly in Benjamin & Cornell (1970).

5.4 RESPONSE SURFACE METHODS

Response surface methods were formally developed in the early 50s by G. E. P. Box and K. B. Wilson, Khuri and Cornell (1987). The objective of the use of response surface methods in this study is to establish an analytical approximation to the functional relationship between the estimated maximum bending moment capacity and the input variables. The response surface function will replace discrete estimates obtained by application of the non-linear finite element model by a smooth analytical function within a predefined area. This represents an approximation to the true under-

lying surface through all discrete values obtained from the analysis. This representation is similar to regression analysis for experiments. The procedure requires relatively few analyses to establish the probability of failure. Hence, the response surface method is an efficient and attractive alternative to numerous finite element analyses or conventional reliability analysis (e.g. Monte Carlo-simulations). The response surface consists of separate polynomial functions for each of the input parameters if correlated effects are negligible. If the combined effects are significant, a response surface as a function of the relevant parameters is to be established. Then, all the individual analytical approximations are multiplied and normalised (also called the multiplicative model). Generally, this response surface forms an n-dimensional space. If combined effects between some parameters are present, the contributions must be accounted for in each of the analytical expressions. It is important that the response surface provides an accurate prediction of the response close to the design point, Bucher and Bourgound (1990). Böhm and Brüchner-Foit (1992) outlined the structural response surface procedure as follows (also indicated in Karunakaran et al. (1995)):

1. A set of parametric studies is performed. A response surface is defined as the relationship between the 'structural response' and the parameters in the problem.

2. Reliability analyses are performed by using the established response surface in conjugation with FORM/SORM or Monte Carlo simulations.

Additionally, response surface methods relating to structural problems are described in e.g. Olivi (1984), Faravelli (1989), Faravelli & Bigi (1990), Rajashekhar & Ellingwood (1993) and Myers & Montgomery (1995).

5.5 RELIABILITY ANALYSIS PROCEDURE

The probability of failure refers herein to a given period, e.g. one year or the service life of the structure. The probability of exceedance for a design criterion is due to different input parameters that are stochastic. These input parameters are represented by the vector $\mathbf{X}$ in the limit state function $g(\mathbf{X})$. The relevant parameters and the failure function for this particular study are given in Section 5.6. However, the reliability procedure is outlined here. This procedure is given in Figure 5.5, Larssen et al. (1994).

1. A study is performed to identify parameters affecting the reliability analysis, i.e. the probability of failure. Possible uncertain parameters are being considered as random, while other parameters are deterministic.
2. A response surface is established for the maximum bending moment capacity, M_{max}. This response surface is based on a large number of finite element analyses.
3. The limit state function, $g(\mathbf{X})$, is defined as: $g(\mathbf{X}) = M_{max} - C$, where $\mathbf{X}$ is the vector of the uncertain parameters and C is a predefined level for the capacity.

4. For the random parameters in the vector **X**, statistical values (i.e. distribution functions with corresponding mean and coefficient of variation (C.o.V.)) are introduced.
5. The probability of failure and the corresponding importance factors are identified by calculations using FORM/SORM algorithms by application of the computer program PROBAN (1996).
6. Analytical probability distribution functions are derived from the numerically defined cumulative distribution functions for the maximum bending moment capacity.

In relation to item 6, different procedures can be applied. For the present purpose the cumulative distribution function is identified for a certain number of points and differentiated at the discrete points for the whole range of possible values of the maximum bending moment capacity.

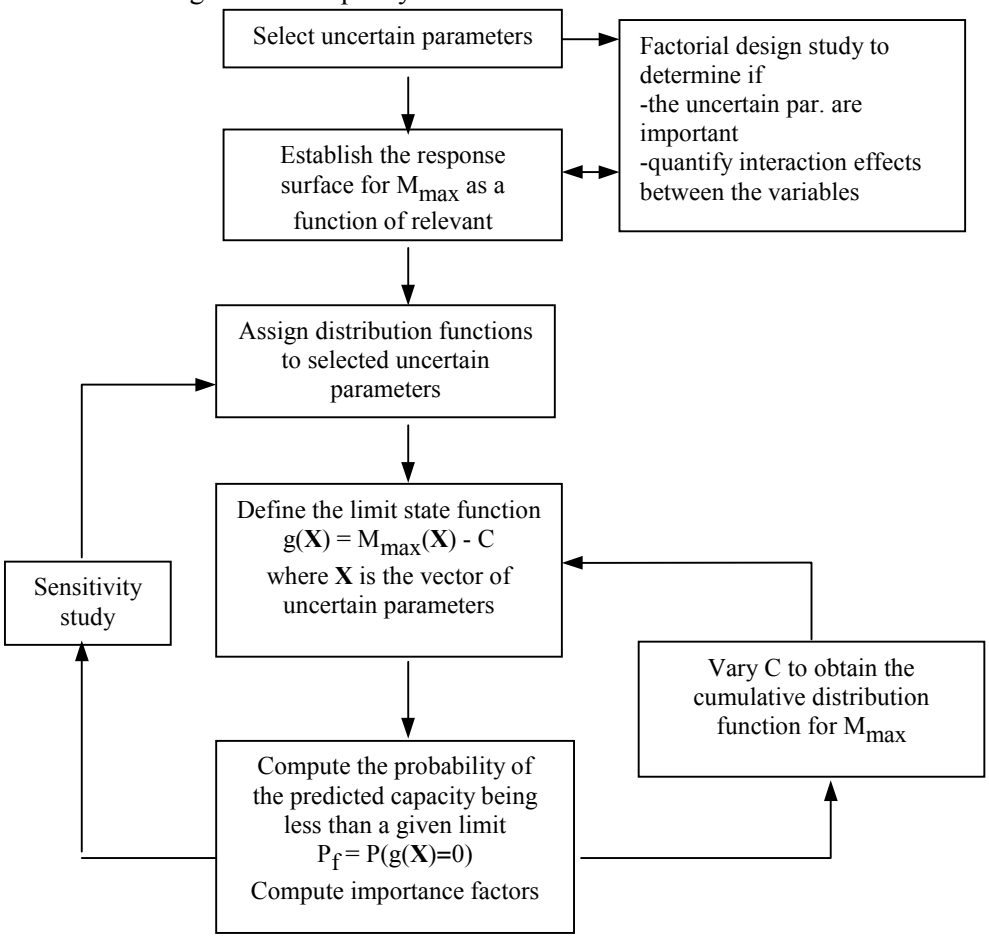

Figure 5.5 Reliability analysis procedure.

5.6 MAXIMUM BENDING MOMENT CAPACITY

Results of the finite element analyses of the maximum bending moment capacity as a function of the different uncertain input parameters are given herein. As described in previous chapters, the bending moment capacity is a function of both geometry and material parameters. These are identified in the list below:

Geometry parameters:

- Initial ovality.
- Uniform wall thickness and cross-sectional orientation.
- Piercer eccentricity.

Material parameters:

- Young's modulus.
- Yield stress.

The following considerations are made regarding low and high values for variation of the different parameters.

Initial ovality:

The titanium pipes do not have a perfect circular shape after production. A small value of out-of-roundness is commonly accepted and specified as permissible manufacturing tolerances. Acceptable tolerances are herein identified from DnV (1996), which are steel pipe values. This design code is a natural reference due to lack of design rules explicitly for titanium pipes. Maximum tolerances given in DnV (1996) for cases with nominal outer diameter less than 600 mm, D/t less than 75 and nominal wall thickness greater than 15 mm are relevant for the present analyses. These tolerances are given in Tables 5.1 and 5.2. The tables provide values both for pipe ends and pipe body. The requirements for the pipe ends are mainly due to welding considerations, and are somewhat stricter than for pipe body. Hence, the analyses of the maximum bending moment capacity are performed with pipe body tolerances.

Table 5.1. Standard and enhanced dimensional requirements for seamless pipes according to DnV (1996).

Characteristics	Standard requirement	Enhanced requirement
Diameter, pipe body	± 1.0 % D_e	±0.75 % D_e, -2mm / +4 mm
Out-of-roundness, pipe body	1.5 %, max 15 mm	1.5% & DM_{max}-DM_{min}<10mm
Nominal wall thickness	± 10 %	± 10 % & tm_{min}- t < +1.5 mm

D_e: nominal outer diameter

tm_{min} and t are measured minimum and nominal wall thickness, respectively.

Where there are two criteria, the larger one is to be used.

For the case of a seamless pipe, the key values are: D_i=20 in=508 mm, D/t=26, t=20.3 mm, D_e=548.6 mm. The corresponding permissible out-of-roundness-values corresponding to the requirements in Table 5.1 are calculated in Table 5.2.

Table 5.2. Calculated out-of-roundness-values for base case based on Table 5.1.

Characteristics	Standard requirements	Enhanced requirements
Diameter, pipe body	± 5.7 mm	-2 mm / +4 mm
Out-of-roundness, pipe body	± 7.5 mm	± 5.0 mm
Nominal wall thickness	± 2.0 mm	± 2.0 mm

The ovalization parameter, f, is defined as follows, DnV (1996):

$$f = \frac{D_{max} - D_{min}}{D}$$

where

D_{max}, D_{min} : maximum and minimum outer diameter, respectively.

D : nominal outer diameter.

By using values from Table 5.2, resulting ovality values may be identified (Table 5.3), which gives the actual range for the ovalization parameter which is applied in the present finite element analysis.

Table 5.3. Actual ovalities based on the requirements from Table 5.2.

Characteristics	Ovality (%) (standard requirements)	Ovality (%) (enhanced requirements)
Diameter, pipe body	2.08	1.09
Out-of-roundness, pipe body	2.73	1.82
Nominal wall thickness	0.73	0.73

As indicated in Table 5.3, the ovality of the pipe resulting from the manufacturing process may vary significantly (from 0.73 % up to 2.73 %). However, in DnV96, an initial ovality of at least 0.5 % is to be used as a minimum value, and is defined as a low value for the present analyses. For a high value of the initial ovality, the results from Table 5.3 is used as a basis together with the maximum ovality from a Serviceability Limit State (SLS) criterion point of view. The SLS criterion is 3 %, DnV (1996). This implies that the actual range of the ovality parameter may be from 0.5 % up to 3 %. However, 3 % initial ovality is not a relevant value since no further flattening of the cross-section is acceptable from a SLS criterion point of view. Hence, a high value of 2.5 % is chosen. This is close to the maximum value from Table 5.3. The three values for the initial ovality are given in Table 5.5.

Wall thickness and cross-sectional orientation:

For the wall thickness variation effect for the present FE-analyses, the following considerations are made:

FE-analyses are performed for constant wall thickness at low, nominal and high values.

The variation for the pipe tested in the laboratory is shown in Figure 3.7, where the values for both ends are given. The wall thickness does not appear to be symmetric relative to the nominal value, but varies from –5.4 % to +21.8 %. Since the majority of the measured values are greater than the nominal wall thickness, low and high values of this wall thickness are taken as -5 % up to +20 % of the mean wall thickness, respectively (this reference value is called ‘mean’ in Table 5.5).

The wall thickness will vary as a harmonic function (sine/cosine) as indicated in Chapter 3 (see Figure 3.4). However, the corresponding variation in the wall thickness in Figure 3.4 (with maximum value for zero degrees as a reference value), will change depending on the orientation of the cross-section. This is another aspect of the wall thickness modeling, namely, how the estimated maximum bending moment capacity is affected by the orientation of the cross-section. Three basic orientations are taken as starting values to identify the maximum bending moment capacity variation with this parameter:

(i) The minimum (t_{min}) and the maximum (t_{max}) wall thickness are at the compressive and tensile side of the cross-section, respectively, as indicated in Figure 3.7 for orientations between 0 degrees and 180 degrees (φ=0 is defined as low value in the parameter variation). See Figure 5.6.

(ii) Vice versa compared to (i) (φ=180 is defined as high value). See Figure 5.6.

(iii) The minimum value (t_{min}) is at the mid-node, and greater (not maximum) wall thickness is at the compressive and tensile side of the cross-section. This represents the orientation in between (*i*) and (*ii*) (φ=90 is defined as mean value), see Figure 5.6. Obviously, the cross-sectional symmetric properties fail as indicated in Figure 5.6. For values of the cross-sectional orientation (φ) between 0 and 180 degrees, the whole cross-section is modelled in ABAQUS.

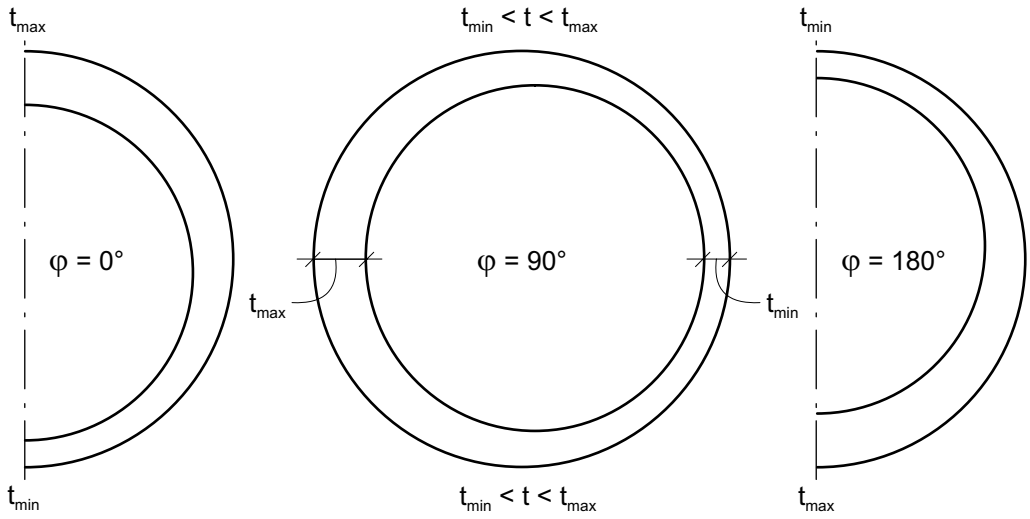

Figure 5.6 Definition of cross-sectional orientation.

Another aspect of wall thickness modeling, is the range from low to high values. As described above, the particular range of this variation used herein is from -5 % up to +20 % relative to the mean wall thickness. The source of this variation is the eccentricity of the centres of the rotating piercer relative to the titanium pipe during extrusion. If the piercer eccentricity is zero, the pipe will have a constant wall thickness. The wall thickness range will, however, become wider for increasing piercer eccentricity. In order to determine the influence of this effect on the maximum bending moment capacity, low and high values of the piercer eccentricity are defined. Zero piercer eccentricity is taken as the lowest value, implying a constant uniform wall thickness equal to the mean value. The maximum range of variation for the wall thickness (i.e. from –5 % up to +20 %) is taken as a high value of the piercer eccentricity. The wall thickness is varied as given in Figure 5.7 for different levels of the piercer eccentricity. A value of the piercer eccentricity equal to 0.5 is taken as the 'mean' value in Table 5.5.

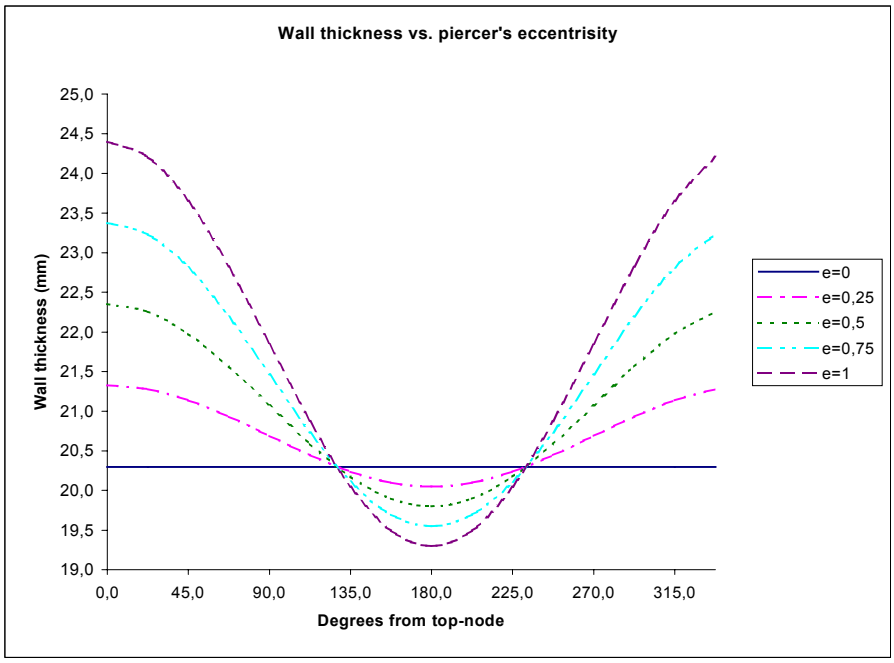

Figure 5.7 Wall thickness variation as a function of piercer eccentricity.

The greatest variation in the wall thickness ranges from 19.3 mm up to 24.4 mm for a piercer eccentricity equal to 1. This gives a total variation of 5.1 mm. The total variation of the wall thickness reduces to 3.8 mm, 2.6 mm and 1.3 mm for eccentricities equal to 0.75, 0.5 and 0.25, respectively.

Young's modulus:

Both low and high values are taken from the laboratory data. The Young's modulus has a mean value equal to 116 937 MPa, with corresponding low and high values of 102 937 MPa and 136 321 MPa, respectively. A coefficient of variance is identified as 5.5% from the laboratory tests. Implicitly, the low and high values -2.2 and +3.0 times the standard deviation in addition to the mean value, respectively.

Yield stress:

Three material curves are employed in the finite element analysis, represented by low, mean and high values of the yield strength. The mean value from the laboratory data is 831.3 MPa, with corresponding low and high values equal to 807.9 MPa and 857.9 MPa, respectively. The coefficient of variation for this particular parameter is 1.61 %,

leading to low and high values equal to –1.7 and +2.0 times the standard deviation in addition to the mean value, respectively. The mean value is taken as the mean stress-strain relationship of all tests from the laboratory (mean curve in Figure 3.3), and in addition the corresponding minimum and maximum curves given in Figure 5.8. They are all fitted well by the Voce material model, see Section 4.5. A summary of the material constants for the three relevant curves is given in Table 5.4.

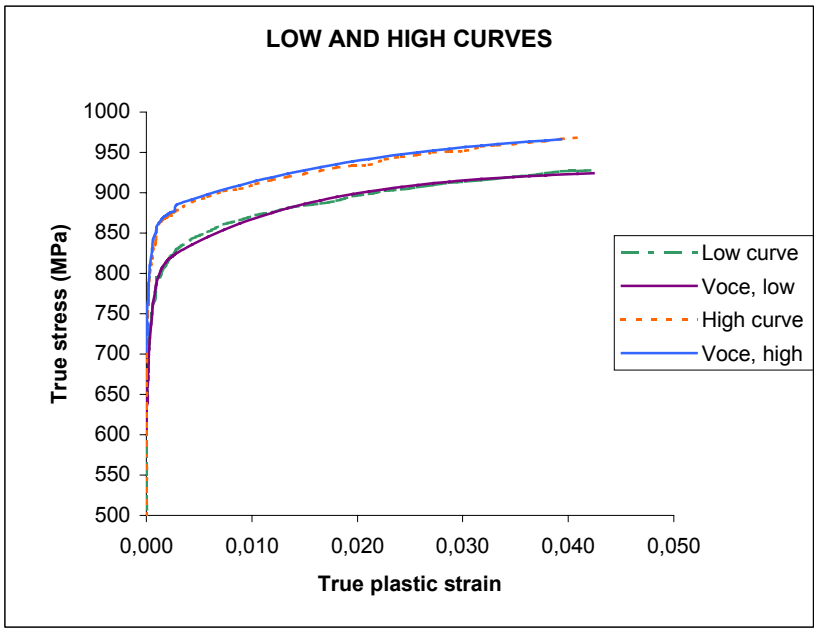

Figure 5.8 Low and high material curves for the finite element analysis.

Table 5.4. Table of material model constants (Voce) for the three curves used in the analysis represented by low, mean and high levels of yield strength.

Curve	σ_{EL}	R_1	R_2	C_1	C_2
Low	622.1	179.4	128.8	2146.7	71.1
Mean	694.5	142.9	126.9	1455.3	54.3
High	717.1	145.9	121.6	2157.5	46.3

The parameters for all curves are identified by the use of the ‘least-square-method’.

Table 5.5 summarises all input parameters with corresponding low, mean (reference) and high values.

Table 5.5. Values of the parameter variations.

Parameter	Symbol	Unit	Low	Mean (reference)	High
Initial ovalization	f_0	(%)	0.5	1.5	2.5
Uniform wall thickness	t	(mm)	19.3	20.3	24.4
Orientation	o	(degrees)	0	90	180
Piercer eccentricity	e	-	0	0.5	1.0
Young's modulus	E	(N/mm^2)	102 935	116 937	136 321
Yield stress	σ_Y	(MPa)	807.9	831.3	857.9

The results of the predicted maximum bending moment capacity as a function of the parameters given in Table 5.5 are shown graphically in the next section. A summary of the results corresponding to the low, mean (reference) and high values, and corresponding differences relative to the base case (defined below), is given in Table 5.6. This allows a quantification of the influence from the different input parameters.

Base case:

The base case is chosen to be a pipe with internal diameter equal to 20 inches (508 mm), a wall thickness of 20.3 mm and implicitly 'mean diameter to thickness'-ratio (D/t) equal to 26.

Table 5.6. Selected normalised maximum bending moment capacities[2] as function of the input parameters (normalising factor is 1.778E9 Nmm).

Parameter	Low	Mean	High
Initial ovalization	1.0377	1.00	0.9584
Uniform wall thickness	0.8009	1.00	1.4741
Young's modulus	0.8583	1.00	1.1074
Orientation	1.2345	1.2531	1.2018
Piercer eccentricity	1.000	1.1507	1.2345
Yield stress	0.9708	1.000	1.0309

'Dev.' is to be interpreted as deviation compared to normalised factor (also referred to as mean value of the predicted bending moment capacity).

It is seen from Table 5.6 that all six parameters influence the predicted maximum bending moment capacity. However, the initial ovality and yield stress have relatively small effect based on the variation range (low to high values), only about ± 3 - 4 %. By

[2] The bending moment value refers to half of the total cross-section. The total maximum bending moment capacity of the whole cross-section is, hence, to be multiplied with 2.

changing the other parameters from their respective low to high values, the maximum bending moment capacity varies from –20 % up to +47 % for the most governing parameter (i.e. the uniform wall thickness). The variation in the Young's modulus leads to a reduced and increased maximum bending moment capacity equal to –14 % and +11 %, respectively. The total range of variation for the piercer eccentricity and the cross-sectional orientation parameters are 17 % and 23 %, respectively.

5.7 FACTORIAL DESIGN ANALYSIS

The results in Table 5.6 represent the variation of the 'response quantity' as a function of all parameters. The numbers correspond to changing one parameter at a time, and keeping the other at their corresponding mean/reference values. However, these analyses do not identify potential interaction effects between some of the parameters. By using the factorial design analysis method, it is possible to identify correlation effects by performing analyses of certain combinations of a low and a high value of the input parameters. To obtain a complete check of the relative importance for n parameters and their corresponding potential interaction effects, the number of cases that need to be analysed is 2^n. Table 5.7 and 5.8 indicated a factorial design analysis for the parameters given in Table 5.5. However, the initial ovality and the yield stress are neglected in the present interaction analyses, due to their small influence on the maximum bending moment capacity based on their low and high values given in Table 5.5. Hence, four parameters remain to be controlled, i.e. the Young's modulus, uniform wall thickness, piercer eccentricity and cross-sectional orientation. Obviously, having a uniform wall thickness is not possible to combine with the piercer eccentricity parameter (except for e=0). The factorial design procedure is thus subdivided into two parts. The potential interaction effect from the Young's modulus, the piercer eccentricity and the cross-sectional orientation is checked. Separately, the interaction effect between the Young's modulus and the uniform wall thickness is also controlled. The values in the last row of the table is to be interpreted as the *change* in the maximum bending moment capacity when moving from low to high value of each parameter. The corresponding values for a single parameter (i.e. E, e or o), are called single-factor effect. Similarly, the influence from two and three parameters is called two- and three-factor effect, respectively. When identifying the different effects on the response quantity, it is important to identify the relative contribution. Tables 5.7 and 5.8 summarise the factorial design analysis performed for the present set of parameters. The numbers in the column called 'FEM', represent results from ABAQUS.

It is seem from Tables 5.7 and 5.8 that two-factor and three-factor contributions are negligible for the estimated maximum bending moment capacity. However, the calculations indicate that there is some interaction between the piercer eccentricity (e) and the cross-sectional orientation (o).

Table 5.7. Factorial design for Young's modulus (E), piercer eccentricity (e) and cross-sectional orientation (o).

E	e	o	Ee	Eo	eo	Eeo	FEM
-	-	-	+	+	+	-	1.607
+	-	-	-	-	+	+	2.030
-	+	-	-	+	-	+	1.623
+	+	-	+	-	-	-	2.047
-	-	+	+	-	-	+	1.747
+	-	+	-	+	-	-	2.109
-	+	+	-	-	+	-	2.060
+	+	+	+	+	+	+	2.299
0.362	0.134	0.227	-0.03	-0.062	0.118	-0.031	

Table 5.8. Factorial design for Young's modulus (E) and uniform wall thickness (t).

E	t	Et	FEM
-	-	+	1.014
+	-	-	1.71
-	+	-	2.545
+	+	+	2.691
0.421	1.256	-0.275	

5.8 ADOPTED RESPONSE SURFACE

Since interaction effects between the parameters are negligible (excluding the combination effect of the piercer eccentricity and the orientation), the response function of the maximum bending moment capacity can be given as a product of separate functions of the parameters. The effect of the piercer eccentricity and the orientation is represented by a two-dimensional surface. The curve and surface fitting procedure is based on the least-square-method and fitted to the FEM-results. One parameter is varied at a time, while the other parameters are kept at their corresponding mean/reference values. Figure 5.8 to 5.11 represent the curve fitting for the initial ovalisation, the Young's modulus, the yield strength and the uniform wall thickness. Figure 5.14 represents the surface resulting from variation of both the piercer eccentricity and the cross-sectional orientation. To determine the order of the polynomial function for the surface, a curve fitting procedure is used for a separate variation of both parameters, see Figures 5.12 and 5.13. The surface is then defined as a function of both parameters (see explanations previous to Table 5.12).

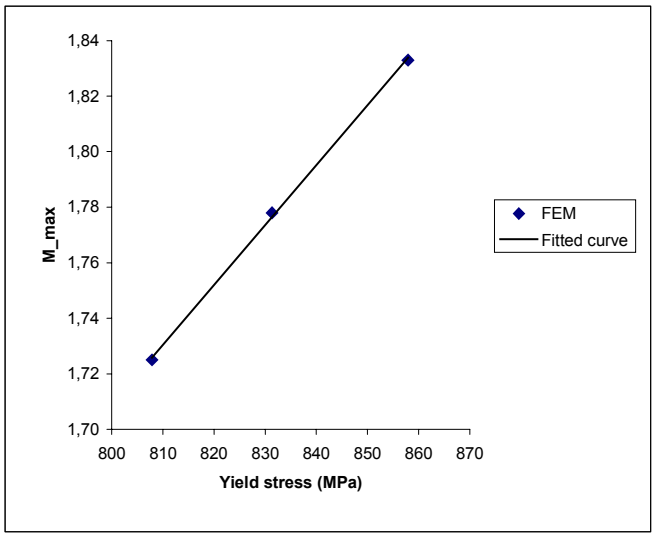

Figure 5.8 Curve fitting for the yield stress.

For the yield stress (Figure 5.8) the maximum observed deviations are less than 0.1 % for the linear curve fit.

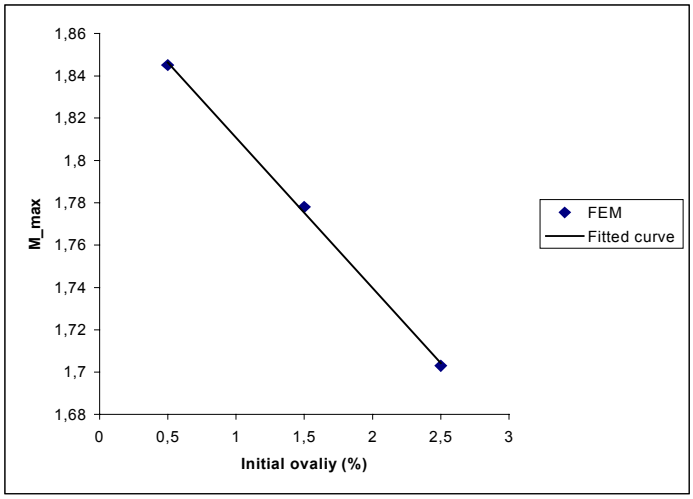

Figure 5.9 Curve fitting for the initial ovalities.

A linear representation fits the FEM-analyses for various initial ovalities very well (Figure 5.9). Maximum observed deviation is less than 0.1 %.

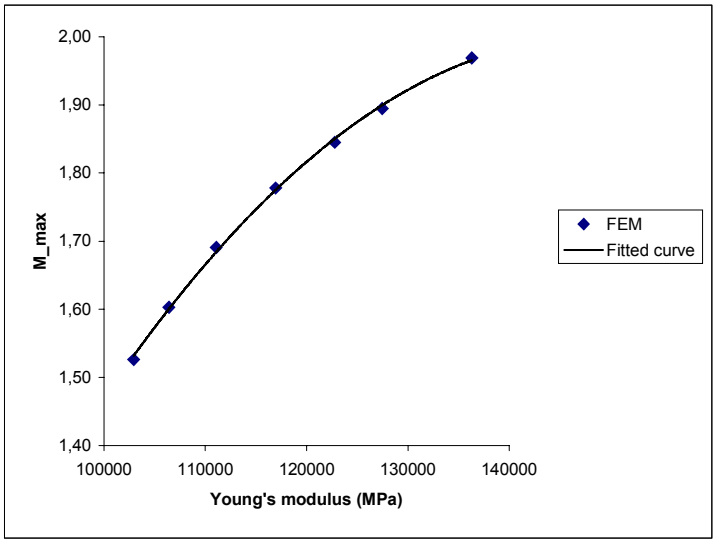

Figure 5.10 Curve fitting for the Young's modulus.

The curve in Figure 5.10 is parabolic. A 2nd degree polynomial represents this behaviour (i.e. observed deviations are less than ± 0.4 %).

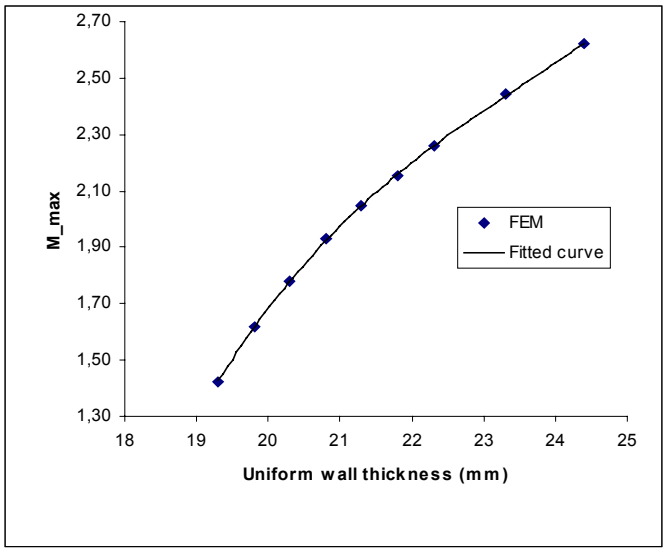

Figure 5.11 Curve fitting for the uniform wall thickness.

The variation of the maximum bending moment capacity due to the uniform wall thickness variation is obviously non-linear. A polynomial of 3rd degree implies maximum observed deviations between – 0.5 % and 0.2 %.

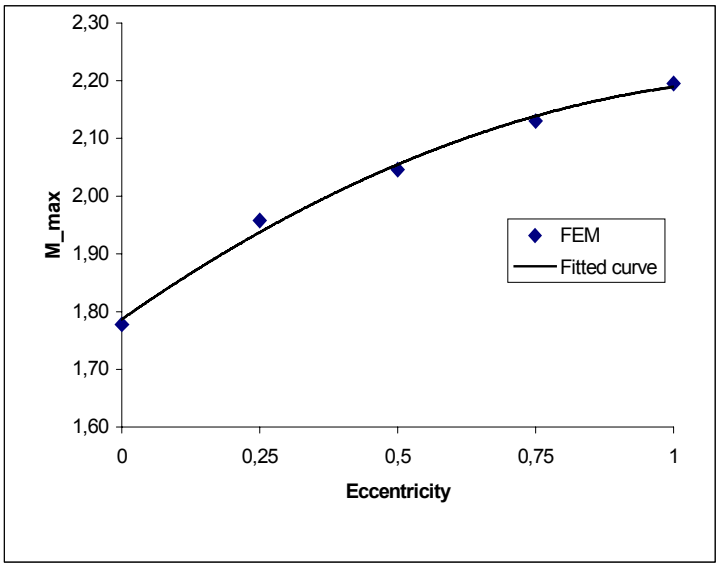

Figure 5.12 Curve fitting for the eccentricities (o=0 degrees).

The response curve given in Figure 5.12 is represented by a 2nd degree polynomial, which gives maximum deviations between – 1 % and + 0.5 % from the FE-analyses.

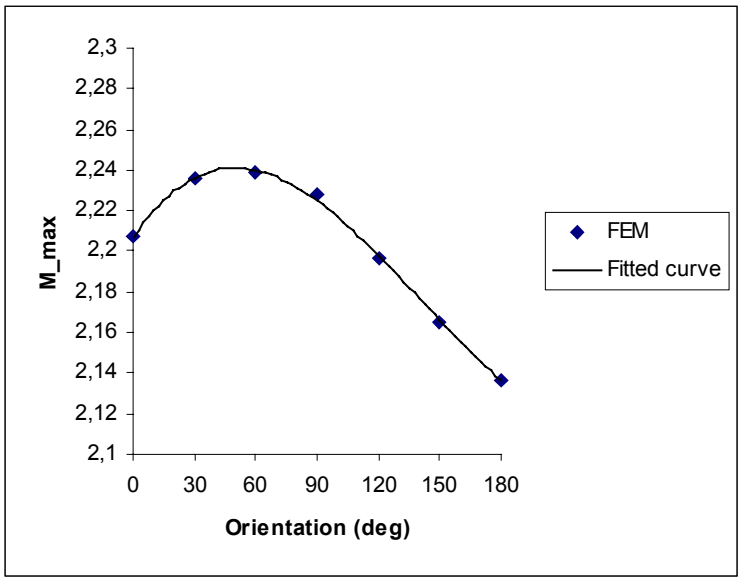

Figure 5.13 Curve fitting for various cross-sectional orientations (at maximum piercer eccentricity, i.e. e=1)

The influence on the maximum bending moment capacity from the cross-sectional orientation can be described by a polynomial function of 3rd degree. The maximum observed deviations are between – 0.06 % and + 0.15 %.

The polynomial degree of the curves for both the piercer eccentricity and the cross-sectional orientation are based on Figures 5.12 and 5.13, respectively. The coefficients for the surface equation are based on 37 different combinations of the two parameters. The surface is shown in Figure 5.14 and the calculations are as follows:

Let **C** be the unknown coefficient vector with dimension 12×1 (i.e. 12 unknown coefficients, see Table 5.10). Furthermore, the matrix **A** represents the values of the product $o^i \cdot e^j$, where $i \in [0,3]$ and $j \in [0,2]$. The dimension of **A** is 37×12 (i.e. 37 combinations are used). The vector, **M**, is given as the estimated maximum bending moment capacity as a function of the different parameter combinations (dimension 37×1). The following equation is obtained:

$$\mathbf{A} \cdot \mathbf{C} = \mathbf{M} \tag{5.7}$$

Since the numbers of rows and columns in **A** differ, the inverse of **A** does not exist. The vector **C** is, hence, solved by multiplying the transposed matrix, $\mathbf{A^T}$, on both sides, and defining $\mathbf{A^T} \cdot \mathbf{A} = \mathbf{A^*}$ and $\mathbf{A^T} \cdot \mathbf{M} = \mathbf{M^*}$. Equation (5.7) is then modified to Equation (5.8):

$$\mathbf{A}^T \cdot \mathbf{A} \cdot \mathbf{C} = \mathbf{A}^T \cdot \mathbf{M} \Leftrightarrow \mathbf{A^*} \cdot \mathbf{C} = \mathbf{M^*} \tag{5.8}$$

Simple matrix operations give the solution of Equation (5.8), by multiplying the inverse matrix of $\mathbf{A^*}$ on both sides. This gives:

$$\mathbf{A^{*-1}} \cdot \mathbf{A^*} \cdot \mathbf{C} = \mathbf{A^{*-1}} \cdot \mathbf{M^*} \Leftrightarrow \mathbf{C} = \mathbf{A^{*-1}} \cdot \mathbf{M^*} \tag{5.9}$$

The maximum observed deviations from the surface and the FEM results for Figure 5.14 are between – 0.8 % and + 2.0 %.

The total response surface is hence dependent on all the single curves and the two-dimensional surface given above, and may be divided into separate response functions. The single curves are established from the variation of the relevant parameters separately by keeping the other parameters at their mean values (called reference values, M_{ref}). The separate functions for the maximum bending moment are given in Table 5.9.

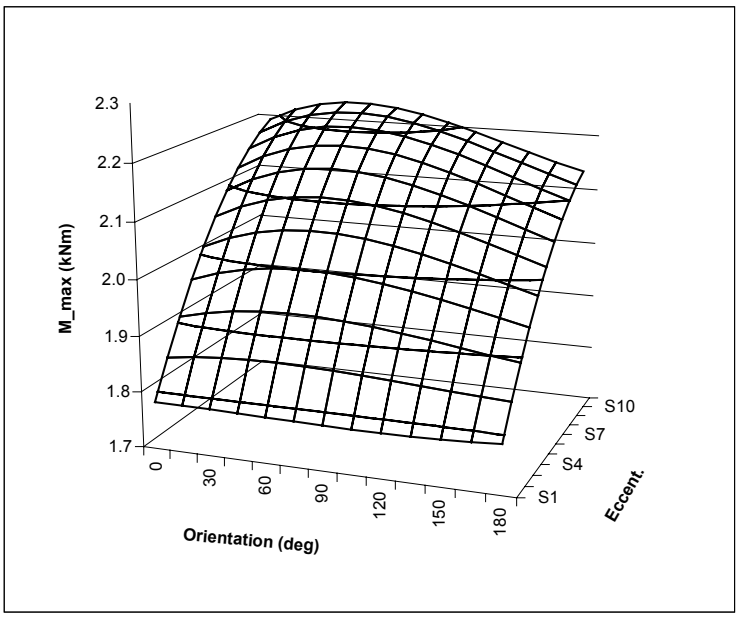

Figure 5.14 Surface for various combinations of cross-sectional orientations and piercer eccentricities. The piercer eccentricity varies from zero to the maximum value (e=1). It is to be noted that the diagram is topographical, i.e. the horizontal lines represent corresponding values of M_{max}.

The response surface is subsequently given as the normalised product of the function fitted along each of the variable axes (see Section 5.4 for discussion related to response surfaces

$$M(f_0, E, \sigma_Y, t, oe) = M_{ref} \cdot \prod_{i=1}^{4} \left(\frac{M_{\max}^{X_i}}{M_{ref}^{X_i}} \right) \cdot \frac{h\left(M_{\max}^{o}, M_{\max}^{e}\right)}{M_{ref}^{oe}} \tag{5.10}$$

where X_i refers to f_0, E, σ_Y, t ($M_{ref}^{f_0} = M_{ref}^{E} = M_{ref}^{\sigma_Y} = M_{ref}^{t} = M_{ref}^{oe} = M_{ref}$ according to the definition of the base case) and h(.) is the analytical expression for the surface in Figure 5.14.

Table 5.9. Curve and surface fitting results.

Parameter	**Formula for maximum bending moment capacity**
Initial ovality	$M_{\max}(f_0) = -0.071 \cdot f_0 + 1.8818$
Yield stress	$M_{\max}(\sigma_Y) = 0.001496 \cdot \sigma_Y + 0.4383$
Young's modulus	$M_{\max}(E) = -2.22626 \cdot 10^{-10} \cdot E^2 + 6.7128 \cdot E - 2.9808$
Uniform wall thickness	$M_{\max}(t) = 0.0043268 \cdot t^3 - 0.30595 \cdot t^2 + 7.3793 \cdot t - 58.139$
Piercer eccentricity and cross-sectional orientation	$M_{\max}(o,e) = C_1 \cdot o^3 e^2 + C_2 \cdot o^3 e + C_3 \cdot o^2 e^2 + C_4 \cdot o^2 e + C_5 \cdot o e^2 + C_6 \cdot o e + C_7 \cdot o^3 + C_8 \cdot o^2 + C_9 \cdot o + C_{10} \cdot e^2 + C_{11} \cdot e + C_{12}$
Piercer eccentricity (o=0)	$M_{\max}(e) = -0.2674 \cdot e^2 + 0.6698 \cdot e + 1.7868$
Cross-sectional orientation (e=1)	$M_{\max}(o) = 0.0427 \cdot 10^{-6} \cdot o^3 - 0.181 \cdot 10^{-4} \cdot o^2 + 0.1482 \cdot 10^{-2} \cdot o + 2.2068$

where the constants C_1, C_2, …, C_{12} are given in Table 5.10.

Table 5.10: Constants for $M_{max}(o,e)$.

C_1	C_2	C_3	C_4	C_5	C_6
-0.03015E-6	0.07145E-6	0.26826E-4	-0.45703E-4	-0.36108E-2	0.53197E-2
C_7	C_8	C_9	C_{10}	C_{11}	C_{12}
0.007184E-6	-0.01258E-4	0.001317E-2	-2.6728E-1	6.7458-1	1.7849

5.9 CONTROL OF THE ADOPTED RESPONSE SURFACE

To verify the established response surface, analyses for various combinations of the input parameters are performed. Some relevant combinations and the results are given in Table 5.11. The last column gives the ratio between the bending moment calculated from the response surface (M_{RS}) and the corresponding result from ABAQUS (M_{FEM}).

Small deviations are in general identified for the response surface as compared to the ABAQUS analyses. The largest deviations are –2.1 % and +1.1 %. This occurs for the combination of cross-sectional orientation and piercer eccentricity different from the mean/reference (μ) values. The adopted response surface accordingly represents the

maximum bending moment capacity sufficiently well and is suited as a basis for the reliability analyses in the next section.

Table 5.11. Results for a selected set of combinations of the input parameters.

E	t	e	o*	f_0	σ_Y	M_{RS}/M_{FEM}
high	μ	low	μ	μ	μ	.989
low	μ	low	μ	μ	μ	.994
μ	low	low	μ	μ	μ	.994
μ	high	low	μ	μ	μ	.994
μ	μ	high	μ	μ	μ	.994
μ	μ	low	high	μ	μ	.990
μ	μ	low	low	μ	μ	.987
μ	μ	low	μ	high	μ	.991
μ	μ	low	μ	low	μ	.991
μ	μ	low	μ	μ	high	.990
μ	μ	low	μ	μ	low	.990
μ	μ	high	30	μ	μ	.994
μ	μ	high	60	μ	μ	.993
μ	μ	high	90	μ	μ	.992
μ	μ	high	120	μ	μ	.993
μ	μ	high	150	μ	μ	.993
μ	μ	high	high	μ	μ	.993
μ	μ	.25	60	μ	μ	1.009
μ	μ	.25	120	μ	μ	1.011
μ	μ	.5	low	μ	μ	.986
μ	μ	.5	30	μ	μ	.997
μ	μ	.5	60	μ	μ	.983
μ	μ	.5	120	μ	μ	.983
μ	μ	.5	150	μ	μ	.991
μ	μ	.5	high	μ	μ	.989
μ	μ	.75	30	μ	μ	.986
μ	μ	.75	60	μ	μ	.979
μ	μ	.75	120	μ	μ	.988
μ	μ	.75	150	μ	μ	.985
μ	μ	.75	high	μ	μ	.987
μ	μ	low	any	μ	μ	.996< <1.000

5.10 STATISTICAL MODELING OF THE UNCERTAIN PARAMETERS

The maximum predicted bending moment capacity depends on the input parameters given in Sections 5.6 and 5.7. Statistical data (i.e. distribution, mean value and C.o.V.)

* Low and high values refer to zero and 180 degrees, respectively.

related to these parameters are to be identified before probability analyses can be performed. The results are summarised in Table 5.12. The background regarding choice of parameter ranges is provided in the following.

The test data from the laboratory does not support a final recommendation for statistical distribution for any of the relevant parameters due to a limited number of test results. The present data from the laboratory are plotted on different types of probability paper, for possible identification of the distribution of the different parameters. To fit the distribution, the parameter values shall appear as a straight line when a sufficient amount of test data is available. This is not the case for the present laboratory tests due to the limited length of titanium pipe available. For some of the parameters, the values given in Jiao et al (1995, 1996) and Jiao, Sotberg & Bruschi (1995) are used as a basis for the choice of distribution and C.o.V. A summary of the statistical data for the input parameters is given in Table 5.12.

No experimental data is available for the initial ovality parameter. A lognormal distribution for the initial ovality is recommended by the SUPERB-project[3]. A C.o.V. of 25 - 60 % is suggested for welded pipes. However, it is further emphasised that larger values are expected for seamless pipes. Somewhat higher values are accordingly selected here.

The mean value for the uniform wall thickness is taken as the nominal value (i.e. 20.3 mm). Values of the C.o.V. are in the range from 2 % up to 6 % (Corresponding values in SUPERB are 2 % and 4.6 %). A truncated normal distribution is employed, since values exceeding the low/high boundary may influence the probability calculations significantly. Additionally, a uniform wall thickness exceeding the corresponding low/high values, are considered as unrealistic.

The corresponding statistical reference values for the Young's modulus are based on the experiments in the laboratory. The C.o.V. is found to be equal to 5.5 %. This parameter is modelled as a Gaussian variable. The low and high values are set equal to 3 % (SUPERB) and 7 %, respectively.

The cross-sectional orientation of the riser is not governed by any specific parameter during laying or in the operational condition. This parameter may hence obtain any value between zero and 180 degrees, and is modelled as uniformly distributed.

There is lack of information when it comes to the eccentricity of the piercer. However, eccentricity is always positive, and may exceed the high value in Table 5.5. When manufacturing pipes, the production tolerances are attempted to be kept at a minimum.

---

[3] SUPERB was a large R&D-project on pipelines performed by MARINTEK Structural Engineering (former SINTEF Structural Engineering), DnV and Snamprogetti 1992-96. Some OMAE-papers are published based on this project, see e.g. SUPERB (1996), Jiao et al. (1995, 1996, 1997) in the reference list.

This explains that the eccentricity parameter tends to be closer to the low value than the high value in Table 5.5. A lognormal distribution seems to be a reasonable choice. The coefficient of variation is set equal to 5 %, 10 % and 15 %.

The yield stress is normally distributed and has a C.o.V. from the laboratory tests close to 2 % (equal to 1.6 %). 2 % is taken as low value. The reference and high values are 4% and 6 %, respectively (both from SUPERB).

Table 5.12. Statistical properties of the input parameters.

			C.o.V.		
Parameter	**Symbol**	**Distribution**	**Low**	**Reference**	**High**
Initial ovalization	f_0	Lognormal	30 %	50 %	70 %
Uniform wall thickness	t	Trunc-normal	2 %	4 %	6 %
Young's modulus	E	Normal	3 %	5.5 %	7 %
Cross-sectional orientation	o	Uniform	58 %	58 %	58%
Piercer eccentricity	e	Lognormal	5 %	10 %	15 %
Yield stress	σ_Y	Normal	2 %	4 %	6 %

The reason for the choice of three different levels for the C.o.V.s for all parameters is due to a limited amount of material. The tests in the laboratory are too few to come up with suggestion of a specific set of C.o.V. for the corresponding parameters. Hence, three different sets of C.o.V is introduced (given as low, reference and high in Table 5.12).

5.11 PROBABILITY ANALYSIS

The cumulative distribution function of the maximum bending moment is obtained by performing reliability calculations for a range of values of the threshold level C in Equation (5.5). By numerical differentiation of the distribution function, the corresponding probability density function is subsequently obtained. The resulting probability density function for the estimated maximum bending moment capacity, based on statistical parameters as given in Table 5.12, is shown in Figure 5.15.

For the lowest values of C.o.V. (continuous line in Figure 5.15), the function becomes more 'narrow' compared to the other two curves. Contrarily, the same phenomenon applies when larger coefficients of variance are used. Hence, the density function becomes 'wider'. The corresponding density curves in Figure 5.15 may be used to identify the type of analytical distribution relevant for the estimated maximum bending moment capacity. The data are plotted on various types of probability paper, see Figure 5.16 and Appendix A. Figure 5.16 shows a Gaussian distribution for the set of C.o.V. referred to as 'low' in Table 5.12.

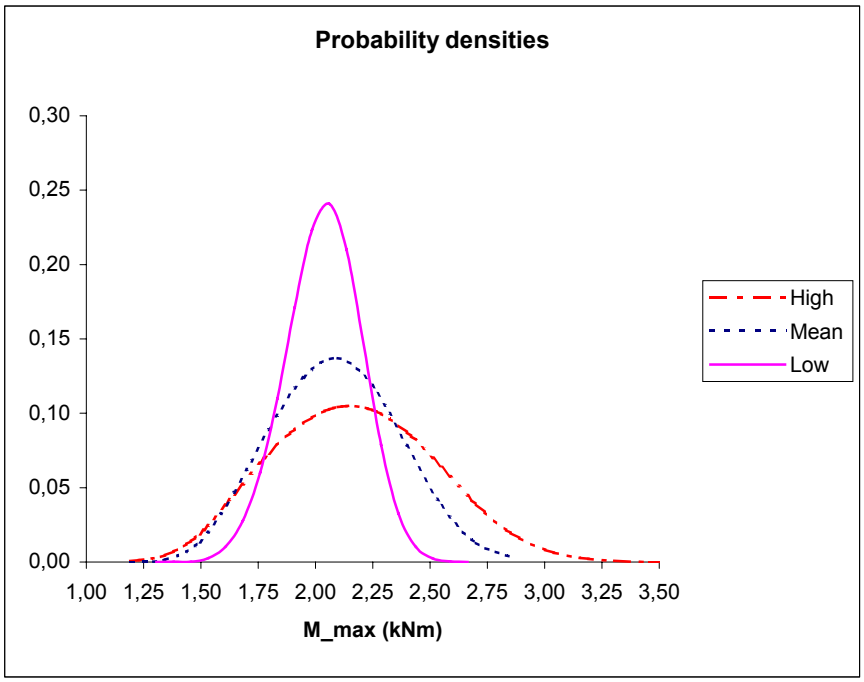

Figure 5.15 Probability densities of the estimated maximum bending moment capacity.

The data for the estimated maximum bending moment capacity appears as a straight line in this Gaussian plot indicating a very close fit to the Gaussian distribution. This is verified by the so-called R^2-factor, which indicates how well a sample fits to a distribution. If R^2 is equal to 1.0, a perfect match is present. For the particular data given in Figure 5.17, R^2 is equal to 0.999, which is considered as a very close fit to the Gaussian distribution. The same applies to the sets of C.o.V. referred to as 'low' and 'high' in Table 5.12. However, for the corresponding 'high' and 'mean' values, a lognormal distribution fits the data almost just as well as the Gaussian distribution. The lognormal distribution can be given a certain plausibility in accordance to the Central Limit Theorem, which says that the product of a large number of independent variables, becomes lognormally distributed, Dougherty (1990). Table 5.13 summarises the corresponding R^2-factors for various distributions of the maximum bending moment capacity.

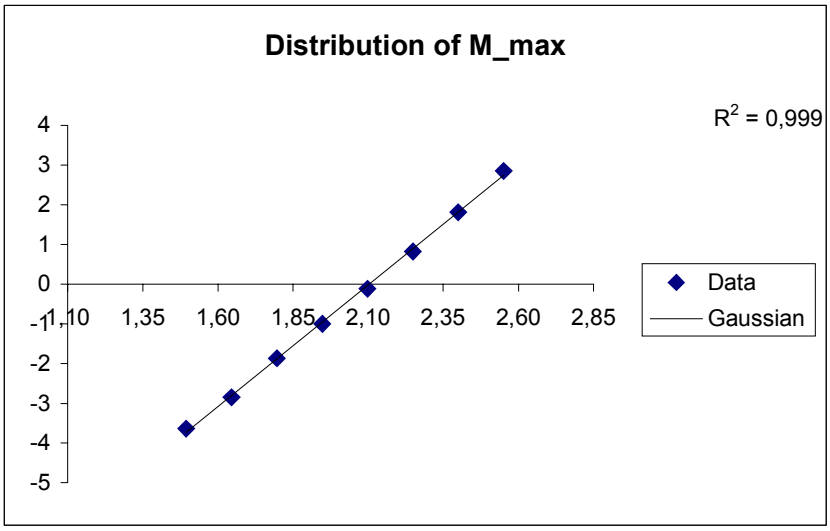

Figure 5.16 Distribution of estimated maximum bending moment capacity.

Table 5.13. R^2-factors for various distributions.

Set of C.o.V.	Gaussian	Lognormal	Weibull	Gumbel
Low	.999	.989	.962	.897
Mean	.994	.992	.952	.956
High	.995	.9947	.944	.941

To identify which parameter that influences the probability of failure the most, importance factors for the input parameters are identified. Table 5.14 shows the variation of the importance factors for the basic random variables as a function of the threshold level.

Table 5.14. Importance factors for basic variables as a function of threshold levels.

Set of C.o.V.	M_{max} (kNm)	Cumm. prob.	Importance factors					
			t	E	σ_Y	o	e	f_0
Low	1.419	1.4E-4	40.2	30.4	4.5	7.6	.4	16.9
	2.023	.544	74.4	12.6	3.3	.5	.4	4.3
	2.475	.998	67.9	18.2	6.5	.9	.9	5.6
Mean	1.268	1.16E-4	24.3	51.5	5.1	.9	.5	14.7
	2.023	.414	75.8	14.4	4.3	1.6	.5	3.2
	2.777	.995	64.1	19.1	10.1	.7	1.4	4.5
High	1.117	1.81E-4	11.1	4.8	1.4	.4	.2	82.3
	1.268	1.03e-3	25.9	50.4	6.6	2.3	.7	14.2
	2.173	.512	73.7	14.9	6.5	1.0	.8	3.1
	3.230	.999	59.2	17.7	16.3	.6	.3	4.0

The tendencies are the same for all sets of combinations of C.o.V. The uniform wall thickness, the Young's modulus and the initial ovality dominate for small bending moment capacities. For high bending moment capacities the two former parameters dominate. The piercer eccentricity parameter has almost a negligible influence on the maximum bending moment capacity when acting separately. The importance factor varies from zero to 1.4 %. However, this parameter is to be combined with the cross-sectional orientation parameter, which gives a contribution about 2 - 3 %, except for low bending moment capacities for the set of C.o.V. referred to as 'low'. There is a contribution from the initial ovality (typically 3 - 5 %), except for very low capacities where this contribution becomes significant. This is reasonable since the problem is dominated by the pressure and not by the bending. The external pressure is about 70 % of the critical pressure. For the lowest bending moment capacity when the set of C.o.V. referred to as 'high' is used, the importance factor for the initial ovality is as high as 82.3 %. This is explained by the fact that the cross-section is being significantly ovalized even at low levels of the external pressure, due to its relatively low Young's modulus. Hence, the initial ovality influences the maximum bending moment capacity considerably if the cross-section is subjected to a large ovality before external loads are applied.

C h a p t e r 6

LOCAL BUCKLING AND COLLAPSE DESIGN

"Though this be madness, yet there is method in it."
Hamlet, 2,2.
William Shakespeare (1564-1616).

6.1 INTRODUCTION

Several design codes are available for checking of acceptable strength of steel pipelines and risers subjected to bending and external overpressure. The steel formulas may not be readily applicable to titanium. This chapter focuses on how local bending capacity and possible collapse for titanium risers are represented by the corresponding formulas for steel pipes in a relevant code among the existing guidelines, i.e. DnV (1996).

6.2 DESIGN CHECK FORMULAS

Murphey and Langner (1985) proposed a format of a buckling criterion that has been frequently used.

$$\left(\frac{\varepsilon}{\varepsilon_c}\right)+\left(\frac{p_e}{p_c}\right)=\frac{1}{S_f} \tag{6.1}$$

where

ε / ε_c	applied strain / critical strain
p_e / p_c	applied external pressure / critical external pressure
S_f	safety factor

The critical bending strain is given by, British Standard, BS 8010 (1993).

$$\varepsilon_c = 15\cdot\left(\frac{t}{D}\right)^2 \tag{6.2}$$

where

t	wall thickness
D	external diameter

The critical external pressure, p_c, is found from Equation (6.3), e.g. in Timoshenko and Goodier (1970).

$$p_c{}^2-\left(2\cdot\sigma_Y^*\cdot\frac{t}{D}+\left(1+3\cdot\delta_0\cdot\frac{D}{t}\right)\cdot p_{el}\right)\cdot p_c+2\cdot\sigma_Y^*\cdot\frac{t}{D}\cdot p_{el}=0 \tag{6.3}$$

where

p_{el} elastic Euler buckling pressure $p_{el}=\dfrac{2\cdot E}{1-\nu^2}\cdot\left(\dfrac{t}{D}\right)^3$ (6.4)

δ_0 ovalization parameter defined by $\delta_0=\dfrac{D_{\max}-D_{\min}}{D_{\max}+D_{\min}}$ (6.5)

$\sigma_Y{}^*$ reduced specified minimum yield stress (SMYS) taking the pipe wall axial stress, σ_a, into account: $\sigma_Y^*=\sigma_Y\cdot\left[\left(1-\dfrac{3\cdot\sigma_a^2}{4\cdot\sigma_Y^2}\right)^{0.5}-\dfrac{\sigma_a}{2\cdot\sigma_Y}\right]$ (6.6)

σ_a is set equal to the true axial wall stress. Set to zero if compression.

The lowest value of the two possible critical pressure values from Equation (6.3) shall be used in Equation (6.1). Experiments on steel materials are the basis of this formula and potential uncertainties when employing them to titanium is emphasised.

An alternative buckling / collapse criterion is taken from DnV (1996), and separates between load- and displacement-controlled cases, explained in the following:

The relation between the bending moment and the bending strain is strongly non-linear. For a bending dominated condition, a small change in the bending moment may imply a significant change in the bending strain when the ultimate capacity is reached. In commonly employed design codes (e.g. DnV, 1996), the cases for load- and displacement controlled scenarios are distinguished when it comes to buckling and collapse analysis. The two different types may be defined as follows, Larsen (1996):

Load-controlled	**Displacement-controlled**
The riser is subjected to bending that in its nature is controlled by loads or bending moment, implying that the controlling parameter is the bending moment. The bending moment capacity interaction formula is given by Equation (6.7).	The riser is subjected to bending that in its nature is controlled by its displacements or curvature, implying that the controlling parameter is the bending strain. The bending moment capacity interaction formula is given by Equation (6.8).

In other words, the difference between the two cases may also be explained by the contribution to its load carrying mechanisms (i.e. for a catenary riser this is: (a) bending (elastic) stiffness defined by the cross-section stiffness, and (b) geometric stiffness related to its effective tension). A load-controlled case is where the bending stiffness dominates, since equilibrium is obtained by change of stresses and, implicitly, bending moments. On the contrary, the geometric stiffness is assumed to be dominating for a displacement controlled scenario. This is due to the fact that equilibrium is obtained by displacements leading to a change of geometry.

However, this phenomenon is in reality not either pure load- or pure displacement-controlled, but there will be a certain combination. Hence, both formulas corresponding to the different conditions (i.e. Equation 6.7 and 6.8) could be checked for the present analysis on titanium.

The two interaction formulas are:

Load-controlled:

$$\left(\frac{\gamma_F \gamma_C M_{F,c} + \gamma_E M_{E,c}}{\frac{M_c}{\gamma_R}} \right)^2 + \left(\frac{p_e}{\frac{p_c}{\gamma_R}} \right)^2 \leq 1 \qquad (6.7)$$

Displacement-controlled:

$$\left(\frac{\gamma_F \gamma_C \varepsilon_{F,c} + \gamma_E \varepsilon_{E,c}}{\frac{\varepsilon_{M,c}}{\gamma_\varepsilon}} \right)^{0.8} + \frac{p_e}{\frac{p_c}{\gamma_R}} \leq 1 \qquad (6.8)$$

where

$M_{F,c}$: characteristic functional bending moment.

$M_{E,c}$: characteristic environmental bending moment.

M_c : characteristic limit bending moment, see (II).

γ_F : functional Load Factor.

γ_E : environmental Load Factor.

γ_C : condition Load Factor.

γ_R : strength Resistance Factor.

p_e : characteristic external over-pressure.

p_c : characteristic collapse pressure, see (I) ($p_c = \infty$ if $p_i > p_e$).

$\varepsilon_{F,c}$: characteristic functional longitudinal strain.

$\varepsilon_{E,c}$: characteristic environmental longitudinal strain.

$\varepsilon_{M,c}$: characteristic buckling strain capacity, see (III).

γ_ε : strain capacity Resistance Factor.

(I): The characteristic capacity for external pressure (collapse) is to be calculated as:

$$(p_c - p_{el})(p_c^2 - p_p^2) = p_c p_{el} p_p f_0 \frac{D}{t} \qquad (6.9)$$

where

$p_{el} = 2\ E\ (t/D)^3 / (1-\nu^2)$

$p_p = 2\ SMYS\ t/D$

$f_0 = (D_{max}-D_{min}) / D > 0.005 = 0.5\ \%$.

(II): The moment capacity is to be calculated as:

$$M_c = M_p\ f_M,\ 15 < D/t < 45.$$

where $M_p = SMYS\ D^2t$.

$$f_M = k_1 \cos\frac{\left[\frac{\pi}{2}\left(k_2 - \frac{1}{2}\frac{\gamma_F \sigma_h}{SMYS}\right)\right]}{k_1} \text{ for } \sigma_h > 0 \tag{6.10}$$

$$f_M = \cos\left[\frac{\pi}{2} k_2\right] \text{ for } \sigma_h < 0 \tag{6.11}$$

$$k_1 = \sqrt{1 - \frac{3}{4}\left(\frac{\gamma_F \sigma_h}{SMYS}\right)^2} \tag{6.12}$$

$$k_2 = \frac{\gamma_F N_{F,c} + \gamma_E N_{E,c}}{\pi\, SMYS\, D\, t} \tag{6.13}$$

$N_{F,c}$ = characteristic functional axial pipe wall force.
$N_{E,c}$ = characteristic environmental axial pipe wall force.

(III): The characteristic strain capacity reflects the strain at the maximum capacity and is to be calculated as:

$15 < D/t < 45$, $\sigma_h > 0$:

$$\varepsilon_{M,c} = \left(\frac{t}{D} - 0.01 + 5\frac{\sigma_H}{E}\right)\alpha_{gw} \tag{6.14}$$

$15 < D/t < 45$, $\sigma_h < 0$:

$$\varepsilon_{M,c} = \left(\frac{t}{D} - 0.01\right)\alpha_{gw} \tag{6.15}$$

where E is Young's modulus and α_{gw} is a girth weld reduction factor.

One of the main differences between the formulas in Dnv (1996) (Equation 6.7) and Murphey & Langner (1985) (Equation 6.1) is that the former formula squares the contributions from both bending and external pressure. Hence, for a given level of bending, the external pressure that is predicted to cause buckling/collapse of the cross-section is at a higher level than for the formula suggested by Murphey & Langner (1985). The same applies for the bending moment at a given level of the external pressure. The formula proposed by Murphey & Langner (1985) is, thus, the more conservative.

6.3 GRAPHICAL REPRESENTATION OF MECHANICAL LIMIT STATES

In this section, equations related to three of the main limit states for sizing of wall thickness of pipes are summarised and given in Figures 6.1 and 6.2. This comprises design checks as follows:

- Pressure containment
- Yielding
- Local buckling / collapse

A graphical comparison between them is presented to identify the relation between the buckling formulas and the yielding / pressure containment limit states. Furthermore, the difference between the two buckling formulas given by Murphey & Langner (1985) and DnV (1996) are shown in Figures 6.1 and 6.2 for different combinations of bending and external pressure (pressure containment is called hoop in Figures 6.1 and 6.2). The formulas and assumptions that form the basis for the diagrams are described in Sections 6.3.1-6.3.3.

6.3.1 Pressure Containment

The stress in a thin-walled pipe subjected to internal pressure only, DnV (1996), can be written as:

$$\sigma_H = \Delta p \frac{D-t}{2t} \tag{6.16}$$

Dividing both sides by σ_Y of the equations gives the following relation:

$$\frac{\sigma_H}{\sigma_Y} = \frac{\Delta p}{\sigma_Y}\frac{D-t}{2t} = \beta\frac{D-t}{2t} \tag{6.17}$$

where $\beta = \Delta p / \sigma_Y$ (pressure difference / SMYS).

This expression corresponds to a horizontal line parallel to the horizontal axis for a given D/t-ratio. The distance from the axis to this line is determined by the ratio β. The maximum permissible distance is given by the usage factor that is employed for the design check. The parameter on the horizontal axis is non-dimensional, i.e. taken as the longitudinal stress divided by the yield strength. It is denoted α, where $\alpha = \sigma_L / \sigma_Y$. Equation (6.17) is independent of the longitudinal stress, since the stress is checked for pressure difference only.

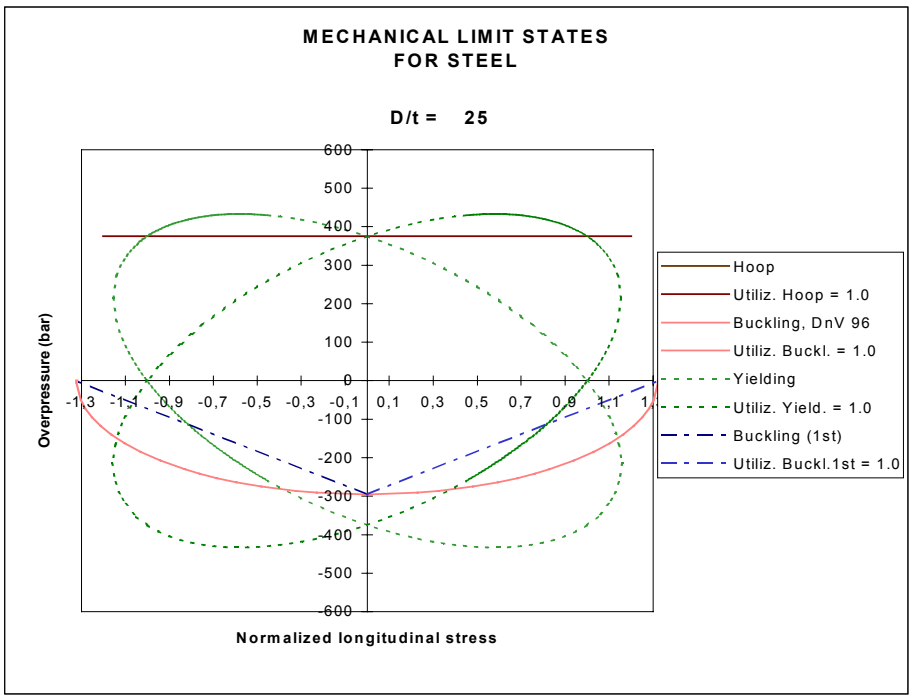

Figure 6.1 Mechanical limit states for a typical steel material.

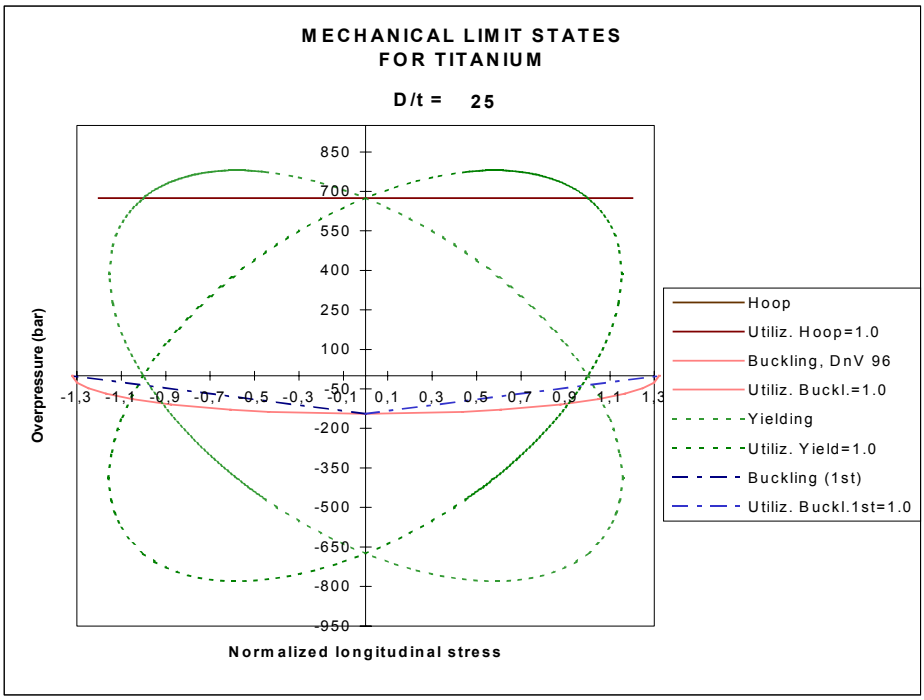

Figure 6.2 Mechanical limit states for titanium based on steel formula.

An important issue in this context is the interaction between the yield strength and the ultimate tensile strength. For materials with low ductility, only a certain fraction of the ultimate tensile strength can be utilised. If this fraction corresponds to a stress level that is smaller than the yield stress, the former replaces the specified minimum yield stress (SMYS) in the pressure containment stress design check. The fraction is obtained by considering X65 steel as a reference material, for which the ratio between the tensile strength (SMTS) and the specified minimum yield stress is 1.17. The permissible fraction is then equal to the inverse of this value. If the same approach is applied for titanium, the stress to be employed in the pressure containment (and yielding) stress check is somewhat smaller than the yield stress (the fraction is about 1.10).

6.3.2 Yielding

The equivalent von-Mises stress is employed as a basis for this stress check. Neglecting the radial stress, a two-dimensional stress formulation is obtained. The formula reads

$$\sigma_{VM} = \sqrt{\sigma_L^2 + \sigma_H^2 - \sigma_L \sigma_H} \tag{6.18}$$

where σ_L and σ_H are longitudinal and hoop stresses, respectively. This formulation will be sufficiently accurate except for thick-walled tubes with D/t ratios of 10 or smaller.

Normalising the equation with respect to the specified minimum yield stress after squaring the equation, and introducing γ as the utilisation ratio (i.e. σ_{VM} / σ_Y), the following equation appears.

$$\left(\frac{\sigma_H}{\sigma_Y}\right)^2 - \frac{\sigma_1}{\sigma_Y}\frac{\sigma_2}{\sigma_Y} + \left(\left(\frac{\sigma_1}{\sigma_Y}\right)^2 - \gamma^2\right) = 0 \tag{6.19}$$

This will correspond to an ellipsis in the two-dimensional stress plane. However, since the bending stresses are antimetric around the neutral axis (in elastic condition) two points around the circumference that are diametrically opposite need to be considered. Accordingly, two different ellipses are obtained which are mirror images of each other with respect to the hoop stress axis.

It is to be noted the radial stress in the two-dimensional equation (Equation 6.18) is neglected. However, this radial stress may influence the von-Mises stress at high pressure levels. This implies that the intersection between the vertical axis and the ellipses in Figures 6.1 and 6.2 is moved at a slightly lower value of the pressure level.

6.3.3 Local Buckling and Collapse

Two of the buckling formulas in Section 6.2 are considered: The linear (Equation 6.1) and the quadratic formula from DnV (1996) (Equation 6.7). The factor $1/\gamma_R$ is to be interpreted as the usage factor. The value is given in the diagrams.

Based on the same normalisation as before, the bounding curve in the stress diagram for this limit state will also be an ellipse. However, only the part located in the lower half plane is relevant, since the equation only applies to pipes with *external* over-pressure.

6.3.4 Graphical Classification and 'Generic' Design Scenario

Based on Equations (6.7, 6.17 and 6.19) that are relevant for the three specified design checks, a diagram of the type shown in Figure 6.1 will result. This diagram is based on a titanium pipe with a D/t ratio equal to 25. There are two buckling curves, as indicated in the legend box of the diagrams. 'Buckling DnV98' and 'Buckling 1st' correspond to formula given in DnV (1996) and by Murphey & Langner (1985), respectively. A useful comparison is provided by Figure 6.2 that applies to a steel pipe with the same D/t ratio. It is seen that for pure elastic overpressure (i.e. negative values on the vertical axis), the maximum pressure with respect to the bucking formulas is 30 MPa (300 bar). The maximum pressure with respect to yielding is approximately 36.5 MPa. This implies a ratio between the maximum external pressure based on buckling and yielding limit states is equal to 82 %. The same ratio for titanium is 23 %. Clearly, the local buckling/collapse limit state is much more critical for titanium than for steel for this D/t ratio.

6.4 COMPARISON OF COMPUTED CAPACITY AND DESIGN CODE LIMIT VALUES FOR STEEL AND TITANIUM

To compare the finite element model used in the present calculations against existing codes, analyses with the FE-model for steel are performed, based on the material parameters given in Table 6.1, Bai et al. (1994). The material model by Tvergaard (1976) fits the material curve for steel X65 very well.

Table 6.1. Characteristic material parameters for Steel X65.

Yield strength, σ_Y (MPa)	Yield strain, ε_Y	Ultimate strength, σ_u (MPa)	Ultimate strain, ε_u
450	0.02	530	0.2

The same finite element model as given in Chapter 4 is used. The results are given in Table 6.2.

Table 6.2. Critical pressure and bending moment for steel.

Mean diam./ thickness	Critical pressure, P_c (MPa)			Critical bending moment, M_c (kNm)		
	Computed	DnV'96	Difference	Computed	DnV'96	Difference
20	36.7	35.4	2.3 %	3786	3787	0.0 %
23	27.7	26.9	3.0 %	3228	3193	1.1 %
26	20.7	20.0	3.5 %	2792	2749	1.6 %
30	14.4	13.7	5.1 %	2356	2322	1.5 %

Difference is to be interpreted as the difference relative to DnV'96-values.

DnV (1996) is in good agreement with the FE-results of the critical bending moment (maximum deviation is up to 1.6 %). The maximum deviation is 5.1 % for the critical external pressure. The systematic over-prediction by the FEM-model for the critical external pressure can be given certain plausibility. This is due to the fact that the formula for the critical external pressure is based on an elastic perfectly plastic material, while the characteristic parameters for steel X65 given in Table 6.1 includes strain hardening. This implies that computed levels for the critical external pressure is higher than the ones predicted by DnV (1996).

No strain hardening is accounted for in the critical bending moment capacity given by DnV (1996). Furthermore, the specific formula assumes that the geometry of the cross-section remains (i.e. no ovality occurs). In the FEM-calculations strain hardening is accounted for, as given in Table 6.1. Hence, this effect tends to increase the bending moment capacity. However, the nodes in the FE-model deform when subjected to a bending moment, leading to a certain cross-sectional ovality. Implicitly, the bending moment capacity is decreased by this geometric effect. These two 'computing' effects (i.e. strain hardening and corss-sectional ovality) seem to contribute with the same magnitude, since the difference between the computed and the DnV (1996) critical bending moment is approximately 1 %.

Table 6.3 gives the critical external pressure and the critical bending moment values for the same set of D/t-ratios as for steel (Table 6.2).

Table 6.3. Critical pressure and bending moment for titanium.

Mean diam./ thickness	Critical pressure, p_c (MPa)			Critical bending moment, M_c (kNm)		
	Computed	DnV'96	Difference	Computed	DnV'96	Difference
20	30.9	26.6	16.2 %	6498	6995	-7.5 %
23	20.8	18.0	15.6 %	5468	5898	-7.3 %
26	14.5	12.7	14.2 %	4684	5079	-7.7 %
30	9.57	8.41	13.8 %	3954	4289	-7.8 %

The critical external pressure and the critical bending moment for titanium are not well predicted by the formula given in DnV (1996). Average deviations equal to + 15 % and – 7.5 % are observed for the critical external pressure and the critical bending moment, respectively. Hence, it seems that DnV (1996) is not adequate for this titanium alloy since the deviation is almost the same for all D/t-ratios for both the critical external pressure (from + 14 % to + 16 %) and for the critical bending moment (from – 7 % to -8%).

The basic explanation for the limit of the critical bending moment based on DnV'96 as compared to predictions from the finite element model, is the difference in Young's modulus between titanium and for which DnV (1996) is based on. The Young's modulus for the particular titanium alloy used for the numerical calculations is only 57 % compared to that for steel. This implies a greater ovalisation for the titanium alloy when the bending moment is applied, and implicitly less bending moment capacity.

The difference between the critical external pressure given in DnV (1996) and estimated for the numerical model can be caused by the different elastic strain limit for steel and titanium. For steel, the elastic limit is $\varepsilon_S = \sigma_Y / E = 0.22\%$, while the same number for titanium is $\varepsilon_T = \sigma_Y / E = 0.71\%$. This means that steel will develop plastic strains at a lower load level than titanium. This can be seen from Figure 6.3, where the plastic strain for uniaxial tension is compared for steel and titanium.

Steel develops plastic strain at a level of 70 % of the critical external pressure. For titanium, the same level is about 90 %.

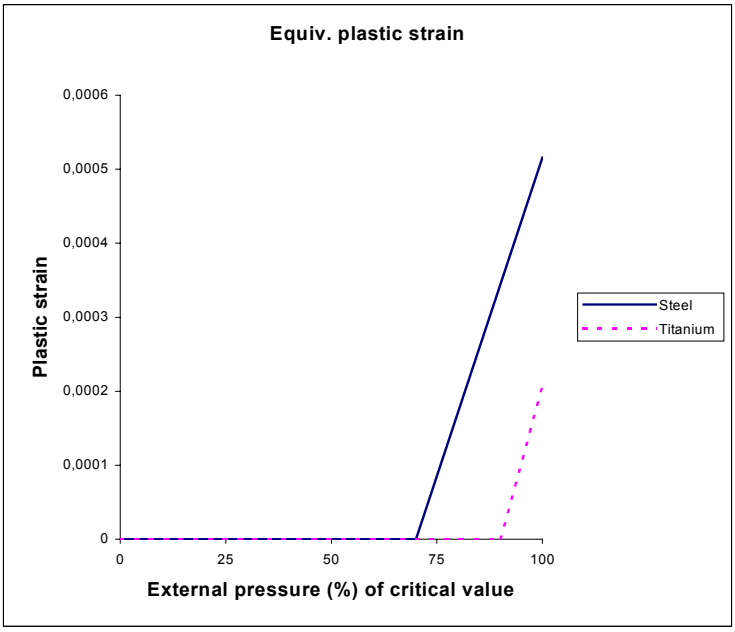

Figure 6.3 Plastic strain for steel and titanium.

6.5 BASIS FOR POSSIBLE DESIGN FORMULA FOR CRITICAL EXTERNAL PRESSURE FOR TITANIUM

Finite element computations are performed to establish the dependency of the critical external pressure on the initial ovality, the Young's modulus, the D/t-ratio and the yield stress. The Least-square-method (LSM) is used to establish analytical expressions that fit the FEM- results for relevant parameters. The different analytical expressions are then used to identify a formula for both the critical external pressure and the critical bending moment (Section 6.6).

Initial ovality

The initial ovality parameter is varied from 0.5 % up to 2.5 %. The corresponding variation in critical external pressure can be fitted to a parabola as shown in Figure 6.4. The variation range relative to the corresponding value for mean initial ovality (equal to 1.5 %) is between – 6.7 % to + 8.2 %.

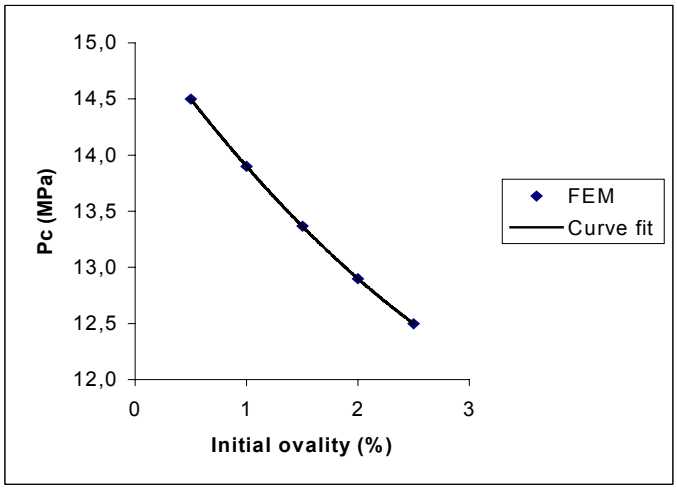

Figure 6.4 Critical external pressure as a function of initial ovality.

Young's modulus

Values for the Young's modulus are varied within the range observed from the laboratory tests, described in Chapter 3. The results and the corresponding curve fit are given in Figure 6.5, which indicates that the critical external pressure varies linearly as a function of the Young's modulus. The variation range relative to the corresponding value for mean Young's modulus (116937 MPa) is between – 11.0 % to + 15.2 %.

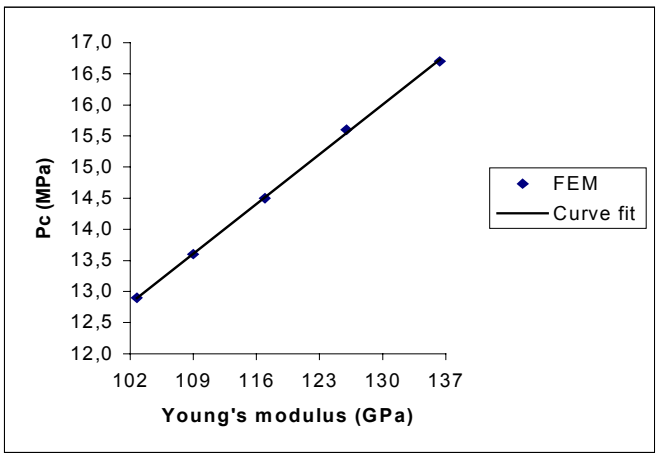

Figure 6.5 Critical external pressure as a function of Young's modulus.

D/t-ratio

The D/t-ratio range is from 20 up to 30. The same tendency is observed for the D/t-ratio as for the initial ovality, i.e. the critical external pressure is well fitted by a second degree polynomial function as shown in Figure 6.6. The variation range relative to the corresponding value for mean D/t (equal to 26) is between – 32 % to + 115 %.

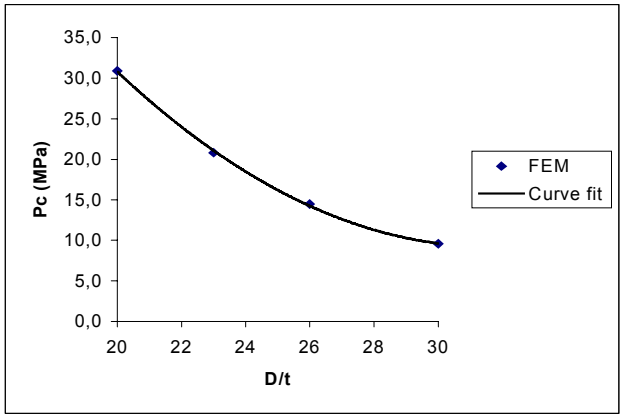

Figure 6.6 Critical external pressure as a function of D/t-ratio.

Yield stress

The yield stress range identified from the laboratory tests described in Chapter 3, is approximately ± 3 % about the mean yield stress (equal to 831.3 MPa). The corresponding variation in critical external pressure for the present titanium alloy is only ± 0.2 % and fits a straight line as shown in Figure 6.7.

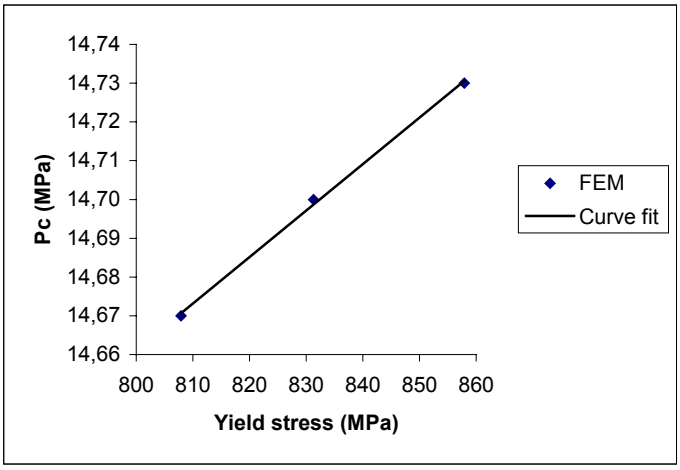

Figure 6.7 Critical external pressure as a function of yield stress.

A suggested functional relationship for the critical external pressure for this particular titanium grade can be obtained on the basis of the calculations performed in this Section. It is clearly seen from Section 6.5 that the parameters entering the functional relationship are likely to be:

$$p_c = f\left(E, \left(\frac{D}{t}\right)^2, f_0^2, \frac{\sigma_Y}{\sigma_{ref}}\right) \tag{6.20}$$

where

D/t	: Mean diameter over nominal wall thickness
E	: Young's modulus (MPa)
f_0	: Initial ovality, see Equation (6.5).
σ_Y/σ_{ref}	: Yield stress divided by a reference yield stress (831.3 MPa).

The least-square-method (LSM) for the fitted curves in Figures 6.4-6.7 leads to the following formula for the critical external pressure for the specific titanium alloy used herein:

$$p_c = k_P \cdot E \cdot \left(\frac{\sigma_Y}{\sigma_{ref}}\right)^{1/15} \cdot \left(k_1 \cdot \left(\frac{D}{t}\right)^2 + k_2 \cdot \frac{D}{t} + k_3\right) \cdot \left(k_4 \cdot f_0^2 + k_5 \cdot f_0 + k_6\right) \tag{6.21}$$

where

$k_p, k_1,\ldots,k_6$	: Constants obtained by LSM, see Table 6.4.

Table 6.4. The constants determined from LSM for estimation by Equation (6.21).

k_0	k_1	k_2	k_3	k_4	k_5	k_6
5.9819E-7	0.1604	-10.134	169.35	0.1314	-1.3943	15.164

The maximum observed deviations for all cases between Equation (6.21) and finite element simulations vary from -1.2 % up to 2.9 %. Thus, Equation (6.21) represents a suitable expression for the critical external pressure for the titanium grade 24.

It is to be noted that the critical external pressure does not strongly depend on the yield strength. Hence, there is reason to believe that elastic buckling of the cross-section tends to occur due to the relatively low Young's modulus. This is furthermore supported by Equations (4.5-4.7) in Section 4.6.

6.6 BASIS FOR POSSIBLE DESIGN FORMULA FOR CRITICAL BENDING MOMENT FOR TITANIUM

Similarly as described for the critical external pressure in Section 6.5, numerical simulations are used to establish the dependency of the critical bending moment on the initial ovality, the Young's modulus, the D/t-ratio and the yield stress.

Initial ovality

The critical bending moment varies linearly as a function of the initial ovality as shown in Figure 6.8. The variation range is between – 0.60 % to + 0.34 % relative to mean initial ovality (equal to 1.5 %).

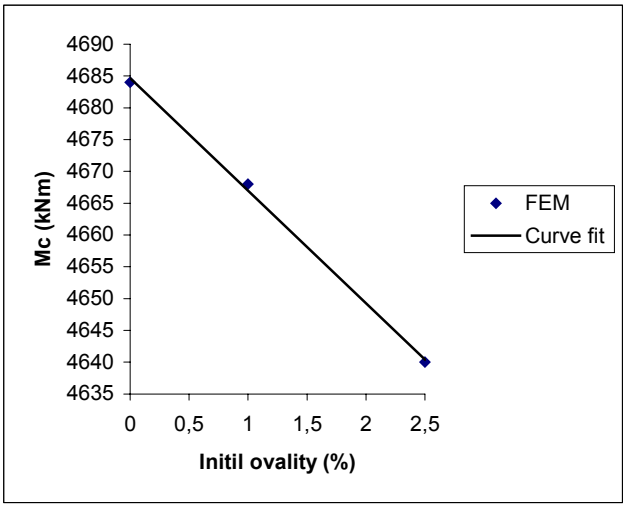

Figure 6.8 Critical bending moment as a function of initial ovality.

Young's modulus

The same range of values as for the critical external pressure is used for this parameter. The results are given in Figure 6.9, where also a 2nd degree polynomial curve fit is shown. The variation range relative to the mean value of the Young's modulus is between – 1.3 % to + 1.3 %.

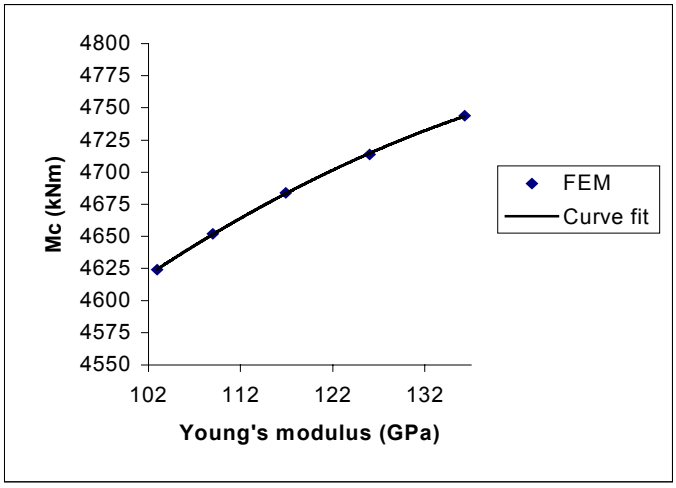

Figure 6.9 Critical bending moment as a function of Young's modulus.

D/t-ratio

The same D/t-ratio applies for the critical bending moment as for the critical external pressure. The same tendency appears, i.e. the critical bending moment is very well fitted to a 2nd degree polynomial function as given in Figure 6.10. The variation range relative to mean D/t-ratio (equal to 26) is between – 16 % to + 38 %.

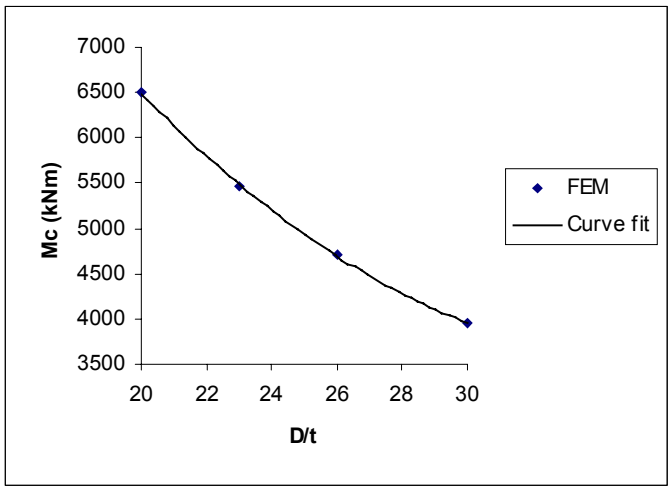

Figure 6.10 Critical bending moment as a function of D/t-ratio.

Yield stress

The critical bending moment is a linear function of the yield stress, see Figure 6.11. The variation range considered here is between – 2.1 % to + 2.1 % relative to the mean value of the yield stress (equal to 831.3 MPa).

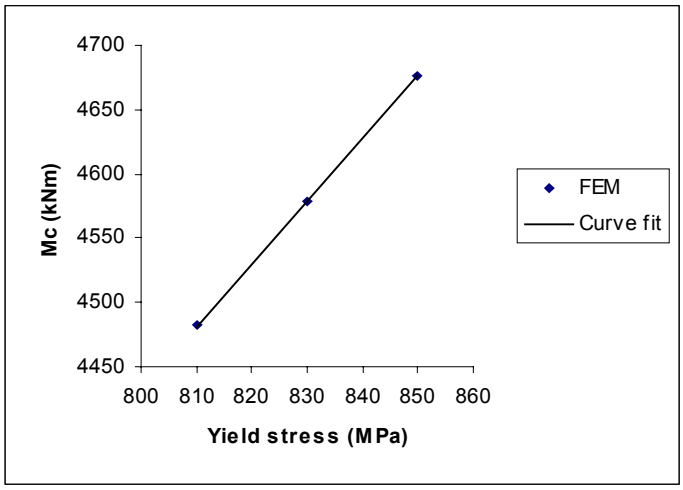

Figure 6.11 Critical bending moment as a function of the yield stress.

A suggested functional relationship for the critical bending moment for this particular titanium grade can be obtained on the basis of the calculations performed in this Section. Based on the calculations in previous Sections, the formula will appear like:

$$M_c = f\left(E^2, \left(\frac{D}{t}\right)^2, f_0, \frac{\sigma_Y}{\sigma_{ref}}\right) \tag{6.22}$$

where

D/t	: Mean diameter over nominal wall thickness.
E	: Young's modulus (MPa).
f_0	: Initial ovality.
σ_Y	: Yield stress (MPa).

The least-square-method (LSM) on the fitted curves in Figures 6.8-6.11 leads to the following formula for the critical external pressure for the specific titanium alloy used herein:

$$M_c = k_M \cdot (1 - f_0) \cdot {\sigma_Y}^{7/8} \cdot \left(k_7 \cdot \left(\frac{D}{t}\right)^2 + k_8 \cdot \frac{D}{t} + k_9\right) \cdot \left(k_{10} \cdot E^2 + k_{11} \cdot E + k_{12}\right) \tag{6.23}$$

where

k_M, k_7,…,k_{12} : Constants obtained by LSM, see Table 6.5.

Table 6.5. The constants determined from LSM for estimation by Equation (6.23).

k_M	k_7	k_8	k_9	k_{10}	k_{11}	k_{12}
6.0235E-7	11.71	-838.87	18585	-.0336E-6	11.623E-3	3784.3

The maximum observed deviations between Equation (6.23) and the FEM-results are varying from – 1.6 % up to + 2.1 %. Hence, the critical bending moment for the titanium grade 24 from the laboratory tests is well represented by the fitted formula given in Equation (6.23).

6.7 MAXIMUM BENDING MOMENT CAPACITY AS A FUNCTION OF EXTERNAL PRESSURE LEVEL

The following calculations are based on the load-controlled scenario. Table 6.6 gives maximum bending moment capacity for selected combinations of D/t and external pressure. A graphical representation of Table 6.6 is given in Figure 6.11. The ratio p_e/p_c is calculated according to Section 6.4.2. The range for p_e/p_c is varying from 0.5 up to 0.8, which is considered most relevant for deep water applications. It is emphasised that the calculations represent a force-controlled system, which is reflected in the choice of corresponding formula in DnV (1996).

Table 6.6. FE-estimates of the maximum bending moment capacity (kNm) of a titanium pipe as a function of p_e/p_c and D/t.

D/t	**External pressure / critical pressure (p_e/p_c)**			
	0.5	**0.6**	**0.7**	**0.8**
20	5964	5756	5408	4898
23	5018	4828	4554	4120
26	4262	4098	3850	3462
30	3546	3396	3156	2820

For a graphical view, the values are plotted in Figure 6.12.

It is clearly seen that the maximum bending moment capacity decreases as a parabolic function for increasing external pressure. The decrease in the predicted bending capacity is for all D/t-ratios from the lowest up to the highest value of p_e/p_c, approximately 20 %.

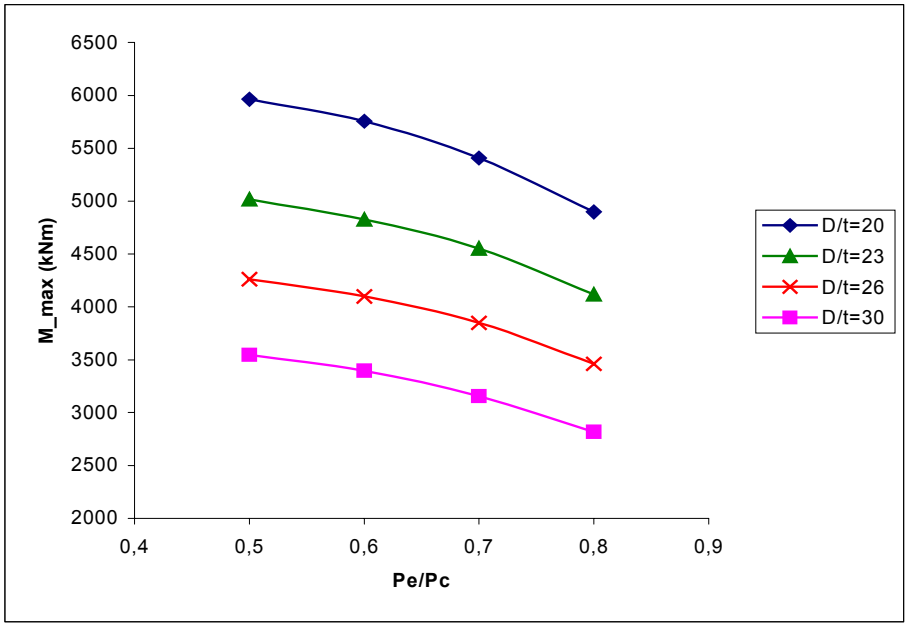

Figure 6.12 Graphical representation of the maximum bending moment capacity for various p_e/p_c-ratios.

The normalised estimated maximum bending moment capacity values with respect to the critical bending moment for the corresponding D/t-ratios relevant for Section 6.4.2, is given in Table 6.7.

Table 6.7. Finite element estimates of normalised maximum bending moments with the corresponding critical bending moment.

p_e/p_c	D/t=20	D/t=23	D/t=26	D/t=30
0.5	0.918	0.918	0.906	0.897
0.6	0.886	0.883	0.871	0.859
0.7	0.832	0.833	0.818	0.798
0.8	0.754	0.753	0.736	0.713

As seen from Table 6.7 the maximum bending moment for p_e/p_c equal to 0.5 is about 90 % for all D/t-ratios of the bending moment capacity. This value decreases to about 87 %, 81 % and 73 % for p_e/p_c equal to 0.6, 0.7 and 0.8, respectively. This is indicated in Figure 6.13 by the curve called 'FEM'. The curve called 'DnV96' in Figure 4.13 is based on the same numerical results for the maximum bending moment capacity as curve 'FEM', but is normalised with p_c and M_c obtained from DnV'96. It is clearly seen that these two curves differ significantly.

The formula given in DnV (1996) seems to under-estimate the critical external pressure by about 15 %. Hence, for no external bending moment, the value of the p_e/p_c-coordinate is 15 % greater for the FEM-results. The opposite tendency applies to the maximum bending moment for no external pressure. The predicted maximum bending moment capacity based on DnV'96 is about 7 % greater than for the FEM-results.

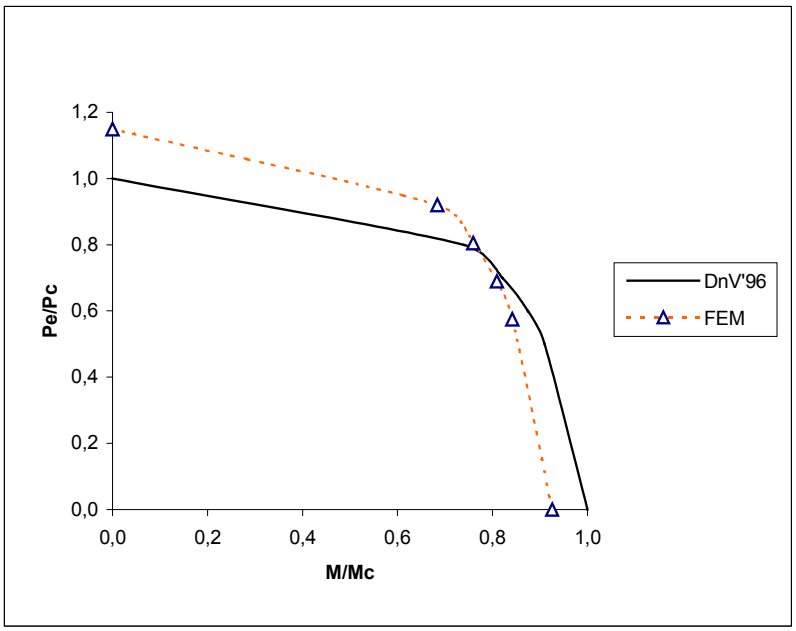

Figure 6.13 Capacity diagram for combined normalised values of bending moment and external pressure.

Figure 6.13 indicates graphically that the two 'end coordinates' for the interaction formula from DnV (1996) (Equation 6.7) can not directly applicable to titanium. Another relevant comparison is the shape of the interaction formula, by the use of the critical external pressure and the critical bending moment calculated from the FEM-analyses. The interaction formula for steel in DnV'96 is drawn in Figure 6.14, and indicates that the interaction formula under-estimates the capacity for titanium. The interaction formula from DnV'96 is drawn for different p_e/p_c-ratios implying that the

corresponding M/M_c-values equal to $\sqrt{1-\left(p_e/p_c\right)^2}$. For the specific coordinates given in the diagram, the reduction in the p_e/p_c-ratio for a given M/M_c-value is from 19 % to 24 %.

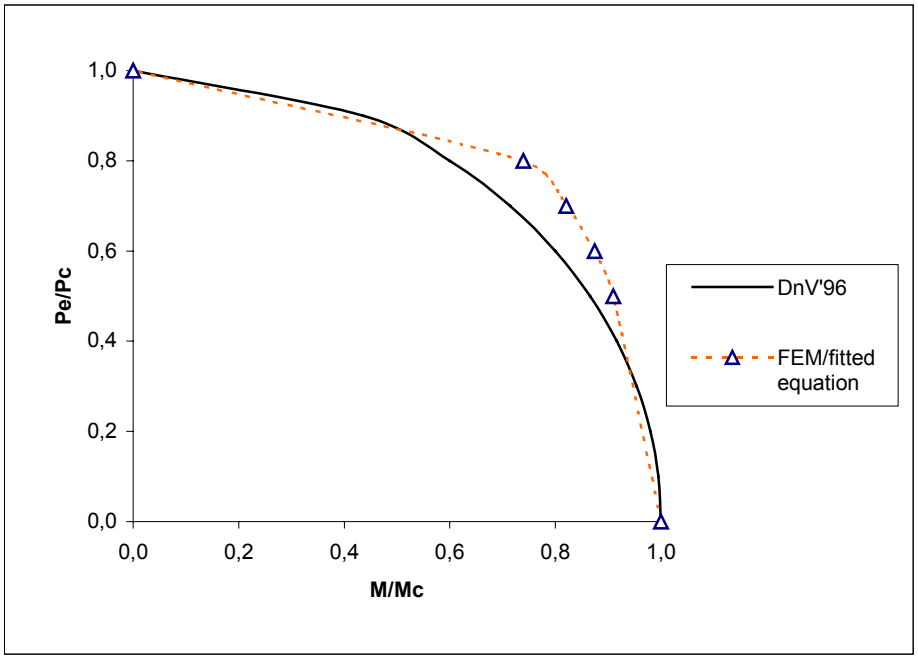

Figure 6.14 Interaction formula in DnV'96 compared to titanium FEM-results.

A modified interaction formula for titanium is suggested. It is based on FEM-results, by the use of 'least-square-method', and is given by:

$$\left(\frac{M}{M_c}\right)^{3.65}+\left(\frac{p_e}{p_c}\right)^{1.83}=1.0 \tag{6.24}$$

The modified interaction formula is given graphically in Figure 6.15.

As can be seen from this figure, the FE-results fit the interaction curve well.

Based on the calculations in Sections 6.5-6.7, the suggested formulas for the critical bending moment, critical external pressure and the interaction formula are valid for the ranges of input parameters as described herein. Specifically, this means for the actual titanium grade 24 and the corresponding material properties (Young's modulus, yield strength), D/t-ratio ranging from 20 up to 30, initial ovality up to 2.5 % (according to definition in DnV (1996)). Hence, extrapolation should be performed with care.

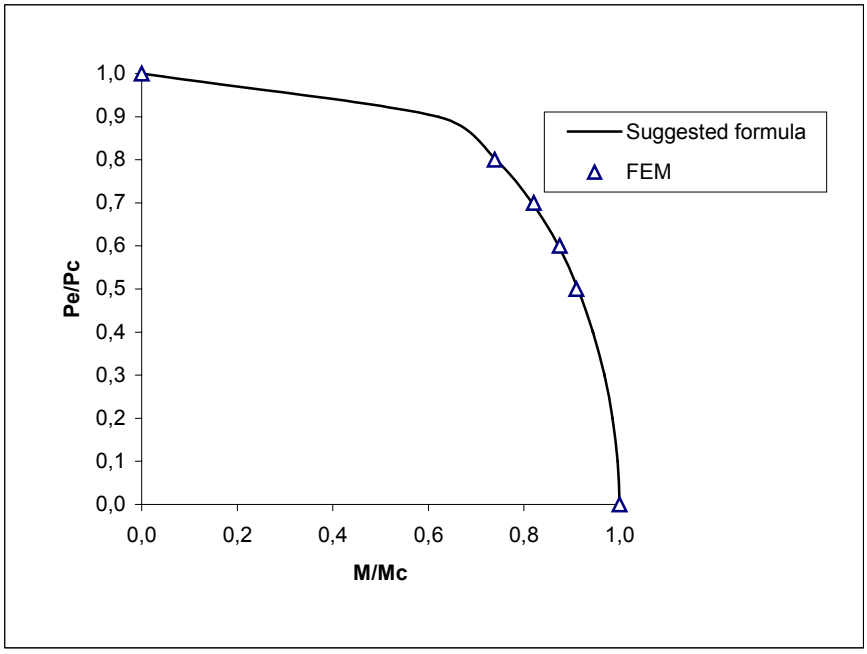

Figure 6.15 Suggested interaction formula for titanium.

As described in Section 4.6, test data for titanium grade 29 pipes were compared with finite element simulations. The suggested interaction formula, which originally was developed for titanium grade 24 can thus be checked for fit to grade 29.

6.8 FIT OF THE SUGGESTED INTERACTION FORMULA TO TITANIUM GRADE 29

By the use of the laboratory data from bending and collapse tests reported in Section 4.6, the suggested interaction formula given in Equation (6.24) is checked for this titanium grade. Finite element analyses and laboratory tests for titanium grade 29, are plotted in a similar diagram as Figure 6.15 to see if this suggested interaction formula is representative for a different titanium alloy.

The finite element analyses are called 'FEM' in the figure, and are represented by the squares. The tests from the laboratory ('LAB') are represented by the triangles, and are based on the M_c and P_c values from the FEM-analyses. The uppermost triangle represents Test 1 in Table 4.10. The second uppermost triangle represents Test 2, and triangle number 3, 4, 5 and 6 from the uppermost one, correspond to tests number 3, 4, 5 and 6. The continuous line represent Equation (6.24).

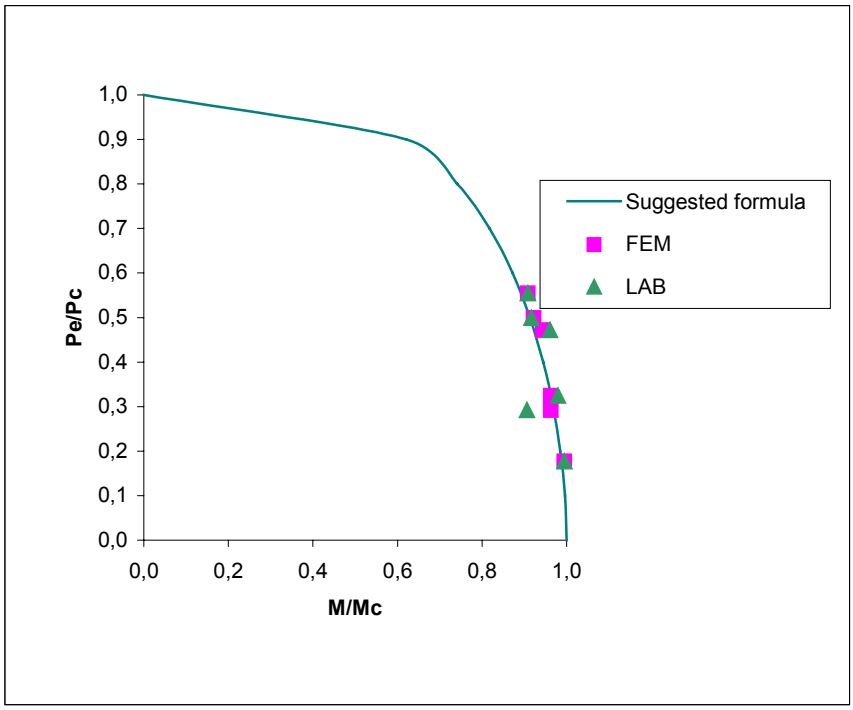

Figure 6.16 The modified interaction formula with data for titanium grade 29.

It is seen that the results based on finite element analyses for titanium grade 29 fit the interaction formula that is suggested in Equation (6.24) very well. Thus, the interaction formula that initially is suggested on the basis of analyses for titanium grade 24, seems to represent the interaction of external pressure and bending moment very well for the additional alloy based on finite element results.

C h a p t e r 7

CONCLUSIVE REMARKS AND RECOMMENDATIONS FOR FURTHER WORK

"An expert is a man who has made all the mistakes, which can be made, in a very narrow field."
Nils H. D. Bohr (1885-1962).

7.1 SUMMARY AND CONCLUSIONS

The present study has addressed the use of titanium risers for floating production platforms in large water depths. Focus has been on the capacity of the riser subjected to combined external pressure and bending relevant for the lower part of the riser.

The loading and deformations of a riser (supported from a TLP) in the sag-bend region are established from a global riser analysis. Pipe capacity estimates with respect to maximum bending moment under constant external pressure conditions are computed with a finite element shell model with possible large geometrical deformation and elasto-plastic material behaviour. Computed capacity based on the shell model is compared with full scale tests.

Statistical measures of the bending capacity are established as a function of the major uncertain capacity parameters associated with material properties, geometrical imperfections and orientation of the bending plane relative to the geometrical imperfections.

Reliability methods are applied to establish statistical measures of the pipe capacity as function of the variability in the capacity parameters. The parameter variability is established from laboratory measurements.

Applicability to titanium of commonly used design check formulas for steel pipes is studied, and a possible capacity formula is proposed based on the numerical simulations for titanium pipes subjected to bending an external pressure.

The following conclusions can be made on the basis of the present study:

Titanium material tests

- The material behaviour for the present titanium pipe material can be modelled as isotropic. An-isotropic effects are very small according to the present test data.

- The strain hardening is low. The ultimate stress is about 10 % greater than the yielding stress.

- The Voce material model represents the material behaviour very well.

- Large variations in the ductility are observed. The fracture strain is observed to vary from 3 % up to 12 %.

- The number of available test specimens is not sufficient to establish accurate statistical models for the material parameters in particular in the outer range relative to the mean values. It is hence emphasised that the present tests will not give information about the variation in material properties for the specified grade and manufacturing process for an arbitrary batch of pipes.

Variation in geometry of a pipe cross section

- The wall thickness measured at the pipe ends varies from – 5.4 % to + 21.8 % relative to the nominal value for the titanium pipe tested in the laboratory. This variation is due to the manufacturing process. If the centre of the pipe and the centre of the rotating piercer are perfectly coincident during the extrusion process, the pipe wall thickness should be constant at any cross section. If such an ideal production process has not been achieved, the wall thickness is likely to vary approximately as a harmonic function.

Influence from parameter variability on sag bend pipe capacity

- The maximum bending moment in the sag-bend region (for the considered loading condition) varies linearly as a function of the yield stress and the initial ovality. For the Young's modulus and the wall thickness, polynomial functions of order 2 and 3 respectively, fit the variation of the bending moment capacity. The variation due to the piercer eccentricity and the cross-sectional orientation can also be represented by polynomial functions of order 2 and 3 respectively.

- There is an interaction effect between the piercer eccentricity and the cross-sectional orientation on the maximum bending moment capacity. The effects of wall thickness and Young's modulus are uncorrelated with the capacity effect from the other random variables.

- A normal range of variation of initial ovality and yield stress according to the present material tests have relatively small effects on bending moment capacity in the sag-bend region. The capacity effect is only ± 3 - 4 %. By changing the other parameters from their respective low to high values, the maximum bending moment capacity varies from – 20 % up to + 47 % for the parameters with the largest influence. The variation in the Young's modulus leads to a variation in maximum bending moment capacity between – 14 % and + 11 %. The total ranges of variation in capacity due to the piercer eccentricity and cross-sectional orientation are 17 % and 23 %, respectively.

Comparison of computed capacity estimates with full scale pipe tests

The comparisons between simulations and test results indicate that the finite element shell model provides reliable estimates of the titanium pipe capacity even if no precise measures of accuracy can be deduced due to lack of detailed information about all the parameters associated with the testing.

Statistical measures of bending moment capacity

- From the statistical analyses it is observed that the variation in maximum bending moment capacity for deep water titanium risers in the sag-bend region will fit a normal distribution for the selected uncertain parameters and range of variation. However, a log-normal distribution fits the data almost equally well.

- The uniform wall thickness and the Young's modulus play a dominating role for the maximum bending moment capacity in the sag-bend region. However, for low bending moment capacities, the influence from initial ovality may also be

considerable. In particular, for the range of high C.o.V. values (according to Table 5.14) the importance factor from the initial ovality is about 80 % for extremely high utilisation of the capacity to withstand external pressure and thus low bending moment capacities.

Basis for design check formulas of titanium pipes subjected to bending and external pressure

- The ratio between the possible maximum external pressure at collapse and at a yield limit state differs significantly between steel and titanium based on formulas given in commonly employed design codes. This ratio is 82 % for steel, and only 23% for titanium. Clearly, the collapse limit state is much more critical for titanium.

- The levels of critical external pressure and critical bending moment for a titanium pipe are not very well predicted by DnV (1996). There seems to be a typical difference of + 15 % and – 7.5 % between corresponding formulas in DnV (1996) and FE-results for the critical external pressure and critical bending moment, respectively.

- A possible capacity design check formula for titanium pipes subjected to bending an external pressure is suggested based on the present numerical simulations.

7.2 RECOMMENDATIONS FOR FURTHER WORK

The topics listed below for further studies are associated with similar riser applications and environmental conditions as the present study to enable more comprehensive conclusions. Extensions to different combinations of loading and possible induced deformations are obvious, but may involve different failure mechanisms and relevant parameters.

- The material testing should be extended to establish more reliable statistical models for the material properties. The tests should then include specimens from different production batches to represent realistic ranges of variability.

- With a more complete knowledge of the material properties and inclusion of uncertainties of induced riser motion and numerical model uncertainties in the statistical analyses, it would be possible to establish a basis for reliability analyses of the specified riser design. Analysis of model uncertainties could include finite element convergence studies or comprehensive comparisons with analytical and other reference solutions and possible series of precise pipe tests.

- Reliability analyses with estimated probabilities of failure would also establish a valuable and required basis for calibration of design formulas.

- Investigate possible differences in collapse behaviour between imposed bending by load or displacement control. Extend to design formulas.

Chapter 8

REFERENCES [4]

ABAQUS (1996): ABAQUS/Standard, User's Manual I and II, Example Problems Manual I and II and Post Manual, version 5.6.

Ades, C. S. (1957): "Bending strength of tubing in the plastic range", Journal of Aeronautical Sciences, vol. 24, pp. 605-610.

API (1998): API RP 2RD, "Design of Riser for Floating Production Systems (FPSs) and Tension Leg Platforms (TLPs)".

Bai, Y., Igland, R. T. and Moan, T. (1994): "Ultimate Limit States of Pipes under Tension and Bending", International Journal of Offshore and Polar Engineering, vol. 4, pp. 312-319.

Baxter, C. F. and Schults, R. W. (1996): "Critical Aspects of Dynamic Titanium Alloys Risers", Proceeding of the Offshore Mechanics and Arctic Engineering Conference.

Benjamin, J. R. and Cornell, C. A. (1970): "Probability, Statistics and Decisions for Civil Engineers", McGraw-Hill, New York.

[4] It is mentioned that the references regarding SINTEF (Division of Structural Engineering) is now a separate division under MARINTEK (in Trondheim, Norway).

Berge, S., Sævik, S., Engseth, A. and Aarnes, R. (1995): "Titanium Risers and Flowlines. Feasibility Studies and Research Activities", Proceeding of the Offshore Mechanics and Arctic Engineering Conference.

Berge, S. (1998): E-mail from Professor Stig Berge, Division of Marine Structures, NTNU, dated 980730.

Bjørset, A. and Leira, B. J. (1996): "TLP with a Catenary Riser", SINTEF-Report no. 6-1 in Titanium Risers and Flowlines JIP (1995-98), Trondheim, Norway.

Bouwkamp, J. G. and Stephen, R. M. (1973): "Large diameter pipe under combined loading", Transportation Journal of the ASCE, vol. 99, pp. 521-536.

Box, G. E. P., Hunter, W. G. and Hunter, J. S. (1978): "Statistics for Experiments", John Wiley and Sons, ISBN 0-471-09315-7.

Boyer, Welsch and Collings (editors) (1994): "Materials properties handbook: Titanium Alloys", American Society of Mechanical Engineers, ASME.

Brazier, L. G. (1927): "On the flexure of thin cylindrical shells and other thin sections", Proceeding Royal Society, A, pp. 104-114.

Breitung, K. (1984): "Asymptotic Approximations for Multinormal integrals", Journal of Engineering Mechanics, ASCE, 110(3), pp.183-190, 357-366.

BS 8010 (1993): "Code of Practice for Pipelines. Part 3. Pipelines subsea: design, construction and installation".

Bucher, C. G. and Bourgund, U. (1990): "A Fast and Efficient Response Surface Approach for Structural Reliability Problems", Structural Safety, vol. 7, pp. 57-66.

Budiansky, B. and Sanders, J. L. (1963): "On the 'Best' First-Order Linear Shell Theory", Progress in Applied Mechanics, The Prager Anniversary Volume, Macmillan, London, pp. 129-140.

Bushnell, D. (1981): "Elastic-plastic bending and buckling of pipes and elbows", Computational Structures, vol 13.

Böhm, F. and Brüchner-Foit, A. (1992): "On Criteria for Accepting a Response Surface Model", Probabilistic Engineering Mechanics, pp. 183-190.

Calladine, C. R. (1983): "Plastic buckling of tubes in pure bending", Proceeding IUTAM Conf. on Collapse, ed. by G. W. Hunt and J. M. T. Thompson, London, UK.

Chen, W. F. and Han, D. J. (1987): "Plasticity for Structural Engineers", Springer-Verlag, ISBN 0-387-96711-7.

Cook, R. D., Malkus, D. S and Plesha, M. E. (1989): "Concepts and Applications of Finite Element Analysis", 3rd ed., John Wiley & Sons Inc.

Corona, E. and Kyriakides, S (1988a): "On the collapse of inelastic tubes under combined bending and pressure", International Journal of Solids and Structures, vol. 24, pp.505-535.

Corona, E. and Kyriakides, S (1988b): "Collapse of pipelines under combined bending and external pressure", Proceeding Int. Conf. on the Behaviour of Offshore Structures, vol. 3, pp 953-964, Trondheim, Norway.

Crisfield, M. A. (1991): "Non-linear Finite Element Analysis of Solids and Structures", vol. I, J. Wiley and Sons, ISBN 0-471-92956-5.

Croll, J. G. A. and Ellinas, C. P. (1984): "Design formulation for Axisymmetric Collapse of Stiffened and Unstiffened Cylinders", Proceeding of the 3rd International Offshore Mechanics and Arctic Engineering Conference, vol. I, pp. 612-617.

DnV (1981): "Rules for submarine pipeline systems", Det norske Veritas, Høvik, Norway.

DnV (1988): "On-Bottom Stability Design of Submarine Pipelines", Recommended Practice RP E 305, Det norske Veritas, Høvik, Norway.

DnV (1996): "Rules for Submarine Pipeline Systems", Det norske Veritas, Høvik, Norway.

Donachie, M. J. jr. (1988): "Titanium – A Technical Guide", ASM International, ISBN 0-87170-309-2.

Dougherty, E. R. (1990): "Probability and Statistics for the Engineering, Computing and Physical Sciences", Prentice-Hall International Inc., ISBN 0-13-715913-7.

Emmerling, F. A. (1982): "Non-linear bending of elliptic tubes under normal pressure" Ingenieur-Arch., vol 52, pp. 1-16.

Fabian, O (1977): "Collapse of cylindrical, elastic tubes under combined bending, pressure and axial loads", International Journal of Solids and Structures, vol. 13, pp. 1257-1270.

Fabian, O (1981): "Elastic-plastic collapse of long tubes under combined bending and pressure loads", Ocean Engineering, vol. 8, pp.295-330.

Faravelli, L. (1989): "A Response Surface Approach for Reliability Analysis", Journal of Engineering Mechanics, ASCE, 115 (12), pp. 2763-2781.

Faravelli, L. and Bigi, D. (1990): "Stochastic Finite Elements for Crash Problems", Structural Safety, vol. 8, pp. 113-130.

Fowler, J. R. (1990): "Large scale tests", Proc, Seminar on Collapse of Offshore Pipelines, Houston, TX.

Gellin, S. (1980): "The plastic buckling of long cylindrical shells under pure bending", International Journal of Solids and Structures, vol. 10, pp.397-407.

Gorynin, I. V., Oushkov, S. S. and Koudriatsev, A. S. (1995): "The Features of Titanium Alloys Applications in Offshore Structures", Proc. Eighth World Conference on Titanium, Birmingham, UK, The Institute of Materials, London, pp. 1703-1710.

Henley, E: J. and Kumamoto, H. (1981): "Reliability Engineering and Risk Assessment", Prentice-Hall, Englewood Cliffs, New Jersey.

Holand, I. and Remseth, S. (1975): "Tube buckling, Interim report no. 1: Methodology", SINTEF Report STF71 F75030, Trondheim, Norway.

Hosford, W. F. and Caddell, R. M. (1993): "Metal forming – Mechanics and metallurgy", 2nd edition, Prentice-Hall, ISBN 0-13-588526-4.

Jiao, G., Sotberg, T. and Bruschi, R (1995): "SUPERB 2M Project: Wall Thickness Sizing:Lilit State Based Design Criteria for Offshore Pipelines", SINTEF Report STF70 F95226, Trondheim, Norway.

Jiao, G., Sotberg, T. and Igland, R. (1995): "Statistical Data: Uncertainty Measures for General Reliability Analysis for Offshore Pipelines", SINTEF Report STF70 F95212, Trondheim, Norway.

Jiao, G., et al. (1996): "Reliability Based Design Handbook: Offshore Pipelines", SINTEF Report STF22 F96742, Trondheim, Norway.

Jiao, G., Sotberg, T., Bruschi, R. and Igland, R. T. (1997): "The SUPERB Project: Linepipe Statistical Properties and Implications in Design of Offshore Pipelines", Proceeding of the Offshore Mechanics and Arctic Engineering Conference, vol. V, pp. 45-55.

Johns, T.G. and McConnel, D. P. (1983): "Response and stability of elastoplastic circular pipes under combined bending and external pressure", Proceeding of 11th Pipeline Technology Conference, Houston, TX.

Karamanos, S. A. and Tassoulas, J. L. (1991): "Stability of Deep-Water Pipelines under Combined Loading", Centre for Offshore Technology, The University of Texas at Austin, USA.

Karunakaran, D., Olufsen, A., Nordsve, N. T. and Leira, B. J. (1995): "Reliability Analysis of Deep Water Flexible Riser System", Proceeding from the Fifth International Offshore and Polar Engineering Conference (ISOPE), pp. 365-372.

Karunakaran, D., Nordsve, N. T. and Olufsen, A. (1996): "An Efficient Metal Riser Configuration for Ship and Semi Based Production Systems", Proceeding from the Sixth International Offshore and Polar Engineering Conference (ISOPE).

Khan, A. S. and Huang, S. (1995): "Continuum Theory of Plasticity", John Wiley and Sons, ISBN 0-471-31043-3.

Khuri, A. I. and Cornell, J. A. (1987): "Response Surface. Design and Analyses", Marcel Dekker, Inc, ASQC, Quality Press, ISBN 0-8247-7653-4.

Korol, R. M. (1979): "Critical Buckling Strains of Round Tubes in Flexure", International Journal Mech. Sci., vol. 21, pp. 719-730.

Kyriakides, S. and Shaw, P.K. (1982):"Response and stability of elastoplastic circular pipes under combined bending and external pressure", International Journal of Solids and Structures, vol. 18, pp 957-973.

Kyriakides, S. and Ju, G. T. (1992): "Bifurcation and localisation instabilities in cylindrical shells under bending-I. Experiments", International Journal of Solids and Structures, vol. 29, pp. 1117-1142.

Larsen, C. M. (1995): "Marine Riser Analysis", lecture note in Dr. Ing.-course "Slender Marine Structures", Division of Marine Structures, Faculty of Marine Technology, NTNU, Trondheim, Norway..

Larsen, C. M. (1996): "On Displacement Controlled and Load Controlled Buckling of Pipes", memo, Division of Marine Structures, Faculty of Marine Technology, NTNU, Trondheim, Norway.

Larssen, R. M., Remseth, S. and Leira, B. J. (1994): "Parameter Sensitivity of Predicted Extreme Response for a Submerged Tubular Bridge", Strait Crossings '94, Balkema, Rotterdam, The Netherlands.

Lemaitre, J. and Chaboche, J.-L. (1990): "Mechanics of Solid Materials", Cambridge University Press, ISBN 0-521-32853-5.

Lunde, L., Peacock, D. K., Murali, J. and Aarnes, R. (1995): "Titanium Components in Offshore Gas/Oil Environments", Proc. Eighth World Conference on Titanium, Birmingham, UK, The Institute of Materials, London, pp. 1715-1718.

Madsen, H. O., Krenk, S. and Lind, N. C. (1986): "Methods of Structural Safety", Prentice-Hall Inc., ISBN 0-13-579475-7.

Makowski, J. and Stumpf, H. (1990): "Buckling equations for elastic shells with rotational degrees of freedom undergoing finite strain deformation", International Journal of Solid and Structures, vol. 26, pp. 353-368.

Malvern, L. E. (1969): "Introduction to the Mechanics of a Continuous Medium", Prentice-Hall.

Melchers, R. E. (1987): "Structural Reliability. Analysis and prediction", John Wiley & Sons, ISBN 0-85312-930-4.

Mohareb, M., Alexander, S. D., Kulak, G. L. and Murray, D. W. (1993): "Laboratory testing of line pipe to determine deformational behaviour", Proceeding of the Offshore and Arctic Engineering Conference, vol. V, pp. 109-114.

Mollan, R. (1992): "Materials for the Snorre Flexible Flowlines and Risers", Proceeding of the International Seminar on Recent Research and Development within Flexible Pipe Technology (FPT), Trondheim, Norway.

Murphey, C. E. and Langner C. G (1985): "Ultimate pipe strength under bending, collapse and fatigue", Proceeding of the 4th International Conference of Offshore and Arctic Engineering, Vol. I, pp. 467-477.

Myers, R. H. and Montgomery, D. C. (1995): "Response Surface Methodology. Process and Product Optimization Using Designed Experiments", John Wiley and Sons, ISBN 0-471-58100-3.

Mørk, K., Spiten, J. and Collberg, L. (1996): "SUPERB Project: Buckling and Collapse Limit State", Report STF22 F96741, SINTEF - Snamprogetti - DnV.

NAFEMS (1992): "Introduction to Nonlinear Finite Element Analysis", edited by E. Hinton, Bell and Bain Ltd., ISBN 1-874376-00.

Olivi, L. (1984): "Response Surface Methodology. Handbook for Nuclear Reactor Safety", EUR 9600EN, JRC Ispra.

PROBAN (1996): Sesam User's Manual, Det norske Veritas, Høvik, Norway.

Rackwitz, R. and Fiessler, B. (1978): "Structural Reliability under Combined Random Load Sequences" Computers and Structures, vol. 9, pp. 489-494.

Rajashekhar, M. R. and Ellingwood, B. R. (1993): "A New Look at the Response Surface Approach for Reliability Analysis", Structural Safety, vol. 12, pp. 205-220.

Ramberg, W. and Osgood, W. R. (1943): "Description of Stress-Strain Curves by three Parameters", NACA Technical Note 902.

Reddy, B. D. (1979): "An Experimental Study of the Plastic Buckling of Circular Cylinders in Pure Bending", International Journal of Solids and Structures, vol. 15, pp. 669-683.

Reissner, E. (1959): "On finite bending of pressurized tubes", ASME J. of Applied Mechanics, vol. 26, pp. 386-392.

Reissner, E. and Weinitschke, H. J. (1963): "Finite pure bending of circular cylindrical tubes", Quarterly of Applied Mathematics, vol 10, pp.305-319.

Remseth, S., Holthe, K., Bergan, P. G. and Holand, I. (1977): "Tube buckling analysis by the finite element method", Proceeding of International Conference on Finite Elements in Non-linear Solid and Structural Mechanics, Geilo, Norway.

RIFLEX (1995): "Flexible Riser System Analysis Program", SINTEF, MARINTEK and NTNU, Trondheim, Norway.

Riks, E. (1979): "An incremental approach to the solution of snapping and buckling problems", Int. J. of Solids and Structures, vol. 15, pp. 529-551.

Row, D., Chan, E. and Langner, C. G. (1987): "Prediction of pipe collapse under external pressure, axial load and bending", Offshore and Arctic pipelines edited by J. S. Chung and K. Karal.

Rubinstein, R. Y. (1981): "Simulation of the Monte Carlo Method", John Wiley & Sons Inc., New York.

Salama, M. M., Murali, J. and Joosten, M. W. (1998): "Titanium Drilling Risers-Application and Qualification", Proceeding of the Offshore and Arctic Engineering Conference.

Sauer, C. W., Sexton, J. B., Sokoll, R. E. and Thornton, J. M. (1996): "Heidrun TLP Titanium Drilling Riser System", Proceeding of the Offshore Technology Conference, vol. II, pp. 559-582.

Schilling, G. S. (1976): "Buckling Strength of Circular Tubes", Journal Struct Div, ASCE, vol. 91, pp. 325-348.

Schneider, J. (1981): "Organization and Management of Structural Safety during Design, Construction and Operation of Structures", Structural and Safety, Elsevier, Amsterdam, The Netherlands, pp. 467-482.

Schutz, R. W. (1999): Fax dated 990104 from RMI Titanium Company, Technical Center, Ohio, USA.

Sertã, O. B., Mourelle, M. M., Grealish, F. W., Harbert, S. J., Souza, L. F. A. (1996): "Steel Catenary Riser for the Marlim Field FPS P-XVIII", Proceeding of the Offshore Technology Conference, OTC 8069, pp. 359-366.

Shaw, P. K. and Kyriakides, S. (1985): "Inelastic analysis of thin-walled tubes under cyclic bending", International Journal of Solids and Structures, vol. 21.

Sherman, D. R. (1976): "Tests of Circular Steel Tubes in Bending", Journal Struc Div, ASCE, vol. 102, pp. 2181-2195.

Sparks, C. P. (1980): "The Influence of Tension, Pressure and Weight on Pipe and Riser Deformations and Stresses", Journal of Energy Resources Technology, ASME.

Spolton, S. (1999): Fax dated 990520 from RTI Energy Systems, Inc., Surrey, UK.

SUPERB (1996): "Limit State Design Guideline for Offshore Pipelines", Report STF22 F96745, SUPERB Project, SINTEF-Snamprogetti-DnV.

Tetyunkhin, V. V. and Smirnov, V. G. (1996): "A New Wrought Titanium Alloy for Offshore Production Tubes", Report 1996, VSMPO (Verkhnyaya Salda Metallurgical Production Association) 1, Parkovaya St. Verkhnyaya, Salda Sverdlovsk Region 624600, Russia.

Tetyunkhin, V. V., Smirnov, V. G., Karpenko, N. P. and Safyanov, A. V. (1996): "Manufacture of Titanium-Alloy Tubes for Geological Prospecting and On-Land and Offshore Oil and Gas Production", Report 1996, VSMPO (Verkhnyaya Salda Metallurgical Production Association) 1, Parkovaya St. Verkhnyaya, Salda Sverdlovsk Region 624600, Russia.

Thornton, J. M. (1994): "The Heidrun TLP titanium drilling riser", 8th Offshore Technology Conference, pp.268-289.

Timoshenko, S. P and Gere, J. M. (1961): "Theory of elastic stability", 2nd ed, McGraw-Hill.

Timoshencko, S. P. and Goodier, C. G. (1970): "Theory of Elasticity", McGraw Hill, 3rd ed.

Thoft-Christensen, P. and Baker, M. J. (1982): "Structural Reliability Theory and Its Applications", Springer Verlag Berlin, Heidelberg, Germany.

Torselletti, E. and Curti, G. (1995): "Capacity Models for Collapse and Buckling", Report STF70 F95229, SUPERB Project, SINTEF – Snamprogetti – DnV.

Tryland, T., Hopperstad, O. S. and Remseth, S. (1997): "Material Properties of a Titanium Pipe", Dep. of Structural Engineering, NTNU, Trondheim, Norway.

Tvergaard, V. (1976): "Buckling of Elasto-Plastic Oval Cylindrical Shells under Axial Compression", International Journal of Solids and Structures, Vol. 12, pp. 683-691.

Tvergaard, V. and Needleman, A. (1980): "On the Localization of Buckling Patterns", Journal of Applied Mechanics, vol. 47, pp. 613-619.

van den Berg, G. (1995): "A finite strain shell model for the analysis of moderately thick-walled tubes", Ph.D.-thesis, Delft University Press, ISBN 90-407-1129-1, The Netherlands.

Voce, E. (1948): Journal of Inst. Methods, vol. 47, pp. 537.

Walker, A. C. (1994): "Bending of Pipelines to High Levels of Strain", Proceeding of the SUT Conference, ASPECT '94, Aberdeen, Scotland, pp. 32-36.

Willson, A. J. and Myers, P. J. (1990): "On the finite elasto-static deformation of thin-walled spheres and cylinders", International Journal of Solids and Structures, vol. 26, pp. 369-373.

Winter, P. E. de, Stark, J. W. B and Witteveen, J. (1985): "Collapse behaviour of submarine pipelines", Shell Structures: Stability and Strength, ed. R. Narayanan, Elsvier Appl. Sc. Publ., chapter 7, pp. 221-226.

Yeh, M. K. and Kyriakides, S. (1986a): "On the Collapse of inelastic thick-walled tubes under external pressure", ASME Journal of Energy Resources Technology, vol. 108.

Yeh, M. K. and Kyriakides, S. (1986b): "Collapse of deep water pipelines", OTC 5215, Proceeding of the Offshore Technology Conference, vol. 3.

Zhou, Z. and Murray, D. W. (1993a): "Behaviour of buried pipelines subjected to imposed deformations", Proceeding of the Offshore and Arctic Engineering Conference, vol. V, pp. 115-122.

Zhou, Z. and Murray, D. W. (1993b): "Towards rational deformation limit states for buried pipelines", Proceeding of ISOPE, vol. II, pp. 18-24.

Zhou, Z. and Murray, D. W. (1995): "Formulation and verification for pipeline beam models using stiffness-property-deformation relations", Journal of Transportation Engineering, ASCE.

APPENDICES

APPENDIX A: Plots of distributions of the maximum bending moment capacity.

APPENDIX B: List of former dr.ing.-thesis at the Division of Structural Engineering, Faculty of Civil and Environmental Engineering, the Norwegian University of Science and Technology, Norway.

A P P E N D I X A :

PLOT OF DISTRIBUTION FITTINGS FOR THE MAXIMUM BENDING MOMENT CAPACITY.

This appendix contains fittings of the distribution for the maximum bending moment capacity for the three sets of C.o.V., as given in Table 5.12. These figures are the basis of the R^2-values given in Table 5.13, and are similar to Figure 5.16. However, this appendix includes figures for all three C.o.V. sets and all considered distributions. A good fit is represented by a high value of R^2 (i.e. close to 1.0), and that the data represented by the squares (called Data) match the continuous lines representing either lognormal, Gumbel, Gaussian or Weibull distribution.

LOW VALUES OF C.o.V:

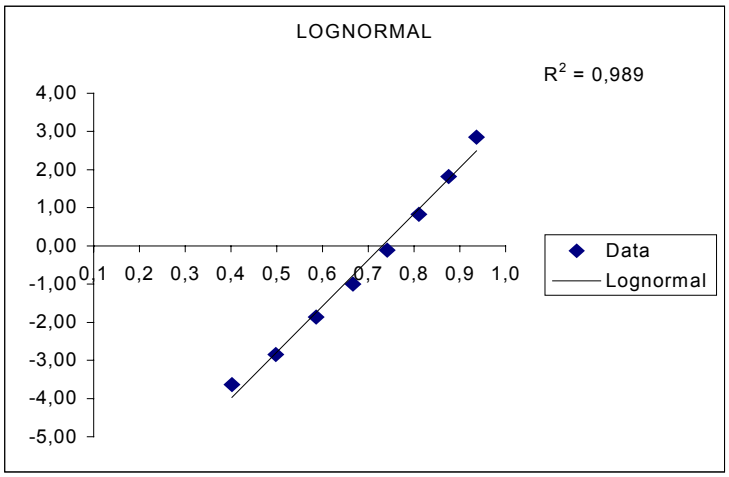

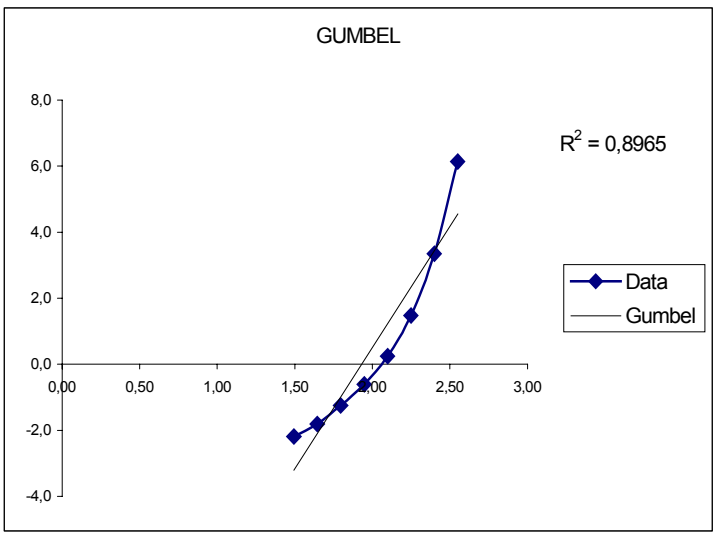

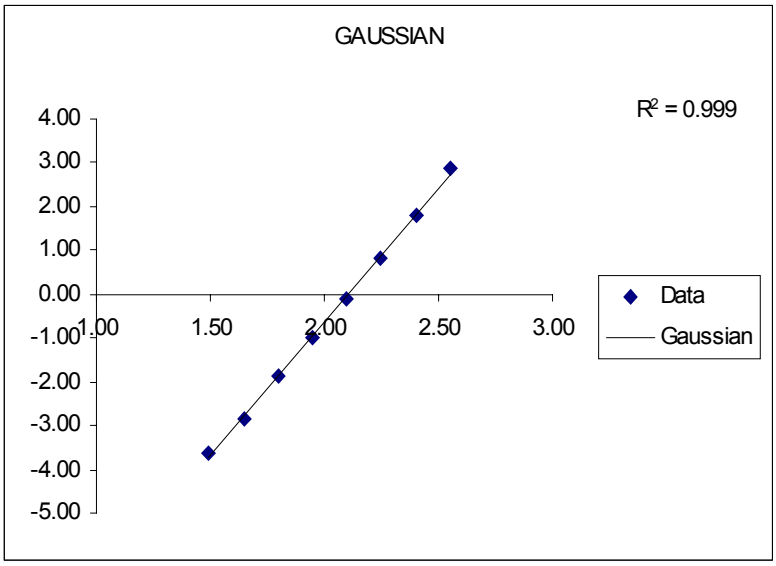
GAUSSIAN
R² = 0.999
4.00
3.00
2.00
1.00
0.00
-1.00
-2.00
-3.00
-4.00
-5.00
1.00
1.50
2.00
2.50
3.00
Data
Gaussian

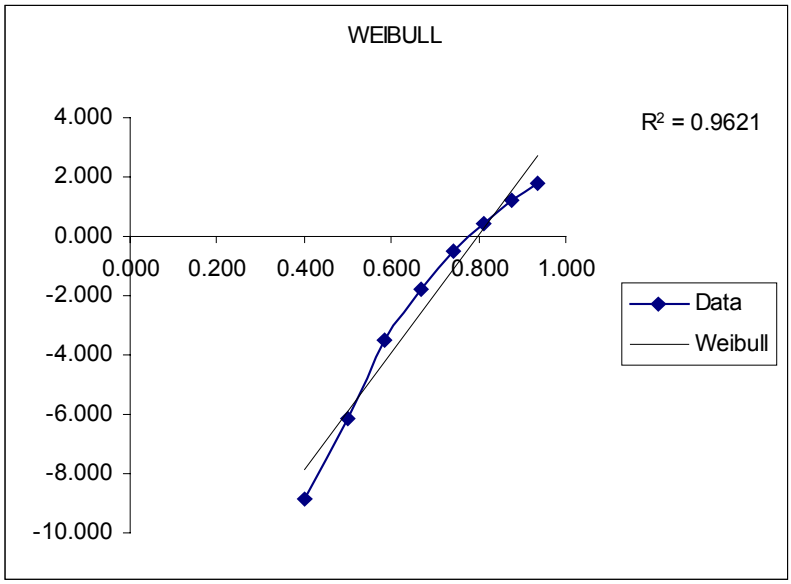
WEIBULL
R² = 0.9621
4.000
2.000
0.000
-2.000
-4.000
-6.000
-8.000
-10.000
0.000
0.200
0.400
0.600
0.800
1.000
Data
Weibull

MEAN VALUES OF C.o.V:

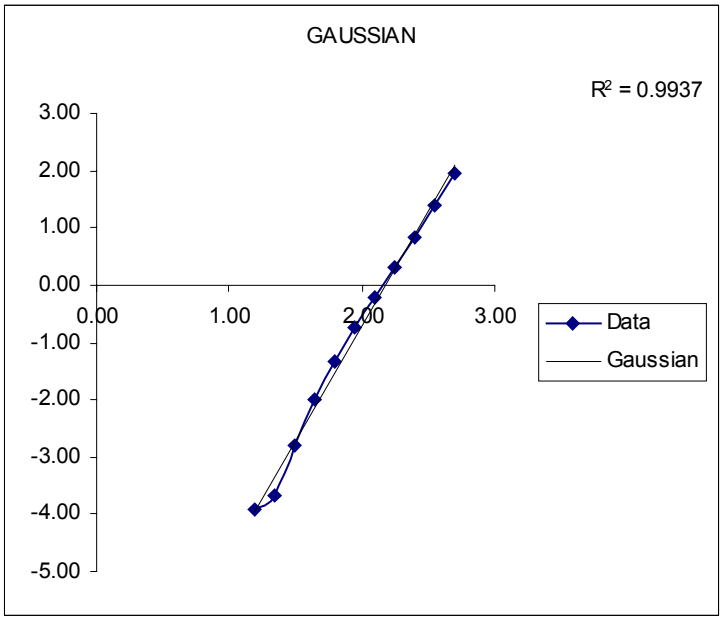

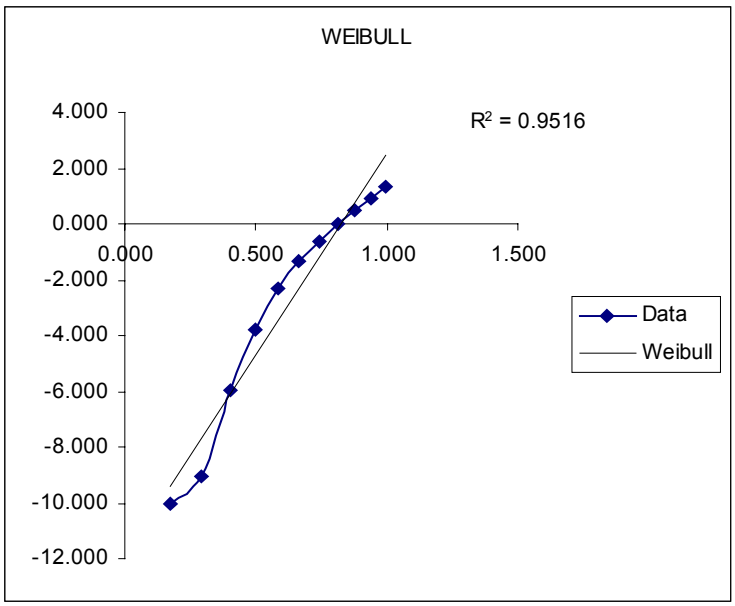

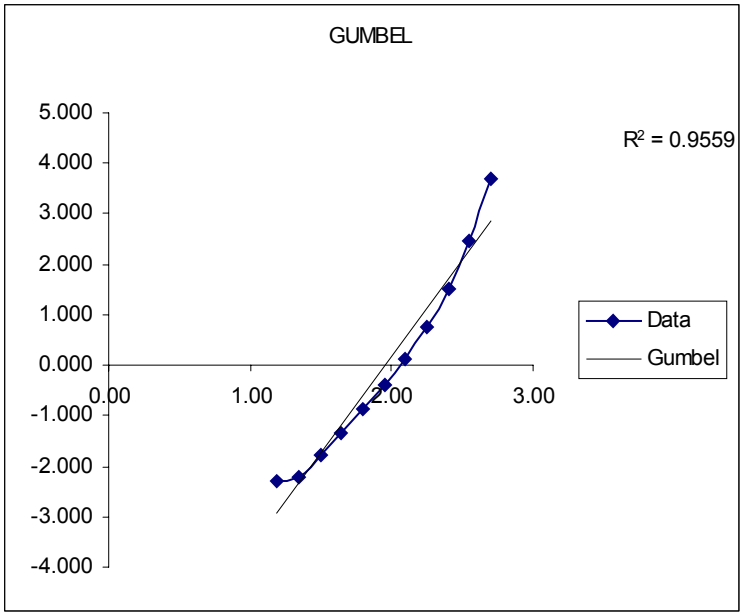
GUMBEL
R² = 0.9559
5.000
4.000
3.000
2.000
1.000
0.000
-1.000
-2.000
-3.000
-4.000
0.00
1.00
2.00
3.00
Data
Gumbel

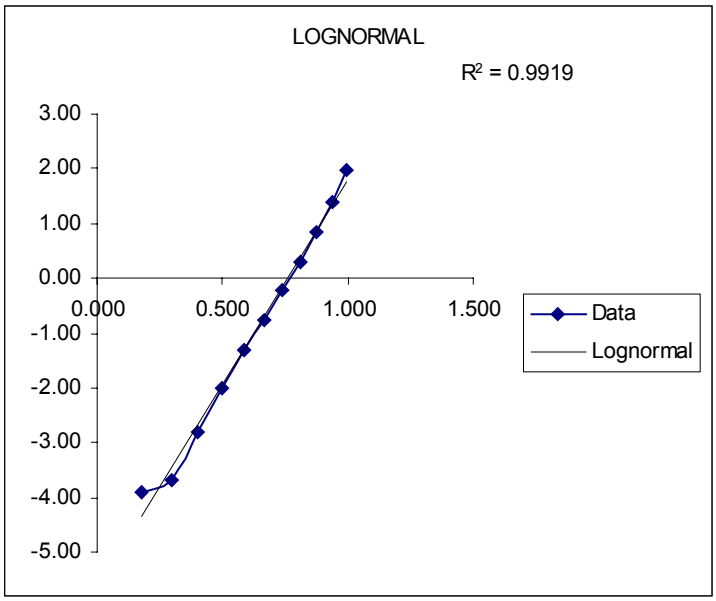
LOGNORMAL
R² = 0.9919
3.00
2.00
1.00
0.00
-1.00
-2.00
-3.00
-4.00
-5.00
0.000
0.500
1.000
1.500
Data
Lognormal

HIGH VALUES OF C.o.V:

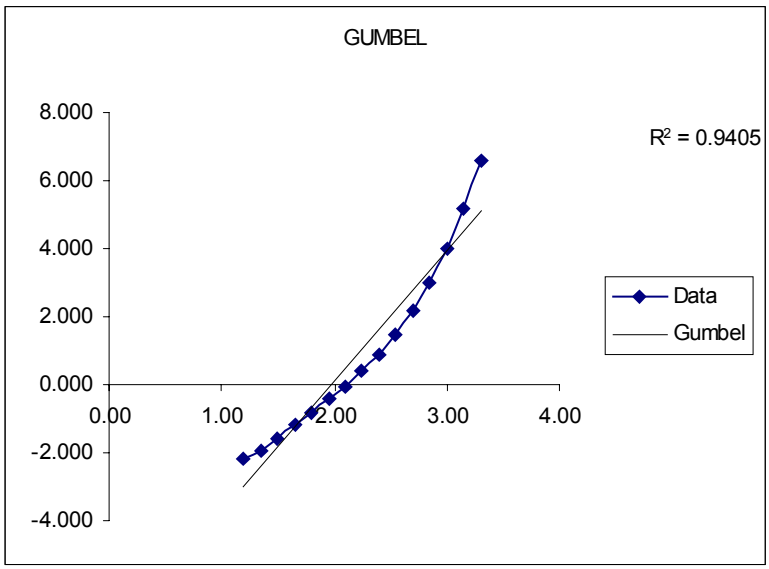

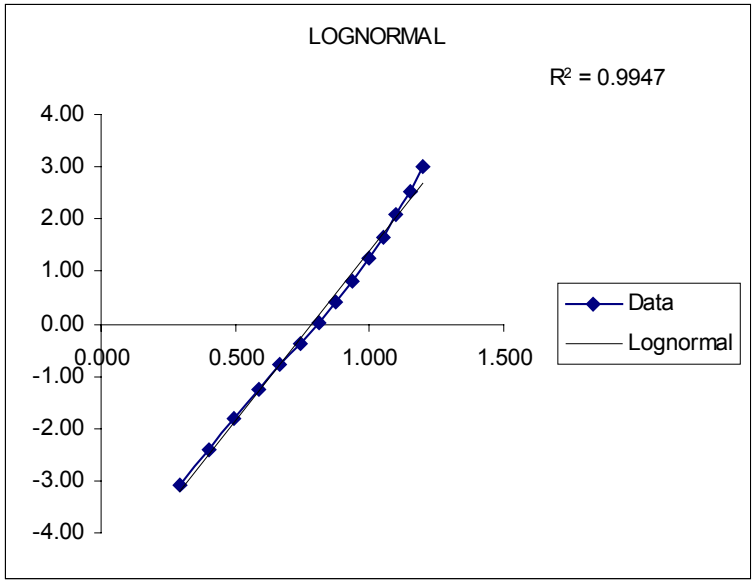

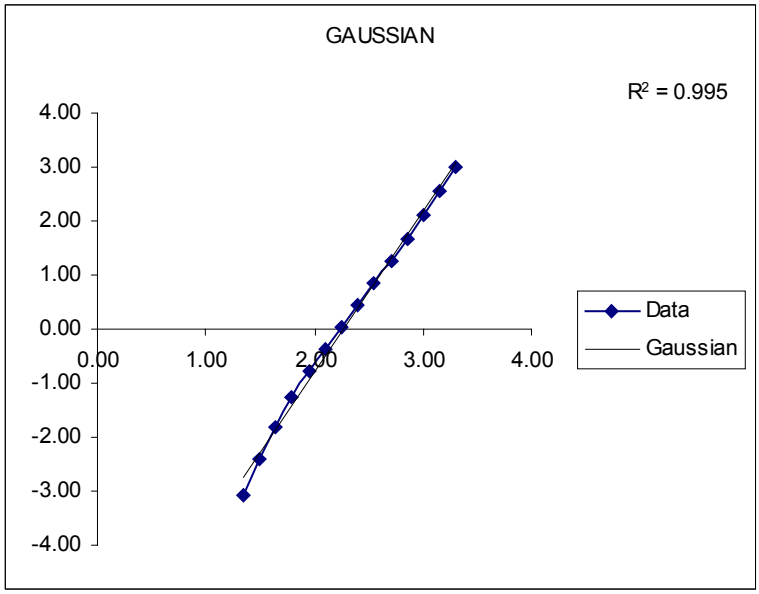
GAUSSIAN
R² = 0.995
4.00
3.00
2.00
1.00
0.00
-1.00
-2.00
-3.00
-4.00
0.00
1.00
2.00
3.00
4.00
Data
Gaussian

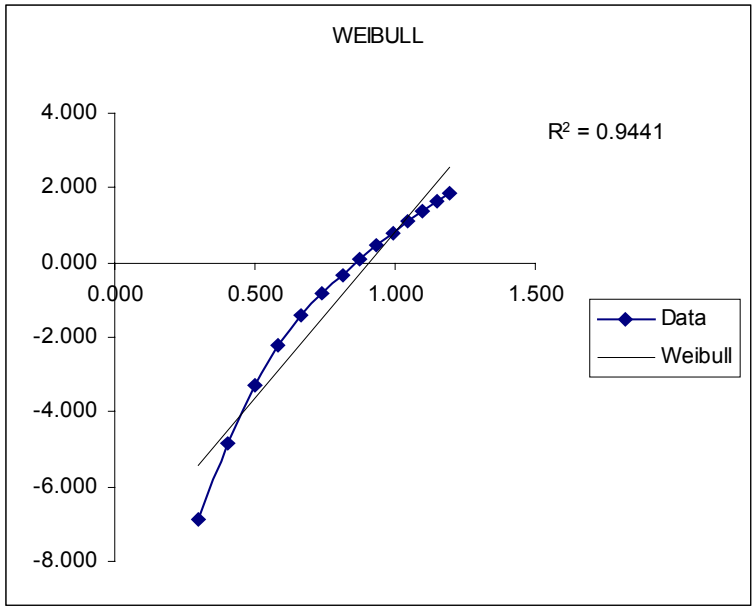
WEIBULL
R² = 0.9441
4.000
2.000
0.000
-2.000
-4.000
-6.000
-8.000
0.000
0.500
1.000
1.500
Data
Weibull

A P P E N D I X B :

LIST OF FORMER DR.ING.-THESIS.

DEPARTMENT OF STRUCTURAL ENGINEERING
NORWEGIAN UNIVERSITY OF SCIENCE AND TECHNOLOGY

N–7491 TRONDHEIM, NORWAY
Telephone: +47 73 59 47 00 Telefax: +47 73 59 47 01

"Techniques for Static and Dynamic Solution for Nonlinear Finite Element Problems",
E. Mollestad - 1983, ISBN 82-90240-14-7.

"Flow-related Aspects of Hasard Area Prediction Following an Accidental Gas Release",
K. J. Eidsvik - 1983.

"Resonant Behaviour of Taut Cables Subjected to Deterministic and Stochastic Excitations",
T. Kjoberg - 1983.

"Sand Waves in Free Surface Flow. A Study with Emphasis on Hydrodynamic Aspects",
H. Moshagen - 1984.

"Free Span Vibrations of Submarine Pipelines in Steady and Wave Flows",
A. N. Mysore - 1985.

"An Experimental Study on Steel Column Behaviour at Elevated Temperatures",
B. Aasen - 1985.

"Nonlinear Analysis of Reinforced Concrete Structures Using Beam and Membrane Elements",
O. Strøm - 1986, ISBN 82-90240-15-5.

"The Free Formulation for Nonlinear Finite Elements with Applications to Shells",
M. K. Nygård - 1986, ISBN 82-90240-16-3.

"Hydrodynamic Force Coefficients in Random Wave Conditions",
T. Bostrøm - 1987.

"A Model for Oscillatory Turbulent Boundary Layers with Suspended Sediment",
K. Hagatun - 1987.

"Implementation of Turbular Joint Flexibility in Global Frame Analysis",
T. Holmås - 1987, ISBN 82-90240-17-1.

"Elasto-Plastic Material Models in the Nonlinear Finite Element Method",
K. E. Moen - 1987, ISBN 82-90240-19-8.

"Current Induced Vibrations and Scour of Pipeline on a Sandy Bottom",
Ø. Kristiansen, 1988:7, ISBN 82-7119-022-9.

"On the Dynamic Analysis of Large Floating Structures",
T. Lokna, 1988:21, ISBN 82-7119-038-5.

"Cyclic Plasticity Modelling in Force Space",
O. C. Astrup, 1988:23, ISBN 82-7119-040-7.

"Dropped Objects. Plugging Capacity of Steel Plates",
M. Langseth, 1988:25, ISBN 82-7119-042-3.

"Cyclic Plasticity and low Cycle Fatigue of Structural Steel and Buttwelded Components",
B. Skallerud, 1988:26, ISBN 82-7119-043-1.

"Nonlinear Static and Dynamic Analysis of Slender Structures Subjected to Hydrodynamic Loading",
H. T. Hansen, 1988:40, ISBN 82-7119-059-8.

"Pseudo-Dynamic Testing. Experimental Accuracy and Techniques",
K. A. Malo, 1988:56, ISBN 82-7119-077-6.

"The Pseudodynamic Test Method. Numerical Algorithms and Implementation",
E. Eberg, 1989:1, ISBN 82-7119-081-4.

"Wave and Current Forces on Pipelines at the Sea-bed",
O. A. Grytå, 1989:5, ISBN 82-7119-085-7.

"Passive Fire Protection subjected to Gas Explosion and Fire Loads",
T. A. Håverstad, 1989:24, ISBN 82-7119-106-3.

"Current Induced Vibrations of a Flexible Cylinder",
Zhi-Jie Wu, 1989:34, ISBN 82-7119-085-7.

"Dynamic Behaviour of Riser Systems Exposed to Internal Fluid Flow - An Analytical Approach",
K. C. Strømsem, 1989:55, ISBN 82-7119-141-1.

"Reliability Analysis of Structural Systems using Nonlinear Finite Element Methods",
C. A. Holm, 1990:23, ISBN 82-7119-178-0.

"Uniform Stratified Flow Interaction with a Submerged Horizontal Cylinder",
Ø. Arntsen, 1990:32, ISBN 82-7119-188-8.

"Large Displacement Analysis of Flexible and Rigid Systems Considering Displacement-Dependent Loads and Nonlinear Constraints",
K. M. Mathisen, 1990:33, ISBN 82-7119-189-6.

"Solid Mechanics and Material Models including Large Deformations",
E. Levold, 1990:56, ISBN 82-7119-214-0, ISSN 0802-3271.

"Inelastic Deformation Capacity of Flexurally-Loaded Aluminium Alloy Structures",
T. Welo, 1990:62, ISBN 82-7119-220-5, ISSN 0802-3271.

"Visualization of Results from Mechanical Engineering Analysis",
K. Aamnes, 1990:63, ISBN 82-7119-221-3, ISSN 0802-3271.

"Object-Oriented Product Modeling for Structural Design",
S. I. Dale, 1991:6, ISBN 82-7119-258-2, ISSN 0802-3271.

"Parallel Techniques for Solving Finite Element Problems on Transputer Networks",
T. H. Hansen, 1991:19, ISBN 82-7119-273-6, ISSN 0802-3271.

"Statistical Description and Estimation of Ocean Drift Ice Environments",
R. Korsnes, 1991:24, ISBN 82-7119-278-7, ISSN 0802-3271.

"Turbidity Current Modelling",
B. Brørs, 1991:38, ISBN 82-7119-293-0, ISSN 0802-3271.

"Zero-Slump Concrete: Rheology, Degree of Compaction and Strength. Effects of Fillers as Part Cement-Replacement",
C. Sørensen, 1992:8, ISBN 82-7119-357-0, ISSN 0802-3271.

"Nonlinear Analysis of Reinforced Concrete Structures Exposed to Transient Loading",
K. V. Høiseth, 1992:15, ISBN 82-7119-364-3, ISSN 0802-3271.

"Finite Element Formulations and Solution Algorithms for Buckling and Collapse Analysis of Thin Shells",
R. O. Bjærum, 1992:30, ISBN 82-7119-380-5, ISSN 0802-3271.

"Response Statistics of Nonlinear Dynamic Systems",
J. M. Johnsen, 1992:42, ISBN 82-7119-393-7, ISSN 0802-3271.

"Digital Models in Engineering. A Study on why and how engineers build and operate digital models for decisison support",
J. Høyte, 1992:75, ISBN 82-7119-429-1, ISSN 0802-3271.

"Sparse Solution of Finite Element Equations",
A. C. Damhaug, 1992:76, ISBN 82-7119-430-5, ISSN 0802-3271.

"Some Aspects of Floating Ice Related to Sea Surface Operations in the Barents Sea",
S. Løset, 1992:95, ISBN 82-7119-452-6, ISSN 0802-3271.

"Modelling of Cyclic Plasticity with Application to Steel and Aluminium Structures",
O. S. Hopperstad, 1993:7, ISBN 82-7119-461-5, ISSN 0802-3271.

"The Free Formulation: Linear Theory and Extensions with Applications to Tetrahedral Elements with Rotational Freedoms",
G. Skeie, 1993:17, ISBN 82-7119-472-0, ISSN 0802-3271.

"Høyfast betongs motstand mot piggdekkslitasje. Analyse av resultater fra prøving i Veisliter'n",
T. Tveter, 1993:62, ISBN 82-7119-522-0, ISSN 0802-3271.

"A Nonlinear Finite Element Based on Free Formulation Theory for Analysis of Sandwich Structures",
O. Aamlid, 1993:72, ISBN 82-7119-534-4, ISSN 0802-3271.

"The Effect of Curing Temperature and Silica Fume on Chloride Migration and Pore Structure of High Strength Concrete",
C. J. Hauck, 1993:90, ISBN 82-7119-553-0, ISSN 0802-3271.

"Failure of Concrete under Compressive Strain Gradients",
G. Markeset, 1993:110, ISBN 82-7119-575-1, ISSN 0802-3271.

"An experimental study of internal tidal amphidromes in Vestfjorden",
J. H. Nilsen, 1994:39, ISBN 82-7119-640-5, ISSN 0802-3271.

"Structural analysis of oil wells with emphasis on conductor design",
H. Larsen, 1994:46, ISBN 82-7119-648-0, ISSN 0802-3271.

"Adaptive methods for non-linear finite element analysis of shell structures",
K. M. Okstad, 1994:66, ISBN 82-7119-670-7, ISSN 0802-3271.

"On constitutive modelling in nonlinear analysis of concrete structures",
O. Fyrileiv, 1994:115, ISBN 82-7119-725-8, ISSN 0802-3271.

"Fluctuating wind load and response of a line-like engineering structure with emphasis on motion-induced wind forces",
J. Bogunovic Jakobsen, 1995:62, ISBN 82-7119-809-2, ISSN 0802-3271.

"An experimental study of beam-columns subjected to combined torsion, bending and axial actions",
A. Aalberg, 1995:66, ISBN 82-7119-813-0, ISSN 0802-3271.

"Scaling and cracking in unsealed freeze/thaw testing of Portland cement and silica fume concretes",
S. Jacobsen, 1995:101, ISBN 82-7119-851-3, ISSN 0802-3271.

"Damping of water waves by submerged vegetation. A case study of laminaria hyperborea",
A. M. Dubi, 1995:108, ISBN 82-7119-859-9, ISSN 0802-3271.

"The dynamics of a slope current in the Barents Sea",
Sheng Li, 1995:109, ISBN 82-7119-860-2, ISSN 0802-3271.

"Modellering av delmaterialenes betydning for betongens konsistens",
Ernst Mørtsell, 1996:12, ISBN 82-7119-894-7, ISSN 0802-3271.

"Bending of thin-walled aluminium extrusions",
Birgit Søvik Opheim, 1996:60, ISBN 82-7119-947-1, ISSN 0802-3271.

"Material modelling of aluminium for crashworthiness analysis",
Torodd Berstad, 1996:89, ISBN 82-7119-980-3, ISSN 0802-3271.

"Estimation of structural parameters from response measurements on submerged floating tunnels",
Rolf Magne Larssen, 1996:119, ISBN 82-471-0014-2, ISSN 0802-3271.

“Numerical modelling of plain and reinforced concrete by damage mechanics”,
Mario A. Polanco-Loria, 1997:20, ISBN 82-471-0049-5, ISSN 0802-3271.

“Nonlinear random vibrations - numerical analysis by path integration methods”,
Vibeke Moe, 1997:26, ISBN 82-471-0056-8, ISSN 0802-3271.

“Numerical prediction of vortex-induced vibration by the finite element method”,
Joar Martin Dalheim, 1997:63, ISBN 82-471-0096-7, ISSN 0802-3271.

“Time domain calculations of buffeting response for wind sensitive structures”,
Ketil Aas-Jakobsen, 1997:148, ISBN 82-471-0189-0, ISSN 0802-3271

“Estimation of chloride penetration into concrete bridges in coastal areas”,
Per Egil Steen, 1998:89, ISBN 82-471-0290-0, ISSN 0802-3271.

“Stress-resultant material models for reinforced concrete plates and shells”,
Jan Arve Øverli, 1998:95, ISBN 82-471-0297-8, ISSN 0802-3271.

“Chloride binding in concrete. Effect of surrounding environment and concrete composition”,
Claus Kenneth Larsen, 1998:101, ISBN 82-471-0337-0, ISSN 0802-3271.

“Rotational capacity of aluminium alloy beams”,
Lars A. Moen, 1999:1, ISBN 82-471-0365-6, ISSN 0802-3271.

“Stretch Bending of Aluminium Extrusions”,
Arild H. Clausen, 1999:29, ISBN 82-471-0396-6, ISSN 0802-3271.

“Aluminium and Steel Beams under Concentrated Loading”,
Tore Tryland, 1999:30, ISBN 82-471-0397-4, ISSN 0802-3271.

"Engineering Models of Elastoplasticity and Fracture for Aluminium Alloys",
Odd-Geir Lademo, 1999:39, ISBN 82-471-0406-7, ISSN 0802-3271.

"Kapasitet og duktilitet av dybelforbindelser i trekonstruksjoner",
Jan Siem, 1999-46, ISBN 82-471-0414-8, ISSN 0802-3271.

“Etablering av distribuert ingeniørarbeid; Teknologiske og organisatoriske erfaringer fra en norsk ingeniørbedrift”,
Lars Line, 1999:52, ISBN 82-471-0420-2, ISSN 0802-3271.

“Estimation of Earthquake-Induced Response”,
Símon Ólafsson, 1999:73, ISBN 82-471-0443-1, ISSN 0802-3271.

“Coastal Concrete Bridges: Moisture State, Chloride Permeability and Aging Effects”,
Ragnhild Holen Relling, 1999:74, ISBN 82-471-0445-8, ISSN 0802-3271.

“Validation of Numerical Collapse Behaviour of Thin-Walled Corrugated Panels”,
Håvar Ilstad, 1999:101, ISBN 82-471-0474-1, ISSN 0802-3271.

“Strength and Ductility of Welded Structures in Aluminium Alloys”,
Miroslaw Matusiak, 1999:113, ISBN 82-471-0487-3, ISSN 0802-3271.

“Thermal Dilation and Autogenous Deformation as Driving Forces to Self-Induced Stresses in High Performance Concrete”,
Øyvind Bjøntegaard, 1999:121, ISBN 82-7984-002-8, ISSN 0802-3271.

“Some Aspects of Ski Base Sliding Friction and Ski Base Structure”,
Dag Anders Moldestad, 1999:137, ISBN 82-7984-019-2, ISSN 0802-3271.

"Electrode reactions and corrosion resistance for steel in mortar and concrete",
Roy Antonsen, 2000:10, ISBN 82-7984-030-3, ISSN 0802-3271.

"Hydro-Physical Conditions in Kelp Forests and the Effect on Wave Damping and Dune Erosion. A case study on Laminaria Hyperborea",
Stig Magnar Løvås, 2000:28, ISBN 82-7984-050-8, ISSN 0802-3271.

”Capacity Assessment of Titanium Pipes Subjected to Bending and External Pressure”,
Arve Bjørset, 1999:100, ISBN 82-471-0473-3, ISSN 0802-3271.